People’s Democratic Republic of Algeria

Ministry of Higher Education and Scientific Research

University of Mohamed Boudiaf – M’Sila

FACULTY OF TECHNOLOGY

DEPARTEMENT OF MECHANICAL ENGINEERING

Serial number: ……………………

Inscribtion number: ………………

Ph.D Thesis

Presented to fulfill the requirements to obtain

ACADEMIC Ph.D DEGREE

Subject-Field: Sciences and Technology

Option: Mechanical engineering

Specialty: Energetics

Subject

Study of heat transfer in a photovoltaic (PV) module

Presented by:

Abdelhak Keddouda

Defended on: 24/02/2025

Thesis examination committee:

Pr. Samir Zeghlache	Professor	University of M’Sila	President
Pr. Razika Ihaddadene	Professor	University of M’Sila	Supervisor
Dr. Badis Bakri	Associate professor	University of M’Sila	Examiner
Dr. Zakaria Haddad	Associate professor	University of M’Sila	Examiner
Dr. Abdelouahab Benseddik	Associate professor	University of Ghardaïa	Examiner

Academic Year: 2024/2025

Dedications

This work is dedicated:

To my mother for her love, confidence, and motivation, may this work be a testimony of my deep gratitude.

To my brothers and sisters.

To my professors.

To all my family.

To all friends.

To anyone who ever gave me love, hope and support.

Abdelhak

Acknowledgments

First and foremost, we extend our deepest gratitude to the Almighty Allah for granting us the will and strength to complete this thesis. We would also like to express our profound appreciation to the esteemed supervisor, Pr. Razika Ihaddadene, Professor in the Department of Mechanical Engineering at the University of M’Sila, for her valuable guidance, support, and care provided throughout the research process. Her mentorship will always serve as a source of inspiration.

Our sincere thanks and appreciation also go to Dr. Ali Boukhari, and Pr. Abdelmalek Atia, Professors in the Department of Mechanical Engineering at the University of El Oued, for their generous support and guidance during the course of this research. Also, special thanks and gratitude to Pr. Müslüm Arici from Kocaeli University, Turkey, for his precious help and valuable advices.

We extend our heartfelt thanks to everyone who contributed to the completion of this research, especially Dr. Nacer Lebbihiat, and all the professors in the Department of Mechanical Engineering at both the University of M’Sila and the University of El Oued.

Last but not least, we express our deepest gratitude to our friends, families, and beloved ones for their continuous support, patience, and confidence, which have been helpful in bringing this work to fruition.

Table of Contents

List of Tables

List of Figures

Nomenclature

A:	Module area	m^2
B:	Model coefficients	-
b:	Bias term	-
C_p:	Specific heat capacity	$J.kg^{-1}.K^{-1}$
ΔT:	Temperature difference ($T_{pv} - T_a$)	°C
F:	View factor	-
G:	Global solar radiation/Solar radiation	$W.m^{-2}$
g:	Gravitational acceleration	$m.s^{-2}$
h:	Heat transfer coefficient	$W.m^{-2}.K^{-1}$
k:	Thermal conductivity/Turbulence kinetic energy	$W.m^{-1}.K^{-1}$ / $m^2.s^{-2}$
L:	Module length	m
n:	Number of attributes/Number of samples	-
P_{pv}:	Module power output/Module power generation	W
q'':	Heat loss per unit area	$W.m^{-2}$
RH:	Rate of humidity	%
S_e:	Volumetric heat source	$W.m^{-3}$
T:	Temperature	°C
T_a:	Ambient temperature	°C
T_c:	Cell temperature	°C
T_{pv}:	Module temperature	°C
t:	Thickness	mm
U:	Heat loss coefficient	$W.m^{-2}.K^{-1}$
V:	Module voltage/Volume	V / m^3
W:	Weights	-
W_d:	Wind direction	deg
W_s:	Wind speed	$m.s^{-1}$
x:	Variable	-
X:	Matrix of values/Input variable	-
y:	Variable	-
Y:	Output variable/Vector of values	-
ϵ:	Error term/Surface emissivity/Turbulence dissipation rate	$m^2.s^{-3}$ / -

Greek Symbols

α:	Thermal diffusivity/Module inclination angle/Regularization coefficient	$m^2.s^{-1}$ / - / °
β	Thermal expansion coefficient	K^{-1}
γ:	Dimensionless coefficient	-
λ:	Regularization coefficient	-
μ:	Temperature coefficient/Viscosity/Module temperature coefficient	%/K / Pa.s / %/°C
ν:	Specific heat capacity	$J.kg^{-1}.K^{-1}$
σ:	Stefan-Boltzmann constant	$W.m^{-2}.K^{-4}$
τα:	Transmittance-absorptance coefficient	-
Φ:	Transfer function	-
ϕ:	Transfer (activation) function	-
η:	Module efficiency	-

Dimensionless numbers

Gr:	Grashof number
Pr:	Prandtl number
Ra:	Rayleigh number
Re:	Reynolds number
Ri:	Richardson number

Subscripts

a:	Ambient
ave:	Average
b/back:	Back
c:	Cell/Critical
conv:	Convection
d:	Direction
exp:	Experimental
f:	Front/Fluid
film:	Film
gr:	Ground
i,j,k:	Index
i,n,p:	Indices
mmp:	Maximum power point

measu: Measured
pred: Predicted
rad: Radiation
ref: Reference
s: Speed/Solid
sky: Sky
surr: Surrounding
t/top: Top

Abbreviations

ANN: Artificial Neural Network
CNN: Convolutional Neural Network
ELM: Extreme Learning Machine
FFNN: Feedforward Neural Network
GPR: Gaussian Process Regression
KRR: Kernel Ridge Regression
LASSO: Least Absolute Shrinkage and Selection Operator
LM: Levenberg-Marquardt algorithm
LSTM: Long-Short Term Memory
MAE: Mean Absolute Error
MAPE: Mean Absolute Percentage Error
MBE: Mean Bias Error
ML: Machine Learning
MLP: Multi-Layer Perceptron
MLR: Multiple-Linear Regression
NOMT: Nominal Operating Module Temperature
NOCT: Nominal Operating Cell Temperature
NTE: Nominal Terrestrial Environment
PCA: Principal Components Analysis
PHANN: Physical Hybrid Artificial Neural Network
PL: Power-Law
PV: Photovoltaic
RANS: Reynolds Averaged Navier-Stokes
RBF: Radial Basis Function
ReLU: Rectified Linear Unit

RMSE:	Root Mean Squared Error
RNN:	Recurrent Neural Network
RPL:	Rational-Power-Law
SE:	Standard Error
STC:	Standard Test Conditions

GENERAL INTRODUCTION

GENERAL INTRODUCTION

BACKGROUND

Driven by the increase in the world's populations and advancements in industry, global warming and climate change have emerged as critical global challenges, primarily caused by the overuse of fossil fuels in energy production and industry. The concentration of CO_2 in the atmosphere has risen dramatically, reaching 419.3 parts per million (ppm) in 2023 [1], around 35% since the 1900s . This has resulted in a global temperature increase of approximately $0.5°C$, and projections suggest a further rise of up to $2°C$ by the end of the century [2], which could lead to catastrophic consequences such as extreme weather events, sea-level rise, and disturbances in ecosystems and human societies. These environmental concerns have driven a global transition toward renewable energies to reduce greenhouse gas emissions and foster a more sustainable energy future.

Algeria, like many other nations, is responding to the challenges posed by climate change by advancing its renewable energy sector. The country's solar potential, with over 3,000 hours of sunshine per year, positions it as a leader in solar energy in the region [3]. To capitalize on this resource, Algeria's Renewable Energy and Energy Efficiency Development Plan aims to install 22 GW of renewable energy capacity between 2011 and 2030 [4], with 13.6 GW expected to come from solar photovoltaics (PV) [5]. As of 2020, Algeria had achieved an installed capacity of 423 MW of solar PV [6], demonstrating its commitment to opting and developing renewable energy.

In this context, the efficiency and performance of PV systems become critical to meet the country's energy goals. PV modules are highly sensitive to environmental conditions such as solar irradiance, ambient temperature, and wind speed, particularly in the desert and arid climate. High module temperatures, in particular, can reduce efficiency and power output. Traditional modeling approaches have struggled to accurately predict photovoltaic modules performance under varying conditions. Therefore, this thesis leverages advanced machine learning models and numerical simulations, including thermal modeling and Computational Fluid Dynamics (CFD), to provide more accurate predictions of PV module behavior, thereby improving energy generation and efficiency. This research contributes to the global effort to optimize solar energy technologies, aligning with Algeria’s renewable energy aspirations and the global movement towards sustainable energy solutions.

SCOPE OF WORK

The scope of this thesis focuses on the development and evaluation of predictive models for photovoltaic (PV) module performance, specifically addressing power output and temperature behavior under varying environmental conditions, such as, solar radiation, ambient temperature, wind speed, and relative humidity. The work encompasses both data-driven modeling using machine learning algorithms and numerical simulations involving thermal modeling and Computational Fluid Dynamics (CFD) analysis. The data-driven approach involves collecting and processing real-world operational data from a PV system, followed by the application of machine learning techniques to predict power output. Simultaneously, the thesis explores thermal modeling to study heat transfer mechanisms in PV modules, complemented by CFD simulations to investigate the impact of ambient factors such as solar radiation, wind speed and ambient temperature, and furthermore investigates the effect of modules’ mounting angle. The combined methodologies provide a comprehensive understanding of the thermal and electrical performance of PV modules, contributing to optimizing their efficiency and reliability under real-world conditions.

OBJECTIVES

The primary objective of this thesis is to develop and evaluate predictive models that can accurately forecast the power output and thermal behavior of photovoltaic modules under various environmental conditions. By integrating data-driven approaches with numerical simulations, this work aims to enhance the understanding of the key factors influencing PV performance, enabling the optimization of solar energy systems for improved efficiency and reliability. The findings are intended to contribute to the broader goal of advancing renewable energy technologies in Algeria and globally, particularly in the context of mitigating climate change. The specific objectives of the thesis are as follows:

- ☞ Develop machine learning models to predict the power output of PV module based on real-time environmental data, including solar irradiance, ambient temperature, and wind speed.
- ☞ Implement and assess the performance of various machine learning algorithms, such as decision trees, random forests, and neural networks, in predicting PV module behavior.

- ☞ Perform thermal modeling to analyze the heat transfer mechanisms within PV modules, focusing on the impact of temperature on efficiency.
- ☞ Conduct CFD simulations using Ansys Fluent to study the effects of ambient parameters, such as wind flow and temperature, on PV module cooling and performance.
- ☞ Integrate data-driven models with numerical simulations to create a comprehensive framework for optimizing PV system performance.
- ☞ Assess the accuracy of the predictive models by comparing their results with experimental data obtained from real-world PV systems.
- ☞ Identify key environmental factors that most significantly affect PV module power output and temperature to improve system design and efficiency.
- ☞ Based on the comprehensive analysis and the obtained results, solutions for enhancing the performance of photovoltaic modules and improving their energy yield can be proposed.

THESIS OUTLINES

In order to convey the study results efficiently and for better understanding of the different steps to accomplish the study objectives, this thesis is decomposed into four chapters, which are structured in the following manner: In CHAPTER I, firstly, the context of the study is presented and highlighted with a basic understanding of the of solar energy, solar radiation, and the photovoltaic conversion. After that, a detailed and extensive review of the previous works in the field of photovoltaics, specifically regarding the prediction of their temperature and power output, and also their modeling using Computational Fluid Dynamics (CFD) and thermal modeling, is reported. Finally, the motivation behind this work is also presented, with a conclusion rounding off the first chapter.

In CHAPTER II, the objective is present the experimental setup that have been used to collect the datasets for this work, and also to present the Machine Learning (ML) algorithms that are being used to predict the operating temperature of the module. Furthermore, the details of data preprocessing, feature engineering and selection, error evaluation, and uncertainty analysis are also presented in CHAPTER II.

After that, in CHAPTER III, the implemented modeling techniques are described and presented in details. Firstly, the physical model for the numerical simulations is depicted, afterwards, the governing equations, boundary conditions, and initial conditions are also presented. Additionally, the implemented approaches for modeling turbulence and radiation are described and moreover, a mesh sensitivity test and model validation are performed in this chapter. Furthermore, and following that, the details of thermal modeling are presented, involving the energy balance modeling approach, modeling radiation and convection heat transfer between the photovoltaic module and its surroundings. Finally, the proposed thermal modeling simulation algorithm is presented and validated.

CHAPTER IV, finally presents and discusses the results of all conducted investigations in this work, starting from the prediction of photovoltaic module power output and its relation with ambient parameters, and more importantly with module temperature, additionally, the results of the study are compared with counterpart models and studies from literature. After that, results regarding module temperature modeling and prediction are presented, discussed and evaluated. Firstly, findings of data driven modeling and prediction of module temperature via twelve different machine learning algorithms were presented with comparison to literature, and similarly, results of another two studies, involving CFD simulations and thermal modeling were presented and evaluated against both experimental data and literature models and studies.

The final section of the thesis will incorporate the GENERAL CONCLUSION of this work and some recommendations and perspectives for future works

CHAPTER I : INTRODUCTION AND LITERATURE REVIEW

I.1 Introduction

In CHAPTER I, the objective is to provide a concise introduction to the topic of solar to electrical energy conversion using solar photovoltaics, where the need of transition from fossil fuels to renewable energy sources will be highlighted. Additionally, the role of solar photovoltaics energy in this transition process will be presented, with a brief introduction to the technology of solar photovoltaic conversion, solar energy and the basics of solar radiation. Furthermore, CHAPTER I will also present a detailed review of most recent and related works in the field of solar photovoltaic power output prediction and its relation to ambient and operating parameters such as solar radiation and module temperature. The latter is a key parameter in this study, there for related work considering module temperature in literature are also reviewed, which is the starting point for current work.

I.2 Global energy needs

In order to meet its energy requirements, currently, the world depends heavily on fossil fuels, which are environmentally unfriendly and non-renewable energy sources. The world's expected total delivered energy consumption in 2025 based on end-use sectors and fuel type is shown in Table I.1. As it can be seen in Figure I.1, the industrial sector consumes over 53% of the total energy, while the second most energy consuming sector is transportation with over 25%, followed by residential and commercial sectors with 13.48 and 7.26%, respectively [7].

Based on the 2025 forecasting of energy the global energy consumption shown in Figure I.2, it can be seen that 78% of the total energy is supplied by fossil fuels, with 23% of it by Coal, 23% using Natural gas, and 3 using Oil. On the other hand, 17% of the total energy will be delivered using renewable energy sources, while Nuclear energy will deliver the remaining 5% [7]. Additionally, and according to the International Energy Outlook 2023, the growth in global population -along with other factors- will affect energy consumption in several ways, where the world's population is expected to grow from 7.9 billion in 2022 to 9.6 billion in 2050, which will cause the energy consumption to increase globally [2]. In the World Energy Outlook, the forecasts show lower fossil fuel demand due to current policies, economic changes, and the 2022 energy crisis. Clean energy is rapidly replacing fossil fuels, and for the first time, all fossil fuels (Natural gas, Oil, and Coal) are expected to peak by 2030. This shift, driven by clean energy growth and efficiency improvements, leads to a decline in fossil fuel use and brings the peak in CO2 emissions forward to the mid-2020s [2].

Table I.1: World Delivered Energy Consumption by End-Use Sector and Fuel in 2025* [7].

Fuel	Total	Electricity	Residential	Commercial	Industrial	Transport	All End-Use Sectors
Oil	207.8	7.1	9.7	3.9	69.6	118.4	201.7
Natural gas	151.3	49.5	24.6	10.6	63.3	4.7	103.1
Coal	153.4	83.2	5.2	1.7	65.9	0.0	72.9
Nuclear	30.9	30.0	—	—	—	—	—
Electricity	—	—	24.9	19.0	40.3	1.9	86.2
Renewables	110.5	83.9	1.5	0.3	23.4	0.0	25.2
Total	653.8	253.6	65.9	35.5	262.5	125.0	489.0

*Values are in Quad Btu (quadrillion Btu). (1 quadrillion Btu = 1 × 10^{15} Btu = 0.95 × 10^{15} kJ)

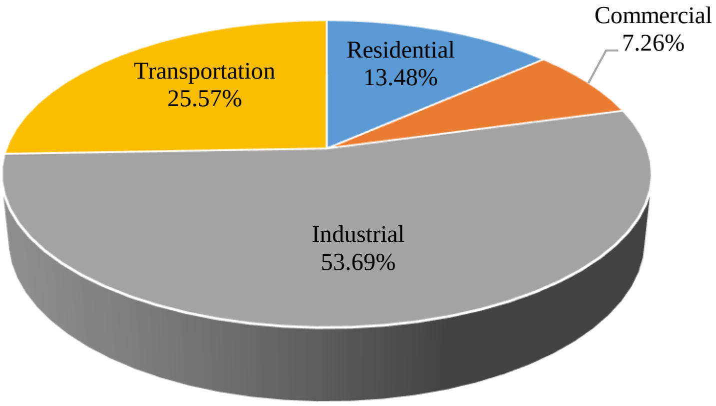

Figure I.1: Distribution of expected energy consumption for 2025 in percentage [7].

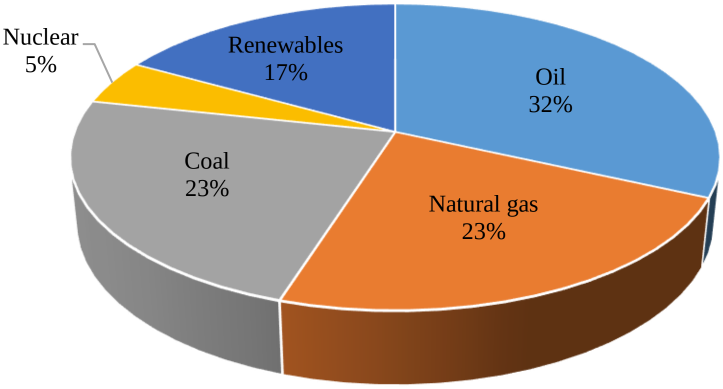

Figure I.2: The world’s energy supply by fuel (expected for 2025) [7].

I.3 Fossil fuel combustion

Fossil fuels have been powering the industrial development since the 1700s, but have caused significant environmental damage, including smog, acid rain, and air pollution, which pose threats to human health and ecosystems [8]. CO2, the primary greenhouse gas, has increased by 20% over the past century, reaching 410 ppm in 2019, driving global warming. The Earth's temperature has already risen by 0.5°C and is projected to increase by another 2°C by 2100, leading to severe consequences like extreme weather, rising sea levels, and ecosystem disruption, where currently, governments are taking actions and setting policies to limit that temperature rise to 1.5°C [2]. Generally, to address these challenges, a shift to renewable energy sources, such as solar and wind, alongside improvements in energy efficiency, is essential. Energy efficiency helps reduce fossil fuel consumption, while renewable energy can directly replace it [8].

I.4 Renewable energy

In order to deal with the challenges raised by the extensive use of fossil fuels over the past centuries, many alternative energy sources can replace fossil fuels, with the choice of energy source depending on economic, environmental, and safety considerations.

As the global economic expansion continues, energy demand is expected to rise, even with efforts to improve energy efficiency. Renewable energy technologies are now seen as capable of meeting this increasing demand at prices comparable to or lower than conventional energy sources. By the mid-21st century, renewables could represent a significant share of the global electricity market and fuel consumption [9].

Transitioning to a renewable energy-intensive economy offers environmental benefits not captured by traditional economic measures. An analysis by Johanson et al. [10] projected that widespread adoption of energy efficiency and renewable energies could reduce global carbon dioxide emissions by 75% compared to 1985 levels by 2050, potentially at no additional cost, as renewable energy is expected to be competitive with fossil fuels [10].

Solar energy is particularly favored due to its sustainable and environmentally friendly characteristics [9].

I.5 Solar energy

The sun is a massive sphere of hot gas, with a diameter of 1.39×10^9 m, located about 1.5×10^{11} m from Earth. It rotates on its axis approximately every 27 days at the equator and every 30 days at the poles. With an effective surface temperature of 5777 K, the sun functions as a continuous fusion reactor. In its core, temperatures range between 8×10^6 and 40×10^6 K, with a density about 100 times that of water. The primary fusion process involves hydrogen nuclei combining to form helium, releasing energy. This energy travels outward from the core through radiative and convective processes, eventually being emitted as radiation across the spectrum, including x-rays and gamma rays [11]. where, $h = 6.63 \times 10^{-34}\, Ws^2$ is Planck's constant, $c = 3.00 \times 10^8\, m/s$ the speed of light, and $k = 1.38 \times 10^{-23}\, J/K$ Boltzmann's constant. As this energy travels 150 million kilometers to Earth, the total energy density decreases to 1367 W/m^2, known as the solar constant [12].

I.5.1 Solar radiation

The process of converting solar energy into other more useful types of energy can be performed mainly via three process of conversion [8]:

- Heliochemical process: It is essentially a photosynthesis process, which is the reason of producing biomass and fossil fuel.

- Heliothermal process: Where the energy received from the sun is collected and converted to heat or thermal energy. Common devices that collect solar energy and convert it to thermal energy are concentrating collectors, Flat-plate collectors, and heliostats. While solar collectors are useful for heating and cooling of residential spaces and heating and producing hot water for buildings, Heliostats are mirrors reflecting solar radiation into a single receiver, where its high temperature thermal energy is used to produce electricity via a heat engine.

- Helioelectrical process: Which is the process of generating electricity using solar cells via the photovoltaic effect. The process is different from heliostats, where solar energy is first converted to thermal energy whereas in the helioelectrical process, solar energy is directly converted to electricity in solar cells.

I.5.2 Fundamentals of radiation

In 1864, physicist James Clerk Maxwell laid the theoretical groundwork for radiation by proposing that accelerated charges or changing electric currents generate electric and magnetic fields. These fields form electromagnetic waves (or radiation), representing energy emitted by matter due to changes in the electronic structure of atoms or molecules [13].

I.5.2.1 Electromagnetic radiation

In 1887, Heinrich Hertz confirmed the existence of these waves through experiments. Electromagnetic waves carry energy and travel at the speed of light in a vacuum, $c = 3.00 \times 10^8\, m/s$. They are characterized by their frequency (ν) and wavelength (λ), which are related by the equation [13]:

$$\lambda = \frac{c}{\nu} \tag{I.1}$$

I.5.2.2 Planck's quantum theory

Max Planck's quantum theory, introduced in 1900, proposed that electromagnetic radiation can be understood as a collection of discrete energy packets called photons or quanta. Each photon of frequency v has an energy given by the equation [13]:

$$e \;=\; hv \;= \frac{hc}{v} \tag{I.2}$$

This relation shows that photon energy is inversely proportional to wavelength, meaning shorter-wavelength radiation carries more energy.

I.5.2.3 Blackbody radiation and the sun

The Sun generates energy through the fusion of hydrogen into helium, converting mass into energy according to Einstein's equation, $E = mc^2$. This process maintains the Sun's surface temperature at about $5800\, K$. The energy is radiated uniformly in all directions, consistent with Planck's blackbody radiation law. The energy density per unit area as a function of wavelength, λ, can be calculated using Planck's formula as follows:

$$w_\lambda = \frac{2\pi hc^2\lambda^{-5}}{e^{(hc/\lambda kT)} - 1} \tag{I.3}$$

I.5.3 Radiative properties

Most common materials, like metals, wood, and bricks, are opaque to thermal radiation, which makes radiation a surface phenomenon for them, meaning it is emitted or absorbed within the first few micrometers of the surface. However, materials such as glass and water allow visible radiation to penetrate to significant depths before absorption occurs, making radiation a volume phenomenon in these semitransparent materials. Despite this, both glass and water are nearly opaque to infrared (IR) radiation. The behavior of materials varies with wavelength, making properties like emissivity, absorptivity, reflectivity, and transmissivity wavelength-dependent. A blackbody, which is a perfect emitter and absorber of radiation, is used as a reference when describing the radiation characteristics of real surfaces [8].

I.5.3.1 Emissivity

Emissivity represents the ratio of radiation emitted by a surface at a given temperature to the radiation emitted by a blackbody at the same temperature. It is denoted by ε, and it ranges between 0 and 1, where $\varepsilon = 1$ corresponds to a perfect blackbody. Emissivity measures how closely a real surface approximates a blackbody. Metals generally have low emissivities, as low as 0.02 for polished surfaces, while nonmetals, such as ceramics and organic materials, tend to have higher emissivities. The emissivity of metals increases with temperature, and oxidation can significantly raise it. Heavily oxidized metals may have emissivities similar to nonmetals [8].

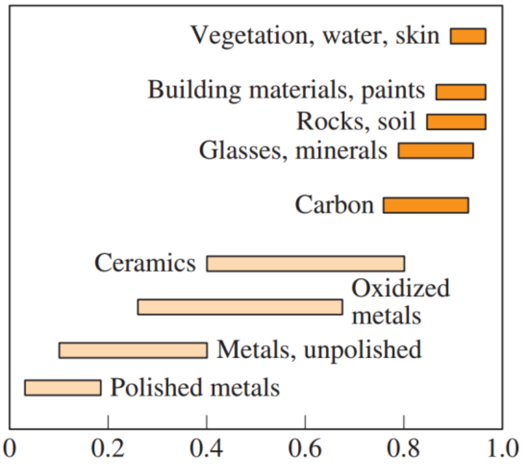

Figure I.3: Typical emissivity of some materials [8].

I.5.3.2 Absorptivity, Reflectivity, and Transmissivity

Everything around us constantly emits radiation, and emissivity describes the emission characteristics of these bodies. This means that everything, including our own bodies, is continuously bombarded by radiation from all directions across various wavelengths. The radiation flux hitting a surface from all directions is called irradiation or incident radiation, denoted by G. It represents the rate at which radiation energy is incident on a surface per unit area. When radiation strikes a surface, part of it is absorbed, part is reflected, and the rest, if any, is transmitted [8].

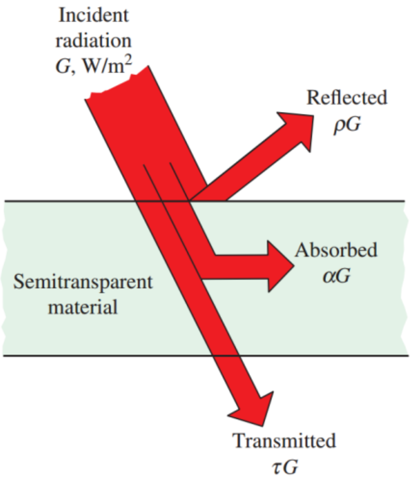

Figure I.4: Absorption, reflection, and transmission of radiation by a semitransparent material [8].

I.5.3.3 The view factor

Radiative heat transfer between surfaces is influenced by the relative positioning of the surfaces, along with their thermal radiation properties and temperatures [14]. Therefore, it is important to introduce the concept of view factor, which is defined as the fraction of the radiation leaving surface i that is intercepted by surface j [15]. The general equation for the view factor F_{ij} from surface A_i to surface A_j is given by [15]:

$$F_{ij} = \frac{1}{A_i} \int_{A_i} \int_{A_j} \frac{cos\theta_i cos\theta_j}{\pi r^2} dA_j dA_i \tag{I.4}$$

where A_i and $A_j$are the areas of surfaces i and j, θ_i and $\theta_j$are the angles between the line connecting differential areas on the two surfaces and the normal to those surfaces, r is the distance between them, and dA_i and dA_j are the differential areas on surfaces A_i and A_j.

I.5.4 Thermal conversion

The conversion of the sun’s radiant energy to heat has been practiced since historical times and has developed into a sophisticated solar conversion technology today. The fundamental principle of solar thermal collection involves solar radiation striking a surface, where a portion is absorbed, increasing the surface’s temperature. The efficiency of a solar collector depends on its ability to absorb solar radiation, minimize thermal and reradiation losses, and effectively transfer the collected energy for practical use. Solar thermal collectors range from unglazed flat-plate collectors, which operate at about 5°C–10°C above ambient temperature, to central receiver concentrating collectors that can exceed 1000°C. Different types of solar thermal collectors, along with their temperature and concentration ranges, are detailed in Table I.2 [16].

Table I.2: Typical temperature range for solar thermal collectors [16].

Type of Collector	Concentration Ratio	Typical Working Temperature Range (°C)
Flat-plate collector	1	≤70
High-efficiency flat-plate collector	1	60–120
Fixed concentrator	3–5	100–150
Parabolic trough collector	10–50	150–350
Parabolic dish collector	200–500	250–700
Central receiver	500 to >3000	500 to >1000

I.5.4.1 Principles of Solar-Thermal conversion

Solar energy is converted into thermal energy using solar thermal collectors, which capture radiation and transfer it to a fluid within the collector tubes [17].

As shown in Fig. 2.9, the temperature of the fluid rises, allowing the stored thermal energy to be utilized for various industrial processes and applications [18]. This stored energy can be used when needed, making solar thermal power a flexible and efficient solution for a range of industrial needs [17].

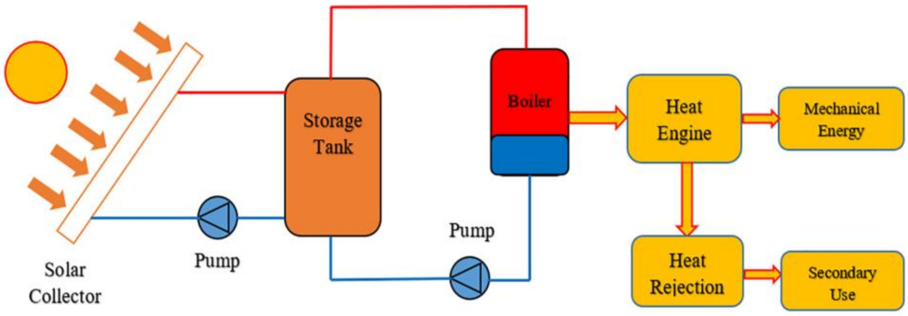

Figure I.5: Diagram of solar-thermal conversion system [18].

I.5.4.2 Types of Solar-Thermal systems

Thermal solar technologies are classified into low, medium, and high-temperature systems. Next is brief description of this classifications [19]:

Low-temperature systems heat fluids below 100°C, commonly used for producing domestic hot water, space heating, swimming pool heating, and low-temperature industrial applications like maintaining fluid temperatures in tanks [19].

Medium-temperature systems operate between 100°C and 250°C. Though not as widespread, their most common use is in solar ovens for cooking. These systems are less commonly applied in other areas [19].

High-temperature systems involve concentrating solar energy to heat fluids above 250°C, primarily in Concentrated Solar Power (CSP) technology. CSP systems are employed in generating electricity through thermodynamic cycles, where the heat is converted into mechanical energy to drive turbines. Additionally, CSP is used in high-temperature chemical processes such as hydrogen production. These technologies offer significant potential for renewable energy generation and reducing dependency on fossil fuels, especially in industrial and power-generation sectors [19].

I.5.4.3 Applications of Solar-Thermal energy

Solar thermal collectors convert solar radiation into heat energy, which is transferred to a working fluid like air or water. This heat can be used directly for water heating or space heating/cooling systems or stored in thermal containers for use during the night or cloudy days [20].

Solar collectors are classified into two types: concentrating and non-concentrating. Non-concentrating collectors have the same intercepting and absorber areas, while concentrating collectors use reflective surfaces to focus sunlight on a smaller area, increasing heat flux. Various designs of solar thermal collectors exist, with differences in orientation, efficiency factors, and applications [18]. The following is some of the applications for solar thermal energy conversion.

a) Flat-plate solar collector

The primary goal of a solar collector is to generate useful heat from solar energy, with the majority being used for hot water production. This hot water is typically utilized in residential and commercial buildings for kitchens, bathrooms, and showers Figure I.6. Solar collectors can also contribute to space heating during winter, though the peak availability of solar heat coincides with summer when heating is less needed. As a result, most solar collectors focus on hot water production and are widely used in regions like southern Europe and Asia, where solar energy is abundant for over 200 days annually [8].

Figure I.6: Water heating solar collectors on the roofs of residential buildings [8].

b) Concentrating solar collector

Concentrating collectors consist of two main components: concentrators and receivers. Various designs for both are available commercially. Concentrators can be refractive or reflective, continuous or non-continuous, and can take cylindrical or parabolic shapes. Similarly, receivers can be flat, convex, concave, or cylindrical, with or without glazing. The positioning of the optical system in concentrating collectors is crucial due to the sun's movement throughout the day [18]. Concentrating collectors offer several advantages over non-concentrating collectors, including higher efficiency and improved performance [21].

Concentrating collectors are typically classified into four main types: Parabolic Trough Collector (PTC), Linear Fresnel Reflector (LFR), Parabolic Dish Reflector (PDR), and Central Receiver or Heliostat Field Reflector (HFR) [18].

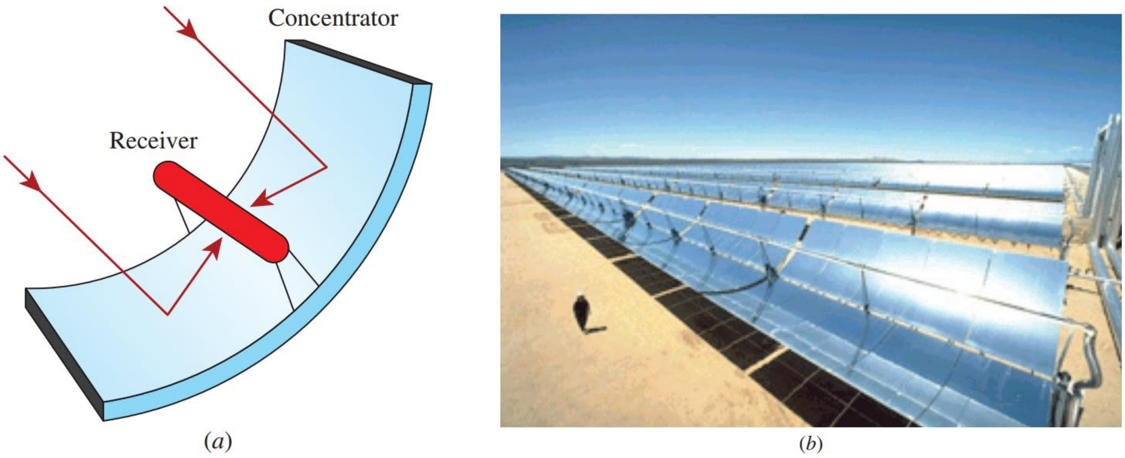

Figure I.7: Parabolic trough collector. (a) Schematic diagram, and (b) Photo [8].

c) Solar-power-tower plant

A solar power tower plant utilizes an extensive array of mirrors, known as heliostats, which track the sun and reflect solar radiation onto a receiver positioned at the top of a tower Figure I.8. In this system, water is heated, boiled, and superheated by the receiver's absorbed solar heat. The generated steam is then directed to a turbine to produce mechanical power. A generator, connected to the turbine, converts this mechanical power into electricity [8].

Figure I.8: A solar-power-tower plant [8].

d) Solar pond

A promising method of generating power involves using solar ponds, which are large artificial lakes a few meters deep that collect and store solar energy. In these ponds, solar energy is absorbed throughout, causing the water temperature to rise uniformly. However, the surface layer of the pond loses much of its heat to the atmosphere, cooling down and acting as insulation for the hotter water below, which helps to trap energy at the bottom. Typically, salt is added to the bottom layer to prevent the hot water from rising to the surface. Power plants can then utilize an organic fluid, such as alcohol, as the working fluid, operating between the upper and lower layers of the pond [8].

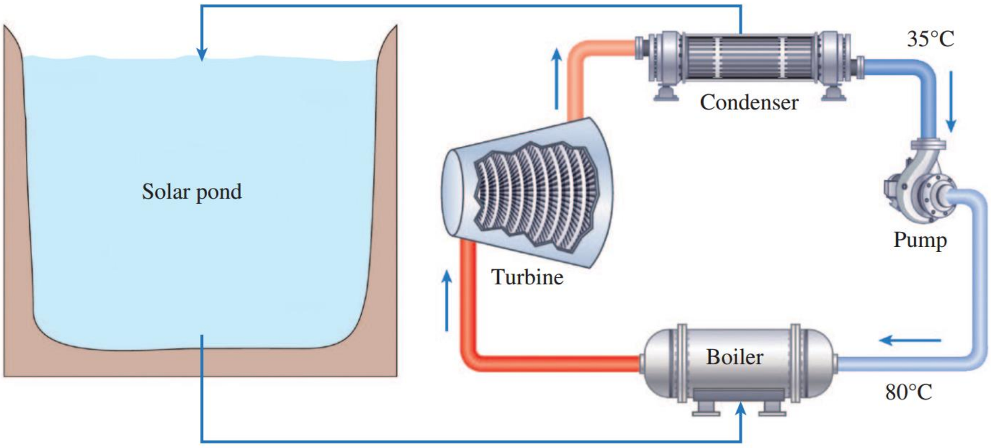

Figure I.9: Operating principle of a solar pond power plant [8].

I.5.4.4 Advantages and challenges

The use of solar energy as a thermal source several applications such as heating water and domestic spaces, have several advantages over the use of fossil fuels for those purposes. However, it may also have some disadvantages, the following is a listing of those advantages and disadvantages:

a) Advantages

- Low operational costs
- scalable for large projects
- reduces fossil fuel dependency.

b) Disadvantages

- High initial costs
- Geographic and climatic limitations
- Energy storage issues.

I.5.5 Photovoltaic conversion

Photovoltaic (PV) conversion directly transforms sunlight into electricity without the need for a heat engine. PV devices are solid-state, making them durable, simple to design, and requiring minimal maintenance [16].

Their greatest advantage is their versatility, as they can be built as stand-alone systems with outputs ranging from microwatts to megawatts. This adaptability has led to their use in a variety of applications, including calculators, watches, water pumps, remote buildings, satellites, and even large-scale power plants. PV panels can also be integrated into building structures, like roof shingles and wall panels. Consequently, the demand for photovoltaics is growing every year [16].

The photoelectric effect was first observed by Becquerel in 1839 [22], when light struck an electrode in an electrolyte solution. In 1877, Adams and Day discovered the effect in solids while working with selenium. Early studies on materials like selenium and copper oxide were conducted by pioneers such as Schottky, Lange, and Grandahl. In 1954, researchers at RCA and Bell Laboratories achieved approximately 6% efficiency using devices made from p-type and n-type semiconductors, marking a significant advancement in the field [16].

I.5.5.1 Principles of Photovoltaic conversion

A basic knowledge of atomic structure is essential for understanding the behavior of semiconductors and their application in PV energy conversion devices. Most introductory physics or chemistry textbooks provide sufficient background for this foundational understanding. Below is a brief overview of the key principles of photovoltaic conversion, applications, and advantages.

a) Semiconductors

A basic understanding of atomic structure is essential for grasping how semiconductors function in photovoltaic (PV) energy conversion devices. Electrons in an atom arrange themselves in orbitals around the nucleus, with the innermost electrons requiring the most energy to become free. The outermost electrons, found in the valence band, participate in bonding with neighboring atoms, forming either ionic or covalent bonds depending on their attachment. When electrons in the valence band gain enough energy, they can jump into the conduction band, where they are responsible for conducting heat and electricity. The energy difference between the valence and conduction bands is known as the band gap [16].

Materials with full valence bands and large band gaps (>3 eV) are insulators, while those with partly filled valence bands and intermediate band gaps (≤3 eV) are semiconductors (Figure I.10). Pure semiconductors are intrinsic, while semiconductors doped with impurities are extrinsic. If a material is doped with atoms that have more valence electrons, it becomes an n-type semiconductor (with excess electrons). Conversely, doping with atoms that have fewer valence electrons creates a p-type semiconductor (with positive holes). These n- and p-type materials facilitate electron and hole movement, critical for semiconductor behavior in PV devices [16].

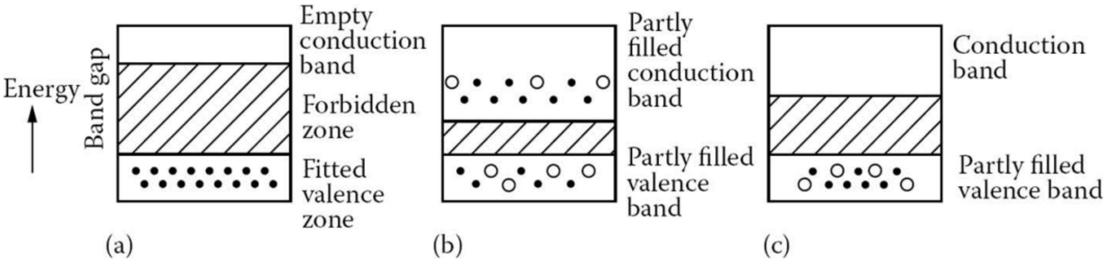

Figure I.10: Electrical conduction is described in terms of allowed and forbidden energy bands. Band gap for insulators (a) is the highest, followed by semiconductors (c) and metals (b), respectively [16].

b) P–N Junction

The fundamental requirement for photovoltaic energy conversion is the presence of electronic asymmetry in the semiconductor structure, known as a junction. When n-type and p-type semiconductors come into contact, electrons from the n-region near the junction move to the p-type semiconductor, leaving a positively charged layer behind. Similarly, holes flow in the opposite direction, creating a negatively charged layer. Eventually, a steady state is reached, forming a junction with almost no mobile charges, called the depletion region [23].

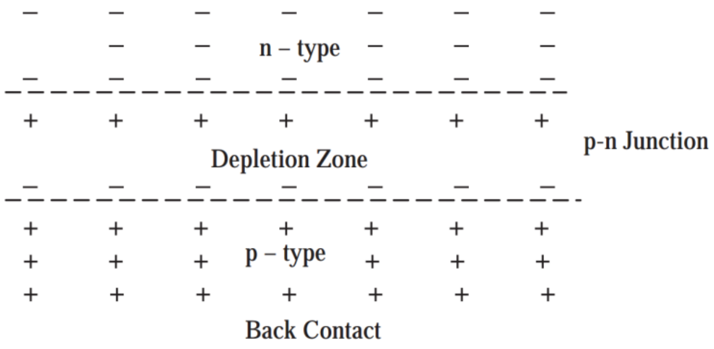

Figure I.11: Diagram of a p-n junction [23].

c) PV effect

When a photon is absorbed by a valence electron, the electron's energy increases by the photon's energy. If the photon's energy is equal to or greater than the semiconductor's band gap, the electron jumps into the conduction band, allowing it to move freely. If the photon's energy is less than the band gap, the electron remains in place, and the excess energy becomes kinetic energy, increasing the temperature. If the photon energy exceeds the band gap, the excess energy also converts to kinetic energy. Importantly, a photon can free only one electron, even if its energy is much higher than the band gap, which limits the efficiency of photovoltaic (PV) devices [16]. The key to generating power from the PV effect is to direct the free electrons through an external circuit before they recombine with holes, which is achieved via the p-n junction. In a PV device, as photons generate free electrons in the n-type layer, these electrons can flow through an external circuit, recombine laterally with holes, or move toward the p-type layer. However, the negative charges at the p-n junction prevent this movement. Making the n-layer very thin reduces the chances of recombination within it unless the external circuit is open. If the circuit is open, the electrons eventually recombine with holes, leading to an increase in temperature [16].

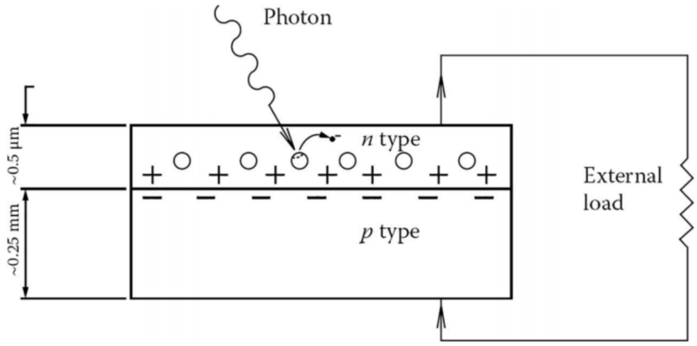

Figure I.12: Schematic diagram of a PV device [16].

I.5.5.2 Types of PV systems

Photovoltaic power systems are typically classified based on their function, operation, component configurations, and connection to power sources and loads. The two main types are grid-connected (utility-interactive) and stand-alone systems. The following is brief description of those types.

a) Grid-connected PV systems

Grid-connected utility-interactive PV systems can supply power directly to the utility grid. These systems fall into two main categories: those without battery backup and those with battery backup. Systems with battery backup are further classified into DC-coupled and AC-coupled systems. In some instances, battery backup systems do not sell power back to the grid but only draw power from it to charge the batteries [12].

b) Stand-alone PV systems

Stand-alone PV systems and grid-connected, battery-backup systems share similarities, especially when a grid-connected system disconnects and functions independently. Stand-alone systems offer more design flexibility, supporting a mix of DC and AC loads, and often include more days of battery storage since they lack grid support. Unlike grid-connected systems, which don’t require precise array tilt, stand-alone systems may need seasonal optimization and backup generation for reliable year-round performance, especially in extreme climates [12].

c) Hybrid solar systems

Hybrid solar systems combine the benefits of both on-grid and off-grid systems by incorporating battery storage while remaining connected to the grid. These systems can operate independently but rely on the grid for backup when solar production is low, such as during rainy seasons. On sunny days, any excess solar energy is stored in the batteries, allowing it to be used during periods of high demand, power outages, or low solar output.

I.5.5.3 Efficiency and performance of PV systems

Several key factors play a crucial role in determining the performance and efficiency of the solar to electrical energy conversion process, one of which is the module operating temperature [24-26]. The latter is influenced by various environmental conditions where the photovoltaic module is situated, and it is well established that parameters such as ambient temperature, wind speed, and solar radiation can significantly affect it [27-30].

Currently, single-junction solar PV cells have an efficiency range of 15% to 28%, with a theoretical maximum of 33.16%. This means that only 15 to 28 watts of energy are converted into electricity for every 100 watts of sunlight, with the rest lost as heat or due to reflection and refraction. Multiple PV cells are combined in series or parallel to form a module, but module efficiency is lower than cell efficiency, as it is shown in , due to energy losses from spacing, mounting, and accessories [31].

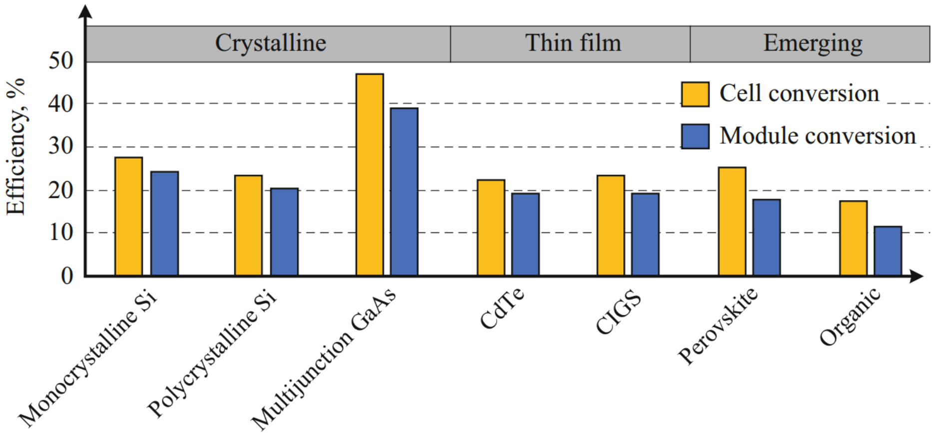

Figure I.13: Comparison of efficiencies for different types of photovoltaic cells and modules [31].

In 2020, Hanwha Q Cells set a record with 20.4% module efficiency in silicon-based polycrystalline technology. Solar PV efficiency has been rising steadily, driven by research and development, particularly in concentrator systems, crystalline silicon, and thin-film PV technologies. For example, the efficiency of concentrator systems increased from 14% in 1995 to 25% in 2020 and is expected to grow further [31].

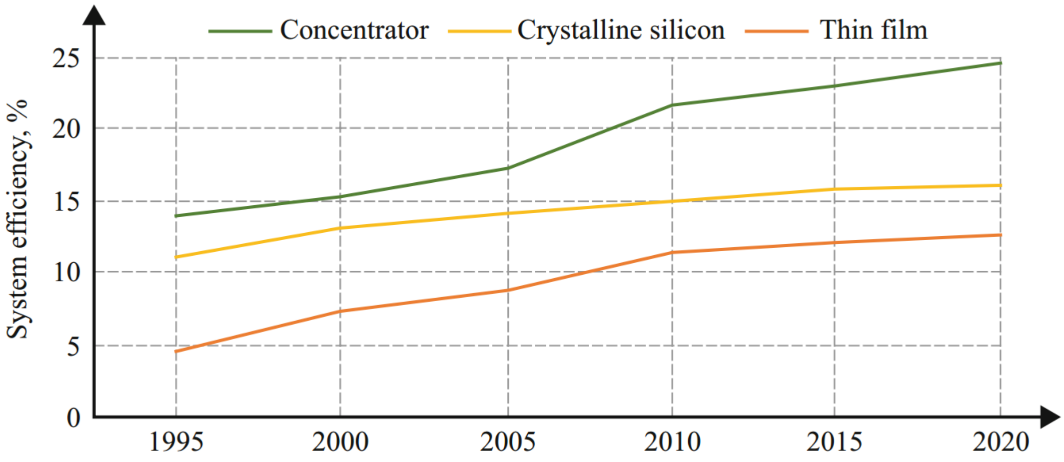

Figure I.14: The increase in efficiency of photovoltaic systems between 1995 and 2020 [31].

I.5.5.4 Applications of PV systems

The scientific community has made significant efforts to explore alternative and clean energy resources due to the limitations of conventional sources. Renewable energy is essential for sustainable economic growth while preserving the environment for future generations. Advances in photovoltaic (PV) technologies have helped bridge the gap between energy supply and demand, especially in emerging applications. Several PV technologies now cater to the increasing energy demand, including solar PV water pumping, home lighting systems, desalination plants, PV thermal systems, space technology, building-integrated PV, and concentrated PV systems. These advancements are contributing to real-world applications and meeting current and future energy needs [32].

I.5.5.5 Advantages and challenges

Despite their significant advantages over fossil fuels, as photovoltaics depend on clean renewable energy sources, they still may have some disadvantages. The following is a listing of some advantages and disadvantages of photovoltaics [33]:

d) Advantages:

- Vast, widely accessible, and nearly infinite fuel source (sunlight).
- No emissions, combustion, or radioactive waste; minimal impact on climate change and pollution.
- Low operating costs due to no fuel requirement.
- No moving parts, leading to minimal wear and a potentially everlasting lifespan.
- Operates at ambient temperatures, avoiding high-temperature corrosion or safety concerns.
- High reliability, with solar modules often guaranteed for over 30 years.
- Predictable annual energy output.
- Modular design allows for flexible installation in small or large systems.
- Can be integrated into both new and existing buildings.
- Quick and easy installation at most points of use.

e) Disadvantages

- Sunlight is a diffuse, low-density energy source.
- High initial installation costs.
- Unpredictable energy output on an hourly or daily basis.
- Lack of cost-effective and efficient energy storage solutions.

I.6 Literature review

Photovoltaic (PV) technology offers a highly convenient way to generate a very desirable form of energy—electricity—directly from sunlight. Despite its advantages, PV technology still faces limitations in performance, making it a central focus in by scientist, engineers, and researchers. This energy conversion process and its efficiency is impacted by various climatic and environmental factors, such as, ambient temperature, solar radiation, wind speed, humidity, and dust, each affecting the power output of a PV panel [34-36]. Power output is critical for the stability and consistency of energy systems, as well as for economic considerations. However, predicting this output presents complexities and nonlinearities, largely due to the unpredictable and often correlated nature of ambient factors like wind speed, which exhibit non-deterministic characteristics. In predictive and forecasting challenges, generally, statistical analysis and regression are frequently used, alongside machine learning and data science. These techniques have become more effective due to advancements in data science, data collection, and modern computational capabilities. Such progress has been crucial in addressing the challenges of PV power forecasting and managing its stochastic, uncontrollable nature caused by variations and uncertainties in solar radiation [37], Researchers and engineers are increasingly leveraging recent advancements in data science, machine learning, and artificial neural networks (ANN) [38-41]. The following section outlines various approaches developed over the past decade to predict the power output and temperature of photovoltaic systems.

I.6.1 Photovoltaic power output

Rosell and Ibanez [42] proposed an approach for predicting PV electricity generation based on the $\mathrm{I}-\mathrm{V}$ curve and a customized expression for maximum power output. According to the findings of the study, the adapted model of $\mathrm{I}-\mathrm{V}$ curve closely aligned with measured data, and the suggested power production equation outperformed the classical model across all operating conditions, offering more accurate predictions and improved reliability. Mellit et al. [43] introduced two models of artificial neural network (ANN) to evaluate the power output of a polycrystalline photovoltaic module, using the experimental setup shown in Figure I.15. The models were developed to predict power production under two distinct conditions: cloudy and sunny days. The results demonstrated that both models provided reasonably accurate predictions. Further analysis revealed that ANNs outperformed conventional methods such as regression, the one-diode model, and analytical approaches, offering superior accuracy in power estimation.

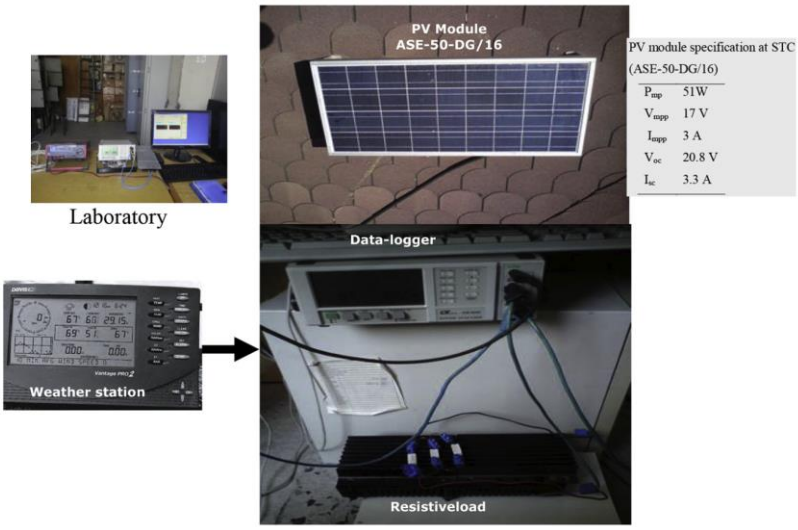

Figure I.15: Experimental setup used by Mellit et al. [43].

Moreover, De Giorgi et al. [44] used multiple regression and artificial neural networks (ANNs) to estimate the power output of a 960 kW grid-connected photovoltaic system. Their analysis showed that using all climatic parameters in the vector of input produced the optimal performance, indicating that predictions were enhanced when all relevant variables were included. Similarly, Dolara et al. [45] introduced a hybrid approach named the Physical Hybrid ANN (PHANN) and compared it to the usual ANN for forecasting day-ahead power production from a PV plant. Their results demonstrated that the hybrid method was more accurate, with error trends revealing superior performance compared to the standard ANN. Additionally, Almeida et al. [46] proposed a procedure utilizing a non-parametric PV model. This model used weather forecast variables alongside the AC power delivered by the power plant, showing that incorporating solar radiation data improved prediction accuracy, while adding more numerical weather forecasts did not necessarily improve results. For hourly predictions, the coefficient of variation for MAE was less than 9.5%. Finally, Qasrawi and Awad [47] employed a Multilayer Feed-Forward Backpropagation Neural Network model to predict the solar cells’ future output, achieving high prediction accuracy.

Graditi et al. [48] conducted a comparative investigation on three approaches to estimate power plant output, focusing on a model from Sandia National Labs, a Multi-Layer Perceptron (MLP) neural network, and a regression analysis. The study results revealed that better and accurate predictions were achieved with the regression and MLP models. Additionally, datasets selected using a genetic algorithm produced better results compared to randomly chosen datasets. Pulipaka et al. [49] modeled the soiling effects on PV modules using ANN and regression analysis techniques, incorporating particle size composition to estimate photovoltaic power output under varying soiling conditions. Their findings indicated that ANNs performed slightly better than regression, though inconsistently. The study also found that small particles influenced power generation at low irradiance levels, while larger particles had a more significant effect at higher irradiances. Leva et al. [50] performed an investigation on a 24h ahead prediction of PV power output as shown in Figure I.16. The study aimed to predict power generation using weather forecasts, with a focus on evaluating the method’s accuracy through the training data and error indicators. It was determined that the accuracy of the method was significantly influenced by the data pre-processing steps and the quality of the training data utilized. Furthermore, it was observed that predictions for sunny days demonstrated higher accuracy compared to those for cloudy and partially cloudy conditions.

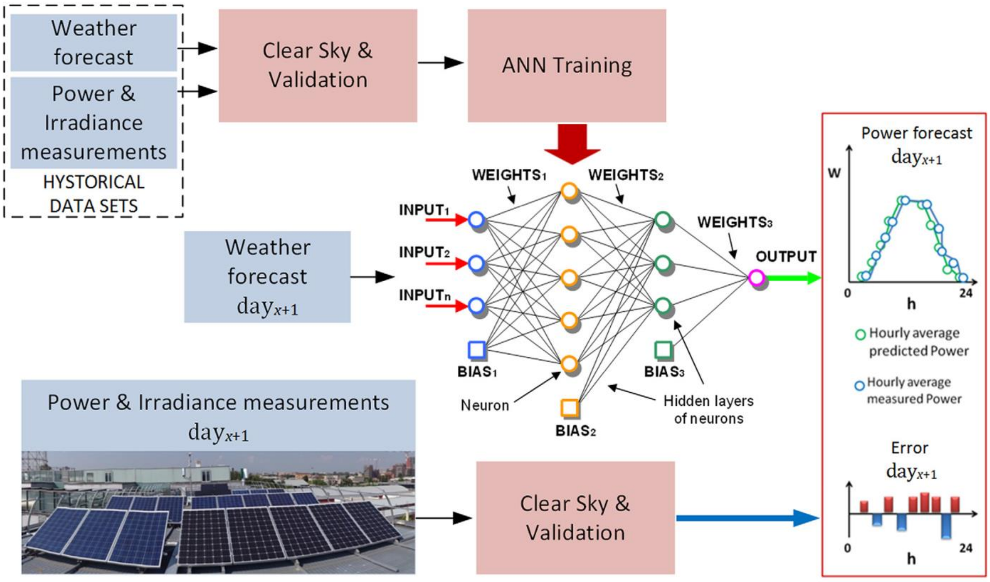

Figure I.16: Work-flow diagram of the study conducted by Leva et al. [50].

Liu et al. [51] examined the photovoltaic system power output forecasting employing a backpropagation network, incorporating various input variables to predict the generated power. Their method demonstrated reliable daily power output predictions, which is highly beneficial for PV system planning. Moslehi et al. [52] conducted research comparing different models for PV power output prediction, exploring the effects of measured module temperature and irradiation on horizontal surfaces instead of the array plane. They also assessed variables like wind speed and found that neither module temperature nor wind speed measurements reliably enhanced inverse solar PV models. The study concluded that directly estimating the power output using climatic data was more reliable than using operating cell temperature, as temperature measurements did not improve model predictions without more representative data. Alomari et al. [53] examined the prediction of photovoltaic power output in Jordan via ANNs, showing that machine learning can effectively predict it based on various weather parameters. Similarly, Behera et al. [54] developed a method to optimize PV power forecasting by refining extreme learning machine (ELM) models. Their findings indicated that ELM outperformed traditional backpropagation neural networks and that using accelerated particle swarm optimization further improved its performance.

Durrani et al. [55] conducted an investigation to forecast photovoltaic power output using solar radiation predictions through multiple feed-forward neural networks (FFNNs). Their research focused on opting the approach shown in Figure I.17, the forecasted global horizontal irradiation, generated through multiple neural networks, was chosen to predict the power output of the PV system, achieving mean absolute percentage errors of 3% for sunny days and 23% for cloudy days. Additionally, the study found that the PV power forecasts using this proposed system outperformed those produced by the photovoltaic persistence power forecast model.

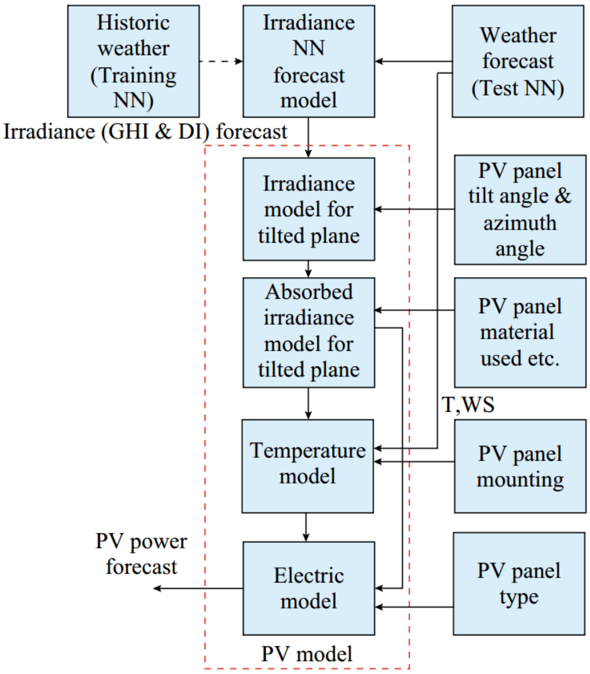

Figure I.17: The prediction approach considered by Durrani et al. [55].

Kayri and Gencoglu [56] examined power output forecasting from a single-axis PV system using ANN, in which that dataset was categorized into sunny and cloudy conditions and assessed independently in the ANN. Based on various statistical metrics, their findings indicated that FFNNs with a backpropagation algorithm demonstrated strong predictive capabilities. Additionally, while the model performed more accurately on sunny days than cloudy ones, the difference between models was minimal. De Jesús et al. [57] introduced a hybrid deep learning model that combined a convolutional neural network (CNN) with long-short term memory (LSTM) to estimate solar PV power, utilizing historical photovoltaic power output and weather data. This model outperformed CNN and RNN models due to its feature extraction capabilities from raw data.

Gómez et al. [58] conducted an investigation on PV power output forecasting, using ANN and climatic data to join machine learning with monitored and modeled weather data, evaluating the Global Data Assimilation System's flux model as a substitute for on-site weather measurements. Their results showed this model effectively forecasted PV power production, achieving error rates below 10% when integrated with machine learning. Erduman [59] conducted an investigation to develop and implement an ANN-based model for predicting the output power of widely used PV panels. The results indicated that the model, which relies on fewer and more cost-effective inputs, can accurately determine the output of photovoltaic modules accurately. Wang et al. [60] compared simple photovoltaic power output estimating models across various PV technologies, finding the simple efficiency model overestimated power output by 10% for all except CdTe modules, while temperature-corrected and one-diode models provided reasonable accuracy.

Furthermore, Ayan and Toylan [61] analyzed the impact of climatic variables on the electricity generation of photovoltaic modules using the setup in Figure I.18. applying both ANNs and Multiple Linear Regression (MLR) with variables such as solar radiation, ambient and module temperature, humidity, wind speed, and wind chill. The study found that ANNs, particularly with the Levenberg–Marquardt algorithm, provided highly accurate power output predictions under varying environmental conditions.

Figure I.18: Free-standing photovoltaic module and measuring equipments used the study by Ayan and Toylan [61].

Park et al. [62] applied a recurrent neural network (RNN) to forecast PV electrical output, testing various network structures on hourly data from 9:00 to 17:00 between January 1 and July 9. Their results showed that a three-layer RNN performed better than a single-layer model, achieving RMSE coefficients of variation of 13.8% and 13.2%. Additionally, it was observed that the estimated and the experimentally collected values of power output exhibited similar fluctuations, mirroring each other’s patterns. Pamain et al. [63] implemented a non-linear autoregressive ANN model with environmental variables to estimate the electrical generation for two types of photovoltaic modules. Based on performance indices, they found that predicted power closely matched experimental data, with the Bayesian regularization algorithm performing best, yielding lower error and highest R^2.

Rodríguez et al. [64] created a model using deep learning and climatic variables to predict PV output confidence intervals 10 minutes ahead. Validated with actual data from Spanish weather stations, the model was found effective for predicting output intervals at different locations. Moreover, additional studies on PV power prediction can be referenced in [65-69]. Besides, for grid-connected photovoltaic power plants and performance prediction using ANN, more studies can be found in literature, such as in [70, 71]. Collectively, these studies highlight that ANN significantly outperforms traditional methods for accurately estimating PV power generation, which is essential for power management, performance optimization, and system stability.

I.6.2 Photovoltaic module temperature

The operating cell temperature is a critical parameter for photovoltaic module performance, significantly impacting the effectiveness of the solar-to-electricity conversion process [24, 25, 72], and therefore attracting considerable interest in the literature [73]. As a large portion of incident solar radiation dissipates as heat into the environment, module temperature is influenced by several environmental factors, including ambient temperature, wind speed, and solar radiation [27-30], To accurately predict module temperature, different heat transfer mechanisms—occurring on both sides of the module—are accounted for within an energy balance framework. Various predictive approaches have been explored in literature, including dynamic energy balance methods [74-76], data-driven modeling [77-81], numerical methods [82-84], and thermal modeling as well [85-88]. The subsequent section presents a review of recent studies employing these methods.

Ross [89], proposed a basic model for estimating the temperature of photovoltaic (PV) cells, introducing a straightforward linear equation for cell temperature (T_{cell}), in which the temperature difference $(T_{cell} - T_a)$ is linearly dependent on solar radiation G, with a proportionality constant k typically ranging from 0.02 to 0.04, later extended to higher values [90]. Another widely recognized method for estimating T_{cell} is the Nominal Operating Cell Temperature (NOCT) model by Stultz [91] where ambient temperature and irradiation are key inputs. Analogous models appear in literature [92-96], all commonly expressing $(T_{cell} - T_a)$ based on G. Servant [97] introduced a regression model that incorporates wind speed, supposing a linear relationship with climatic parameters and achieving close alignment with experimental data. Similarly, Lasnier [98] also used regression analysis to relate module temperature to ambient temperature and solar radiation. King [99] developed an empirical equation that considers ambient temperature, solar radiation, and wind speed, while in a later study, King et al. [100] introduced a model factoring in material properties, relating cell temperature with the module back-side temperature and offering empirical coefficients for calculation.

Additionally, TamizhMani et al. [101] tested five-inputs and three-inputs correlations for PV module temperature, where the simpler model includes basic environmental factors, while the more complex adds wind direction and humidity. Their findings suggested that solar radiation drives temperature increases, ambient air temperature sets the baseline, and wind speed mitigates the rise. Similar correlations by King et al. [102] and Kurtz [103] suggested another model equation for PV modules operating temperature, similar to the previous model, this one accounted for the above-mentioned variables, and considers the module encapsulation and mounting arrangement. Mondol et al. [94] proposed a module temperature estimation equation similar to Ross's model, relating it to ambient temperature and solar radiation. According to the study results, the suggested model resulted in less predictive error compared to the NOCT approach. Skoplaki et al. [104] introduced a semi-empirical formula for PV module temperature based on basic environmental variables, demonstrating a 3% error when natural convection was excluded, which decreased to 1.6% for solar radiation between 600 and 1100 W/m^2 and wind speeds of 1.2 to 4 m/s.

Koehl et al. [105] calculated PV module operating temperature with statistical and analytical models, recommending a Realistic Operating Module Temperature (ROMT) model, which showed a better correlation with experimental data than the NOCT method. Almaktar et al. [106] pointed out that a photovoltaic module's the temperature can be directly relate to ambient air temperature, introducing regression-based equations for calculating module temperature from environmental factors like solar radiation, ambient temperature, and wind speed, with results showing strong agreement with measured data and achieving low error rates across different module types. Muzathik [79] suggested a straightforward empirical equation to predict the operating temperature of the module, utilizing ambient air temperature, wind speed, and solar radiation as inputs, achieving about a 2.85% predictive error in terms of root mean squared error (RMSE).

Figure I.19: Photovoltaic module used the work of Muzathik [79].

Bailek et al. [77], proposed a predictive empirical equation for the temperature of the back-side of photovoltaic modules following the evaluation of several models. Their model used solar radiation and ambient temperature as inputs and achieved a coefficient of correlation at 0.955 with an error rate of 10%. Kaplanis et al. [107] conducted research on predicting the temperature and performance of photovoltaic modules, incorporating multiple parameters and performing a theoretical analysis. They introduced an empirical and compact model suitable for various mounting conditions, which showed superior performance and reduced error compared to similar models. Ceylan et al. [108] utilized an ANN model to estimate module efficiency, power output, and temperature, using an experimentally regulated solar radiation and ambient temperature during the training of the network. Coşkun et al. [109] applied ANNs to forecast the photovoltaic modules' surface temperature by factoring in ambient temperature, solar radiation, and wind speed, concluding after testing multiple training algorithms that ANNs could estimate module temperature with high accuracy. Additionally, Sohani and Sayyaadi [110] used genetic-based programming to develop a function form for module temperature estimation, including relative humidity as an input. They found that their function significantly outperformed existing models, such as the NOCT method.

Figure I.20: Photovoltaic module and measuring devices used in the study of Sohani and Sayyaadi [110].

Dong et al. [78] introduced a radial basis function neural network-assisted hybrid model to estimate the photovoltaic module temperature. Incorporating a refinement coefficient built up on the network yield, the considered approach enhanced the generalizability and significantly enhanced operating temperature forecasts. Similarly, Dong et al. [111] developed a radial basis function neural network-based hybrid model for module temperature prediction, optimized with an l_1 norm penalty, demonstrating accurate and promising predictive outcomes. Shiravi et al. [112] experimentally examined the impact of solar radiation concentration and wind speed on the performance of photovoltaic module. Via obtaining correlations for module temperature, efficiency, and power output, they highlighted the considerable influence of these parameters on module performance. Computational fluid dynamics (CFD) simulation has also been utilized in literature to study the power output of photovoltaic modules, temperature, performance, and installing configuration [113-115], and also PV/thermal systems [116, 117] is the approach of computational fluid dynamics (CFD) simulation. Lu and Zhao [115] used CFD simulation to investigate the impact of dust on module efficiency, noting that dust deposition, influenced by particle size, reduced performance. Wind effects on photovoltaic modules were examined in studies [118, 119], which found that wind velocity affects the distribution of pressure over the module surfaces and the process of cooling. Hove [120] pointed out that photovoltaic module temperature could be estimated through an energy balance, calculating heat loss based on experimental measurements. Mattei et al. [121] proposed a similar energy balance-based model to evaluate module temperature, incorporating an absorbance-transmittance coefficient $(\tau\alpha)$ of 0.81 and a heat transfer coefficient obtained from experiments, achieving a mean squared error (MSE) of $2.24°C$. Tiwari and Sodha [122, 123] also considered the thermal energy balance equation for cell temperature estimation in a hybrid PV-thermal system, finding close alignment with experimental data in system results.

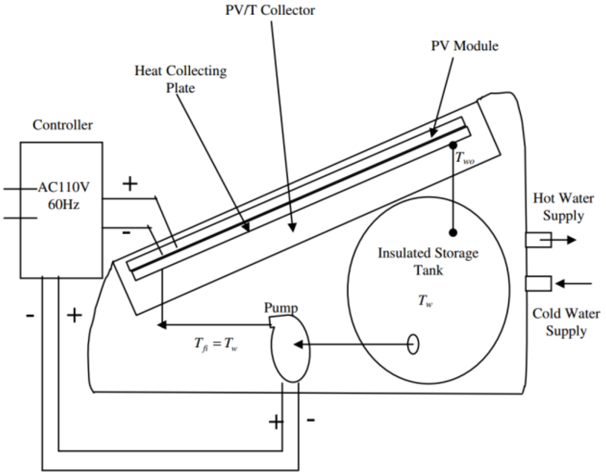

Figure I.21: Diagram of the PVT system in the studies of Tiwari and Sodha [122, 123].

Furthermore, Migliorini et al. [124] developed a thermo-electrical model that includes the underlying dynamics of the PV panels, where the operating temperature of the module estimated in the thermal model is used to predict power output. Their findings demonstrated that predictive error was notably reduced when accounting for the module’s dynamic properties. Akhsassi et al. [125] conducted experimental research involving thermal modeling for photovoltaic modules, presenting two models—one that includes wind effects and one that does not—. Results showed that their models performed better than comparable models in literature. Bevilacqua et al. [126] adopted an energy balance approach combined with the finite difference method to evaluate module temperature during spray cooling. This approach was designed to model the module’s internal thermal field and found that cooling reduced operating temperature of the module by 28.2%, with a potential power increase of up to 7.8%.

The above literature review indicates that many studies have focused on thermal-electrical modeling for photovoltaic modules [26, 127, 128]. However, it was observed that prior research primarily emphasized data-driven modeling for module temperature prediction. Additionally, most approaches concentrated on specific factors, like wind speed and direction [129-131], or on building-integrated PV modules [132-134]. In several studies, thermal radiation and free convection were often neglected, even though these factors become critical at high temperatures or low wind speeds.

Table I.3, provides a comprehensive listing of equations and models discussed within the above review of prior works. It highlights that correlations for operating temperature of photovoltaic modules can be categorized in various ways, including their mathematical basis of being explicit or implicit, the inputs used in the models, or the foundational principles they are based upon, such as the data-driven methods or the energy balance approach.

Table I.3: A list of equations for PV module temperature prediction.

#	Author(s) and year	Proposed model	Ref.
1	Ross (1976)	$T_{pv} = T_a + 0.03G$	[89]
2	Schott (1985)	$T_{pv} = T_a + 0.028G - 1$	[135]
3	Servant (1986)	$T_{pv} = T_a + 0.016G(1 + 0.030T_a)(1 - 0.085W_s)$	[97]
4	Lasnier (1990)	$T_{pv} = 1.14(T_a - 25) + 0.0175(G - 300) + 30.006$	[98]
5	King (1996)	$T_{pv} = T_a + \frac{G}{G_{ref}}(0.0712W_s^2 - 2.411W_s + 32.96)$	[99]
6	King et al. (1998)	$T_{pv} = T_a + \frac{G}{G_{ref}}(19.6\, e^{-0.223W_s} + 11.6)$	[100]
7	Hove (2000)	$T_{pv} = T_a + \left(\frac{\tau\alpha - \eta}{U_l}\right)G$	[120]
8	Davies at al. (2001)	$T_{pv} = T_a + \frac{G}{G_{ref}}\left(T_{NOCT} - T_{a,NOCT}\right)\left(1 - \frac{\eta}{\tau\alpha}\right)$	[136]
9	TamizhMani et al. (2003)	$T_{pv} = 0.943T_a + 0.028G - 1.528W_s + 4.3$	[101]
10	King et al. (2004) (I)	$T_{pv} = T_a + G(e^{-0.075W_s - 3.56})$	[102]
11	King et al. (2004) (II)	$T_{pv} = T_a + G(e^{-0.059W_s - 3.47})$	[102]
12	Mattei et al. (2006)	$T_{pv} = \frac{U_l T_a + G[(\tau\alpha) - \eta_{ref}(1 - \mu_T T_{ref})]}{U_l - \mu_T \eta_{ref} G}$	[121]
13	Mondol et al. (2007)	$T_{pv} = T_a + 0.031G$	[94]
14	Skoplaki et al. (2008) (I)	$T_{pv} = T_a + \left(\frac{0.25}{5.7 + 3.8W_s}\right)G$	[104]
15	Skoplaki et al. (2008) (II)	$T_{pv} = T_a + \left(\frac{0.32}{8.91 + 2.0W_s}\right)G$	[104]
16	Barno et al. (2012)	$T_{pv} = T_a + \frac{G}{50.0731 + 1.12349W_s} + 4.51228\log(1 + \frac{V}{V_{mpp}})$	[137]
17	Almaktar et al. (2013) (I)	$T_{pv} = 1.411T_a - 6.414$	[106]
18	Almaktar et al. (2013) (II)	$T_{pv} = 26.97 + 0.77T_a + 0.023G - 0.206RH - 0.137W_s \pm 2.656$	[106]
19	Almaktar et al. (2013) (III)	$T_{pv} = 20.72 + 0.88T_a + 0.022G - 0.14RH - 0.937Ws \pm 1$	[106]
20	Muzathik (2014)	$T_{pv} = 0.943T_a + 0.0195G - 1.528W_s + 0.3529$	[79]
21	Akhsassi et al. (2018) (I)	$T_{pv} = \frac{U_l T_a + G\left[(\tau\alpha)\eta_{STC}(1 - \mu_{Pmp}T_{ref})\left(1 + \gamma_{Pmp}\log\left(\frac{G}{G_{ref}}\right)\right)\right]}{U_l + \eta_{STC}\mu_{Pmp}\left(1 + \gamma_{Pmp}\log\left(\frac{G}{G_{ref}}\right)\right)}$	[125]

22	Akhsassi et al. (2018) (II)	$\mathrm{T_{pv}} = \mathrm{T_{ref}} + 0.0126(\mathrm{G} - 200) + 1.03(\mathrm{T_a} - \mathrm{T_{a,NOCT}})$	[125]
23	Bailek et al. (2020)	$\mathrm{T_{pv}} = 0.968\mathrm{T_a} + 0.02\mathrm{G} - 1.007$	[77]
24	Sohani and Sayyaadi (2020)	$\mathrm{T_{pv}} = \frac{1}{3}\left[aT_a + b\left(\frac{G}{G_{ref}}\right)^c + dRH^e - fW_s + g\right] - 273.15$	[110]

I.7 Motivation

The above review, introduction, and current situation of energy consumption, as well as the forecasting of future energy demand and population growth suggest that clean and renewable energy sources must replace fossil fuels that are being used currently.

Among several renewable energy sources, solar photovoltaic conversion, which affords direct clean electricity, is one of the most promising technology, thanks to several advantages over other renewable energies. However, the efficiency and performance of photovoltaic modules are highly sensitive to environmental conditions, particularly temperature, which significantly impacts their power output.

Accurate prediction and optimization of PV performance under various operational conditions is crucial for maximizing energy production and improving system reliability. This thesis is motivated by the need to develop robust models that integrate data-driven approaches, machine learning, and numerical simulations to enhance the understanding of photovoltaic module behavior, specifically in relation to temperature effects and power output. By combining thermal modeling and advanced computational techniques, this research aims to contribute to the broader effort of accelerating the transition to sustainable energy systems, ensuring better energy management and more effective deployment of solar technologies.

I.8 Conclusion

This chapter reported an introduction to the topic of solar photovoltaic conversion, beginning with an overview of the current global energy landscape, focusing on energy consumption patterns and the heavy reliance on fossil fuels, and their relation to global climatic change on the planet. Additionally, this chapter highlighted the importance of the shift towards renewable energy, and role of solar energy in general, and the solar photovoltaic energy in particular. Moreover, the chapter presented the fundamentals of solar radiation and the principles of photovoltaic conversion, explaining how solar energy is harnessed and converted into electrical power. Finally, a detailed literature review was conducted, examining previous research and technological advancements relevant to this study’s focus, laying the foundation for the development of predictive models and optimization of PV systems in later chapters.

CHAPTER II : MATERIALS AND METHODS

II.1 Introduction

In CHAPTER II, first, the experimental setup and data acquisition system are presented, thereafter, uncertainties associated with each device in the system, as well as error and performance evaluation criterions are introduced. Additionally, the different techniques used in data preprocessing are also presented in details in this chapter. Moreover, the proposed data-driven approaches to estimate, predict and understand the relations are presented, where a solid understanding of the underlaying structure of the data and parameters governing the performance of photovoltaic modules is established.

II.2 Experimental setup

In this study, one of the objectives is to build models that estimates the photovoltaic modules' the power output of and their temperature accurately. Thus, experimental dataset is required for training and tasting stages of data-driven models, and for the numerical simulations as well. In pursuit of this goal, two identical polycrystalline silicon PV modules of JONSOL JSP-36 type are being utilized (Figure II.1). The electrical and mechanical characteristics of these modules are shown in Table II.1 and Table A.1, respectively. The installation of the modules was at the University of El Oued, south-east of Algeria (33°27′20″N 7°11′0″E and 76m altitude), where warm climatic conditions may be expected even in winter [138]. The on-site climatic parameters, namely, ambient temperature (T_a), solar radiation (G), wind speed (W_s), wind direction (W_d), humidity (RH) and module temperature (T_{pv}), as well as the power output of both modules (P_{pv}) were collected for several periods over the past few years.

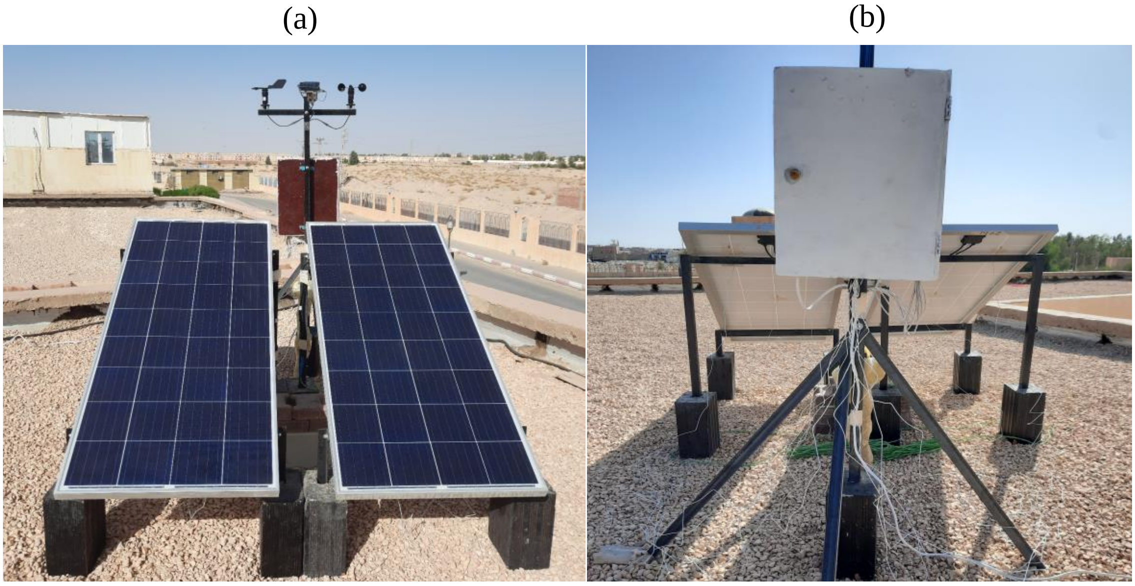

Figure II.1: (a) front view and (b) back view of the utilized photovoltaic modules [25].

Table II.1: Photovoltaic module electrical characteristics [25].

Characteristic	Value
Open-Circuit Voltage ($\mathrm{V_{oc}}$)	22.70 V
Optimum Operating Voltage ($\mathrm{V_{mp}}$)	18.60 V
Short-Circuit Current ($\mathrm{I_{sc}}$)	9.08 A
Optimum Operating Current ($\mathrm{I_{mp}}$)	8.61 A
Maximum Power at STC ($\mathrm{P_{max}}$)	160 W
Cell Efficiency	18.3%
Module Efficiency	16.2%
Maximum system Voltage	1000 V DC
Operating temperature	-40C° to +85 C°
Power tolerance	0/ +3 %

II.2.1 Error evaluation

To evaluate the results machine learning algorithms, simulations models, the performance of regression models and prediction accuracy, several statistical indicators are used. In additions to the basic Mean Absolute Error (MAE), these metrics include Mean Squared Error (MSE), Root Mean Squared Error (RMSE), and the coefficient of determination (R^2), where R^2 helps determine the extent of data variability explained by the model [139]. Other metrics quantify prediction errors, for instance, MAE provides an average error metric but assigns equal importance to all errors, which may not be ideal [34], Thus, MSE and RMSE are also used to address this limitation. MSE quantifies the deviation between estimates and true values, as it reflects the expected squared Euclidean distance between the estimated and actual values [140]. RMSE, a commonly used metric, measures the square root of these average squared deviations, thereby capturing the mean difference between observed and predicted values [141]. Furthermore, this study uses both adjusted R^2 and predicted R^2. The statistical indicators applied here are expressed mathematically as follows:

$$R^2 = 1 - \frac{\sum_{i=1}^{n}\left(Y_{i,meas} - Y_{i,pred}\right)}{\sum_{i=1}^{n}\left(Y_{i,meas} - \overline{Y_{\imath,pred}}\right)} \tag{II.1}$$

$$MAE = \frac{1}{n}\sum_{i=1}^{n}\left|Y_{i,meas} - Y_{i,pred}\right| \tag{II.2}$$

$$MSE = \frac{1}{n}\sum_{i=1}^{n}\left(Y_{i,meas} - Y_{i,pred}\right)^2 \tag{II.3}$$

$$RMSE = \sqrt{\frac{1}{n}\sum_{i=1}^{n}\left(Y_{i,meas} - Y_{i,pred}\right)^2} \tag{II.4}$$

$$MAPE = \frac{1}{n}\sum_{i=1}^{n}\left|\frac{Y_{i,meas} - Y_{i,pred}}{Y_{i,meas}}\right| \tag{II.5}$$

where $Y_{i,meas}$ and $Y_{i,pred}$ represent the experimental and estimated target variables, respectively; n is the number of instances, and $\overline{Y_{\imath,pred}}$ denotes the mean value of the estimated target.

II.2.2 Uncertainty analysis

Each experimental measurement involves some margin of uncertainty, despite instrument accuracy. This uncertainty can arise from factors such as instrument sensitivity, calibration inconsistencies, and environmental effects. A common approach to assess such discrepancy is to repeat trials as extensively as possible, using the mean value of the variable measurements as the best estimate of that variable [142].

Although this technique was not directly applied in present work, however the mean of all parameters' measurements over a specified time interval was considered to decrease potential experimental errors. Additionally, every instrument was calibrated before taking measurements. Calibration revealed good levels of accuracy across instruments, with solar radiation measurement errors within only $\pm 3\%$, using a SolData Instruments hand pyranometer (type 105hp). The humidity and temperature sensors had maximum errors of 5% and $0.5°C$, respectively, as specified by the provider, with resolutions of 0.1% and $0.1°C$. Wind speed and direction sensors, according to the supplier, have a measuring accuracy of $\pm 3\%$ and a response time of under 1 second, with an accepted range of $0\text{–}30\,m/s$ for wind speed. K-type thermocouples used for temperature measurements showed an accuracy of $\pm 0.75\%\,T$, a time of thermal response below 0.5 seconds, and a measurement range from -40 to $400°C$.

II.3 Data description and preprocessing

The datasets in the studies of current work were originally recorded with a three-second time interval between each two consecutive measurements, which resulted in 28800 instances per day for each variable. When data-driven modeling is desired, the dedicated dataset was split to two main separate subsets, the first one includes data that was used for training, validation or cross-validation, and testing, with ratios ranging from 70 to 80%, 10 to 15%, and 10 to 15%, respectively. While the second dataset is for prediction purposes. Schematic presentation of the datasets decomposition (during module power output prediction) is shown in Figure II.2. It should be pointed out that the purpose of tests performed for the first subset of data is only for model tuning and training algorithm selection, whereas, after the model validation and testing, the second subset of data is used for the forecasting of desired variable, which is either the module's power output or its temperature.

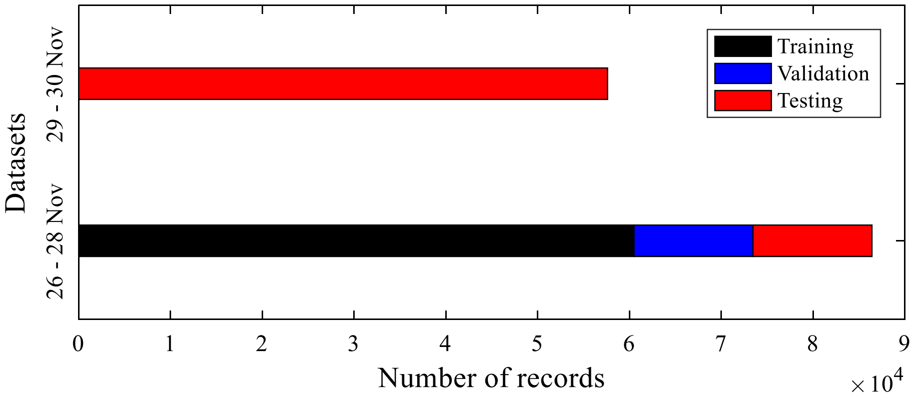

Figure II.2: Division of datasets into train, validation, and test subsets [25].

To develop an effective, reliable, and accurate model, historical measured data must first be validated to prevent unreliable data from slowing the learning rate or causing the model to miss-learn, which could increase error likelihood and lead to inaccurate forecasts. Validation ensures that the training and testing data are reliable and well-suited to the problem at hand. Additionally, by applying physics-based expertise, new variables can be created from the original ones, ultimately adding value to the data and enhancing model performance. However, caution is required, as poorly chosen features can increase model complexity. Further preprocessing is necessary to select the features most relevant to the target variable, resulting in a subset of data used for implementing the learning technique. This preprocessing, often referred to as feature engineering and feature selection, is applied in this study and discussed in the following sections.

II.3.1 Feature engineering

To improve model performance, feature engineering aims to formulate useful features that enhance target prediction accuracy. This process involves various techniques, and for this study, imputation has been applied to address missing data. Specifically, absent values in the dataset have been substituted with their corresponding mean values, aligning with the principle of normal distribution. Similarly, outliers and abnormal values were handled using the same approach as well. Whereas, the negative quantities were substituted by zeros. Additionally, to decrease the noise in the raw data acquired from experiments and measurements of weather conditions and PV module output, a 20-point average was applied, yielding a refined data that averages the data over one-minute intervals.

Prior to training, validation, and testing phases of the ANN model, a final step involves normalizing the measured data to a range of [0, 1]. This normalization prevents neuron saturation and eliminates the influence of attribute dimensions, achieved by applying Eq. (II.6):

$$\bar{x} = \frac{x - x_{min}}{x_{max} - x_{min}} \tag{II.6}$$

In this equation $\bar{x}$ denotes the standardized variable, *x* represents the primer variable in the dataset, while x_{max} and x_{min} denote the maximum and minimum values of the corresponding variable in the dataset. Thus $\bar{x}$ equals 0 when *x* is at its minimum and 1 when it is at its maximum.

Similar approach that can be taken when implementing machine learning algorithms, is normalizing the dataset, which is usually essential for many machine learning algorithms. The scaling is achieved using Eq. (II.7):

$$\bar{x}_{i,j} = \frac{x_{i,j} - \mu_j}{\sigma_j} \tag{II.7}$$

where $\bar{x}$ denotes the normalized or scaled input feature, $x_{i,j}$ represents the j^{th} feature in i^{th} sample from the original dataset, and μ_j and σ_j represent the mean and the standard deviation for the j^{th} feature, respectively in data. This process centers all feature $(\bar{x})$ around zero and scales them by their standard deviation, optimizing the data for machine learning algorithms while preserving the underlying information.

II.3.2 Feature selection

II.3.2.1 Correlation coefficient

In machine learning, input variables are referred to as features, and in this work, each column in the dataset represents a feature. Due to the fact that a model may identify non-essential patterns or incorporate noise into its learning, which can increase computational time, reduce predictive accuracy, and complicate the model [143]. it's crucial to ensure only the most relevant and useful features are included for optimal training. Here, several weather-related features (solar radiation G, ambient temperature T_a, wind speed W_s, wind direction W_d, and relative humidity RH) associated with photovoltaic module temperature power generation were logged. To assess the significance and relevance of each feature to the output variable, a correlation analysis is conducted using Principal Component Analysis (PCA) or Pearson correlation coefficient. For Pearson correlation coefficient, the chosen thresholds for interpreting R values are as follows: for $R \geq 0.9$ indicates high correlation; $0.9 \geq R \geq 0.5$ suggests a fair or reasonable correlation; whereas $0.5 \geq R \geq 0.3$ denotes weak correlation; and when $R \leq 0.3$, it indicates that almost there is no correlation [144].

II.3.2.2 Principal Component Analysis

To analyze the dataset's structure, a Principal Component Analysis (PCA) was conducted. PCA serves to identify underlying patterns and simplify the dataset by reducing dimensionality. This technique helps streamline the model by removing less relevant features, retaining only those that provide significant information. By transforming the original features into a set of uncorrelated components, PCA emphasizes the most impactful variations within the data, which enhances computational efficiency and potentially improves model accuracy. The results of PCA inform the selection of key features, ensuring the model uses only the most informative attributes while minimizing redundancy [145].

II.4 Machine learning algorithms

Modeling involves establishing equations and mathematical expressions to describe and explain the comportment of a specific dependent variable, relaying on information from other independent input variables, often called explanatory variables or predictors [146]. This approach is widely used to represent and understand natural phenomena, with models reflecting our insights.

These models typically contain coefficients, and the process of determining them is called regression [147], which helps estimate relationships between outputs and inputs. Regression can be classified in many ways—linear, non-linear, simple, multiple, parametric, and non-parametric—and can be performed using various approaches. One common method is Least Squares, which aims to minimize the sum of squared residuals. Recently, advanced methods like regularization have emerged, and machine learning (ML) algorithms are increasingly applied to regression and prediction. In this study, several ML algorithms were employed, assessed, and evaluated for predicting PV module temperature and power output. These include multiple-linear regression, non-linear regression, Ridge regression, LASSO, Elastic Net, decision trees, random forest, gradient boosting, support vector regression, artificial neural networks, and Gaussian process regression. These algorithms fall into categories such as linear, non-linear, tree-based, kernel-based, probabilistic, and artificial neural networks. The following provides a brief overview of each ML algorithm used in this study.

II.4.1 Multiple-linear Regression

Multiple-linear regression (MLR) is a widely used technique for deriving predictive models and estimating equations, often applied to predict photovoltaic module temperature. In this context, MLR serves as a statistical tool for constructing, expressing, and evaluating the relationships between multiple input variables and the module temperature as the output. This approach is straightforward, yet highly effective for analyzing the influence of each input to the output variable, where each feature is assigned a coefficient (or weight) that represents its impact on the output (power output or module temperature in this work). The general form of an MLR equation is as follows

$$\hat{y} = b_0 + b_1 x_1 + b_2 x_2 + \cdots + b_p x_p + \epsilon \tag{II.8}$$

where $\hat{y}$ denotes the target output, x_i denotes the i^{th} explanatory variable, whereas $b_0, b_1, b_2, \dots, b_p$ are the coefficients for the regression, and ε signifies the error term, that is deviation of estimated values from actual values.

II.4.2 Non-Linear regression

Simple linear regression and multiple-linear regression (MLR) are accessible and interpretable tools for mathematical modeling. However, much of natural phenomena behave in nonlinear ways [147], making nonlinear analysis frequently essential. Nonlinear models can take diverse forms—such as exponential, quadratic, or logarithmic—that capture more complex relationships. While MLR is commonly used to estimate the photovoltaic (PV) power output and operating temperature of the module due to its simplicity, it risks overfitting and may lack sufficient flexibility. Nonlinear models, in contrast, can improve prediction accuracy and adaptability, especially when accounting for the stochastic nature of wind speed and solar radiation, which may exhibit ergodic characteristics. Additionally, ambient temperature variations, especially in arid regions, can produce corresponding fluctuations in the operating temperature of photovoltaic module and their power output.

In this study, with ambient temperature (T_a), solar radiation (G), wind speed (W_s), and relative humidity (RH) as inputs, and the operating temperature of the module (T_{pv}) as the target, the regression task for both MLR and nonlinear models is formulated as follows:

$$Y = BX \tag{II.9}$$

where X represents the matrix of measurements, Y is the response variable, and B is the vector of model coefficients. The Least Squares method is applied to estimate these coefficients for both the MLR and nonlinear models.

II.4.3 Ridge regression

The coefficients of input variables can be influenced by the inclusion or exclusion of other features in the model, raising significant concerns when correlations among features exist. Such correlations can lead to substantial errors and unexpected predictions [148]. In this case, to address this issue, redundant features may be removed, or regularization techniques like Ridge regression, also known as Tikhonov regularization, can be employed [149], This method introduces an l_2 penalty term to the sum of squares in a regression framework. Essentially, the goal is to minimize the sum of squares to achieve a good fit while simultaneously preventing the coefficient vector from becoming excessively large. Mathematically, Ridge regression can be formulated as minimizing the following objective function:

$$\sum_{i=1}^{n} \|Y - BX\|_2 + \alpha\|B\|_2 \tag{II.10}$$

where α is a tuning parameter to be set. One method for determining the optimal α value involves adjusting the value of α and plotting the predicted coefficients versus α values, creating what is referred to as the Ridge trace. The optimal αα is identified as the point at which the curve exhibits a “knee” [148]. Alternatively, α can be selected through cross-validation, where the value that yields the best predictions on new datasets or results in the lowest error is chosen. This latter approach is the one adopted in this study.

II.4.4 Kernel Ridge Regression (KRR)

An advanced variant of the Ridge regression algorithm is the Kernel Ridge Regression (KRR), which represents a specific case of Support Vector Regression [150]. This approach leverages a kernel function to model nonlinear relations between the inputs and the output target, allowing it to effectively account for complicated structures and patterns in the data. By utilizing the kernel function, KRR defines the inner product in a transformed higher-dimensional space [151]. The mathematical formulation of the objective function to be minimized in the KRR problem can be expressed as follows: [152]:

$$\sum_{i=1}^{n} \left\| Y - BK(x_i, x_j) \right\|_2 + \alpha \|B\|_2$$

where K is the kernel matrix (a matrix of kernel values between pairs of data points). In this study, a second-order polynomial function serves as the kernel function, utilizing the optimal value of the regularization parameter α to predict the module temperature based on ambient conditions.

II.4.5 LASSO

The Least Absolute Shrinkage and Selection Operator (LASSO), introduced by Tibshirani, is another technique used for regularized regression [153], and is particularly useful when dealing with a large number of predictors. The LASSO algorithm employs an l_1 penalization that helps to balance model complexity and interpretability, effectively preventing overfitting [154]. This method can also yield a particular subset of features from the dataset, as it reduces some coefficients in the model toward zero, thereby eliminating certain variables in the model. LASSO is known to be robust to outliers, and also known for its ability to create sparse models. The LASSO algorithm achieves this by trading the l_2 penalty term used in Ridge regression with an l_1 penalty term, leading to the following objective function that needs to be minimized:

$$\sum_{i=1}^{n} \|Y - BX\|_2 + \lambda\|B\|_1 \tag{II.11}$$

Here, λ is also a tuning parameter. The selection of λ can also be performed visually, similar to the approach used in Ridge regression, by utilizing what is known as the LASSO path. Alternatively, validation or cross-validation for performance evaluation can be employed, wherein the model is trained on a training dataset and subsequently evaluated against a test holdout dataset. This testing process involves random and repeated selection of the holdout data in the case of cross-validation, across a spectrum of λ values.

II.4.6 Elastic Net

Elastic Net is a regularization technique introduced by Zou and Hastie [155] that enhances the capabilities of the previously discussed regression methods by integrating the strengths of both Ridge and LASSO. This approach not only offers a sparse representation but also effectively groups correlated predictors, allowing them to be included or excluded from the model collectively. Elastic Net proves particularly advantageous when the number of features greatly exceeds the number of observations. Mathematically, Elastic Net aims to find the value of B that minimizes the following objective function [148]:

$$\sum_{i=1}^{n} \|Y - BX\|_2 + \lambda\|B\|_1 + \alpha\|B\|_2 \tag{II.12}$$

Again, both values of the tuning parameters (λ and α) are determined through cross-validation, that is the approach used in this study.

II.4.7 Decision Tree Regression

Decision trees are structured data representations consisting of various branches and nodes, where internal nodes have outgoing edges and terminal nodes are referred to as leaves [156]. These algorithms serve both regression and classification tasks, making estimations and predictions by recursively dividing a dataset and applying simple models to each segment [157]. In this work, the emphasis is on regression type decision trees, which predict continuous target variables. The process begins with a complete dataset at the root node, where an algorithm generates the decision tree by selecting a specific feature and threshold at each decision node to divide the dataset into two subsets based on a defined criterion (MSE in this case). The splitting process continues iteratively for all subset, forming a tree-like structure. If the regression tree is established, predictions for input values are computed as the average or weighted average of the target values from the training data within that specific leaf node. Regression decision trees offer several advantages, including flexibility, simplicity, and the ability to handle missing data. However, they also face challenges such as sensitivity to data variations and the risk of overfitting [156]. In this work, a regression model akin to the one depicted in Figure II.3 is utilized to predict T_{pv}. The model, featuring 51 nodes, was selected following a cross-validation and tuning process, where the maximum number of splits was capped at 25, yielding the lowest MSE during the training phase.

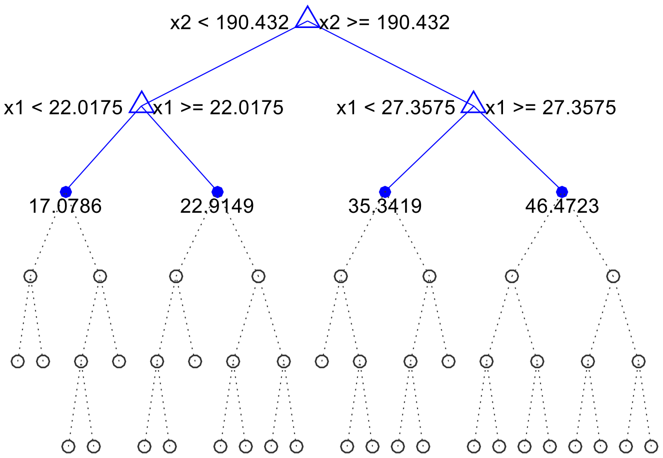

Figure II.3: Schematic presentation of decision tree model in this work [145].

II.4.8 Random Forest Regression

Random forest is an ensemble learning technique developed by Breiman [158], which combines multiple decision trees to create a more accurate and robust predictive model. In this approach, the predictions from individual trees are averaged for regression tasks or voted upon for classification, resulting in a final ensemble prediction. The algorithm works by drawing random samples from the original dataset through a method known as bootstrapping, subsequently constructing unpruned regression trees for each sample. During this process, rather than evaluating all input available to determine the optimal split at a given node, a random subset of inputs is selected. The feature that yields the optimal results is then chosen, introducing randomness and diversity into the tree ensemble. After constructing all trees, each tree generates predictions for the new dataset; in the case of regression, the final prediction is obtained by averaging the outputs from all trees [159].

In this study, the random forest algorithm is employed to estimate the operating temperature of a photovoltaic module (T_{pv}) based on various ambient parameters. A cross-validation process is conducted, utilizing a random selection of 80% of the training dataset to train and fine-tune the model. After conducting 100 trials, it was determined that a model comprising 98 trees yielded the best performance. The random number of features for each tree, which is selected to optimize the dataset split at each node, was set to two features. This model not only produced the lowest mean squared error (MSE) among the tested configurations but was also deemed optimal for future predictions of module temperature.

II.4.9 Gradient Boosting Regression

The Gradient Boosting regression algorithm is another ensemble learning method that builds robust models by adding weak learners sequentially, usually in the form of decision trees [160]. The process begins with a weak learner, known as the base model, which is normally a decision tree in regression problems. Initially, this base model may produce inaccurate predictions. To improve these predictions, residuals (or pseudo-residuals, given the iterative nature) are computed based on the loss function's gradient, often the least squares function. To predict these residuals using the input features, a regression tree is then generated. The model's predictions are subsequently updated by incorporating this new weak learner into the ensemble, where the predictions from the new tree are scaled by a learning rate to penalize and regularize performance. Thus, the final prediction of the ensemble model is achieved by summing the predictions of all weak learners, each weighted by the learning rate. This iterative process progressively minimizes the residuals at each step, significantly improving the overall model accuracy. Further details and mathematical formulations of the algorithm are available in [160, 161]. In this study, a least square boosting model is employed to estimate the operating temperature of a photovoltaic module (T_{pv}) using ambient conditions as inputs. Specifically, this model utilizes as weak learners, 600 regression trees, which was identified as the optimal configuration after conducting cross-validation.

II.4.10 Support Vector Regression (SVR)

Introduced as an innovative regression method by Drucker et al. [162], and founded on the concepts developed by Cortes and Vapnik [163], Support Vector Regression Machines (SVR), focuses on identifying an optimum function that characterizes the relation between the input x and the output variable y, all with achieving a balance between the accuracy and simplicity of the model. The algorithm operates by transforming the input features into a higher-dimensional space via a kernel function [164], which allows for linear separation and facilitates the modeling of complex relationships. Mathematically, the goal of the SVR algorithm is to minimize the following optimization problem [165]:

$$\min_{w,b,\xi,\xi^*} \frac{1}{2}\|w^2\| + C\sum_{i=1}^{n}(\xi_i + \xi_i^*)$$

Subject to:

$$Y_i - w^T\emptyset(x_i) - b \leq \epsilon + \xi_i^*$$

$$w^T\emptyset(x_i) + b - Y_i \leq \epsilon + \xi_i$$

$$\xi_i, \xi_i^* \geq 0, i = 1, \dots n$$

In this formulation of the objective function, the first term serves as a regularization component, while the second term quantifies the discrepancy between the estimated values and the real output values (Y_i). The coefficient C plays a crucial role in balancing the minimization of error against the maximization of margins, with the variables ξ_i^* and ξ_i representing the inferior and superior limits on the training error, respectively. By solving this optimization problem, the SVR algorithm determines an optimum weights vector w, bias b, and the bound parameters, all of which define the hyperplane that best fits the dataset. In this study, the SVR algorithm is employed to estimate the operating temperature of the photovoltaic module, utilizing the training algorithm of Sequential Minimal Optimization (SMO) [166]. The established model undergoes cross-validation using a training subset of the data and includes a linear kernel function, which yielded the most favorable results.

II.4.11 Artificial neural networks

Artificial neural networks (ANNs) are a form of artificial intelligence designed to emulate natural neural systems. They consist of numerous interrelated processing nodes, known as neurons, which function like microprocessors [167], This structure enables ANNs to automatically adjust and learn from data. They excel at identifying patterns and relationships within datasets, making them well-suited for various forecasting and prediction tasks, particularly in non-linear contexts [168], In an ANN, each neuron receives a signal of input, transforms it by applying the weight and bias terms, and then uses an activation function before passing the processed signal to the subsequent neuron. This process continues as the ANN receives inputs $(x_1, x_2 \dots x_n)$ adjusts the weights and biases through a learning mechanism, and ultimately generates the output y. Mathematically, the output of a neuron can be represented as follows:

$$Y_i = \phi\left(\sum_{i=1}^{n} w_i x_i - b\right) \tag{II.13}$$

where Y_i represents the output, x_i denotes the input variable, w_i designates the weight, and b is the bias term, while ϕ denotes the activation function, which is employed to constrain the output of the neurons to a specific range, typically between 0 and 1 (or -1 to 1). Among the various activation functions available, Rectified Linear Unit (ReLU) and the sigmoid function are among the most commonly employed ones. In this study, the sigmoid activation function is chosen due to its superior performance in comparative tests with other activation functions. Its characteristics align well with the problem at hand, and it is well-suited to the nature of the dataset being analyzed, making it a popular choice in contemporary applications.

During the transfer of information from the input layer to the output layer through one or more hidden layers, the parameters known as weights are adjusted to reflect the strength of connections among the nodes (neurons) across different layers. This adjustment process enables the artificial neural network (ANN) model to learn and align its output with a desired target output. This iterative process, referred to as the training algorithm, continues until a predetermined criterion is met. Once the model is trained, it can generate predictions for new, unseen data that was not included in the training phase. The prediction of a neural network is usually evaluated using some error indicator, for instance, the Mean Squared Error (MSE) or the Mean Absolute Error (MAE).

In this study, a Feed Forward Neural Network (FFNN) is established to estimate the operating temperature of photovoltaic (PV) modules. This model is a multilayer perceptron ANN that aligns the input data to the corresponding output. Several FFNN configurations were employed and assessed, and through a hyperparameter tuning process, it was determined that a model featuring three hidden layers with 4, 3, and 2 neurons, respectively, provided optimal robustness and superior performance in terms of accuracy and computational efficiency, as illustrated in Figure II.4, To enhance prediction accuracy, various training algorithms were tested and compared to identify the most effective approach for this prediction task, whereas the sigmoid activation function was employed to present the nonlinearity into the model.

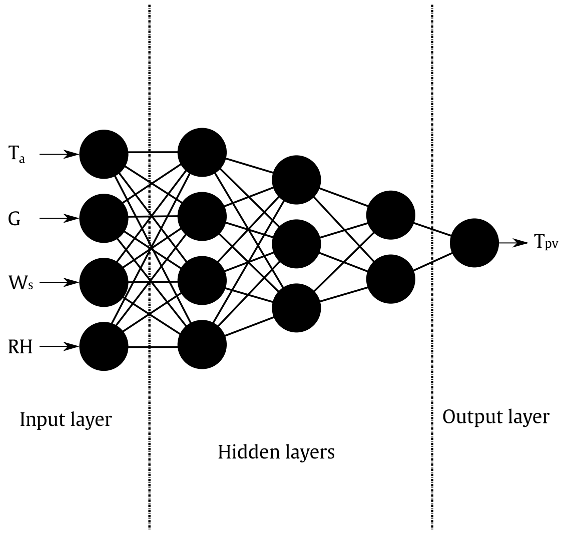

Figure II.4: Schematic illustration of the ANN model [145].

II.4.12 Gaussian Process Regression

Gaussian Process Regression (GPR) is a non-parametric probabilistic algorithm that, in contrast to traditional regression methods which yield point estimates for predictions, offers a distribution over possible functions that can describe the correlation between the output and input variables. This makes GPR particularly valuable for modeling complicated data, involving non-linear relations [169].

The fundamental hypothesis underlying Gaussian processes is that the function values at a set of inputs $M > 0$ are jointly Gaussian, characterized by a mean function $\mu = m(x_1), \dots, m(x_M)$ and a covariance (kernel) function $\sum_{i,j} = K(x_i, x_j)$, where m is the mean function and K is a positive definite kernel [170]. In essence, this means that if x_i and x_j are deemed similar according to the kernel, the function's outputs at those points are also likely to be similar.

In practice, GPR establishes a prior distribution over functions. When the training data consisting of inputs $X = \{x_1, x_2 \dots x_n\}$ and their corresponding output values $y = \{y_1, y_2 \dots y_n\}$ are available, this prior can be updated to form a posterior distribution over functions. The joint distribution of the observed data and new data points can then be calculated, allowing the model to make predictions that incorporate both the uncertainty in the data and the inherent variability of the underlying function:

$$\begin{pmatrix} y \\ y_* \end{pmatrix} \sim \mathcal{N}\left(0, \begin{bmatrix} K & K_* \\ K_*^T & K_{**} \end{bmatrix}\right)$$

Here, K represents the covariance matrix of training data points, K_* signifying the covariance matrix between training and new data points with K_*^T denoting its transpose, and K_{**} is the covariance matrix of new data points. Then, for testing dataset of input X_* the predictive mean and covariance are calculated:

$$y_*|x_*, X, y \sim \mathcal{N}(K_*^T K^{-1} y, K_{**} - K_*^T K^{-1} K_*)$$

The y_* values represent the predicted outputs corresponding to new inputs x_*, based on the observed values X and y, The expressions in parentheses indicate the predictive, mean and covariance matrix, respectively. It is important to highlight that selecting the appropriate kernel function and fine-tuning its hyperparameters are crucial for enhancing the quality of predictions and defining the characteristics of the inferred function. In this study, the Gaussian Process Regression (GPR) algorithm is employed to forecast the temperature of photovoltaic (PV) modules, utilizing a Squared Exponential kernel (also known as the radial basis function). This choice allows the model to effectively capture intricate relationships between the input features and the target variable, enabling more accurate predictions in estimating the operating temperature of the photovoltaic module.

II.5 Conclusion

In CHAPTER II, the experimental setup for data collection is presented in detail, outlining the photovoltaic (PV) system configurations, instrumentation, monitoring equipments. This chapter also explains how key parameters such as electrical output and environmental conditions were measured, providing context for the collected data. It also includes error evaluation metrics and uncertainty analysis to assess the accuracy and reliability of the data. Metrics such as Mean Absolute Error (MAE) and Root Mean Squared Error (RMSE), while the uncertainty analysis highlights potential sources of measurement errors. Following this, the data processing techniques are discussed, including data cleaning and handling missing values, to prepare the dataset for analysis. Additionally, a detailed overview of the machine learning algorithms used in this study, such as linear regression, decision trees, random forests, and neural networks, is provided. Each algorithm’s purpose, strengths, and limitations are explained, alongside the reasoning behind their selection for predicting PV performance under varying conditions. This chapter establishes the foundation for the modeling and analysis conducted in the research.

CHAPTER III : MODELING TECHNIQUES

III.1 Introduction

In addition to the data-driven modeling and prediction of photovoltaic (PV) module power output and temperature, numerical simulations using Ansys Fluent's Computational Fluid Dynamics (CFD) were applied to study the effect of ambient parameters on PV performance. These simulations explore how factors like wind speed, ambient temperature, and solar irradiance impact the thermal behavior and power output of PV modules. By modeling fluid flow and heat transfer around the modules, the CFD analysis provides detailed insights into cooling and heating processes, essential for maintaining high module efficiency. To further enhance the understanding of heat transfer within PV modules, thermal modeling was also proposed. This approach uses heat transfer principles, including conduction, convection, and radiation, to predict the temperature of the modules under different operating conditions. By incorporating fluid dynamics and thermal properties, the model accurately forecasts how the module's temperature changes with varying environmental influences. CFD simulations and thermal modeling offers a more comprehensive view of PV performance, complementing the data-driven models. Combined, these methods enable better optimization of PV systems, improving temperature management, enhancing efficiency, and extending the lifespan of the modules. Those approaches lead to more reliable predictions of power output and performance under real-world conditions.

III.2 Numerical simulation

III.2.1 Physical model

In this study, the focus is on investigating the three-dimensional fluid flow and heat transfer around a free-standing photovoltaic (PV) module. The primary goal is to model heat conduction across the various layers of the PV module and to account for heat exchanges through convection and radiation between the outer surfaces of module and the surrounding air. This modeling effort aims to accurately predict the average temperature, efficiency, and power output of the PV module. To achieve this, a physical model analogous to the one schemed in Figure III.1 is utilized for the numerical simulations. The surrounding fluid domain (air) is defined by dimensions of length L, width W, and height H, with the photovoltaic module positioned at the third of the total length L. Furthermore, the air domain is assumed to be sufficiently wide so that the boundaries do not influence the simulation results. The photovoltaic module under consideration is composed of five distinct layers arranged from top to bottom: Glass, EVA, PV Cells, EVA, and a back sheet made of Tedlar Polyester (TPT). The material and thermophysical properties of each layer of the module, as well as those of the surrounding air, are summarized in Table III.1.

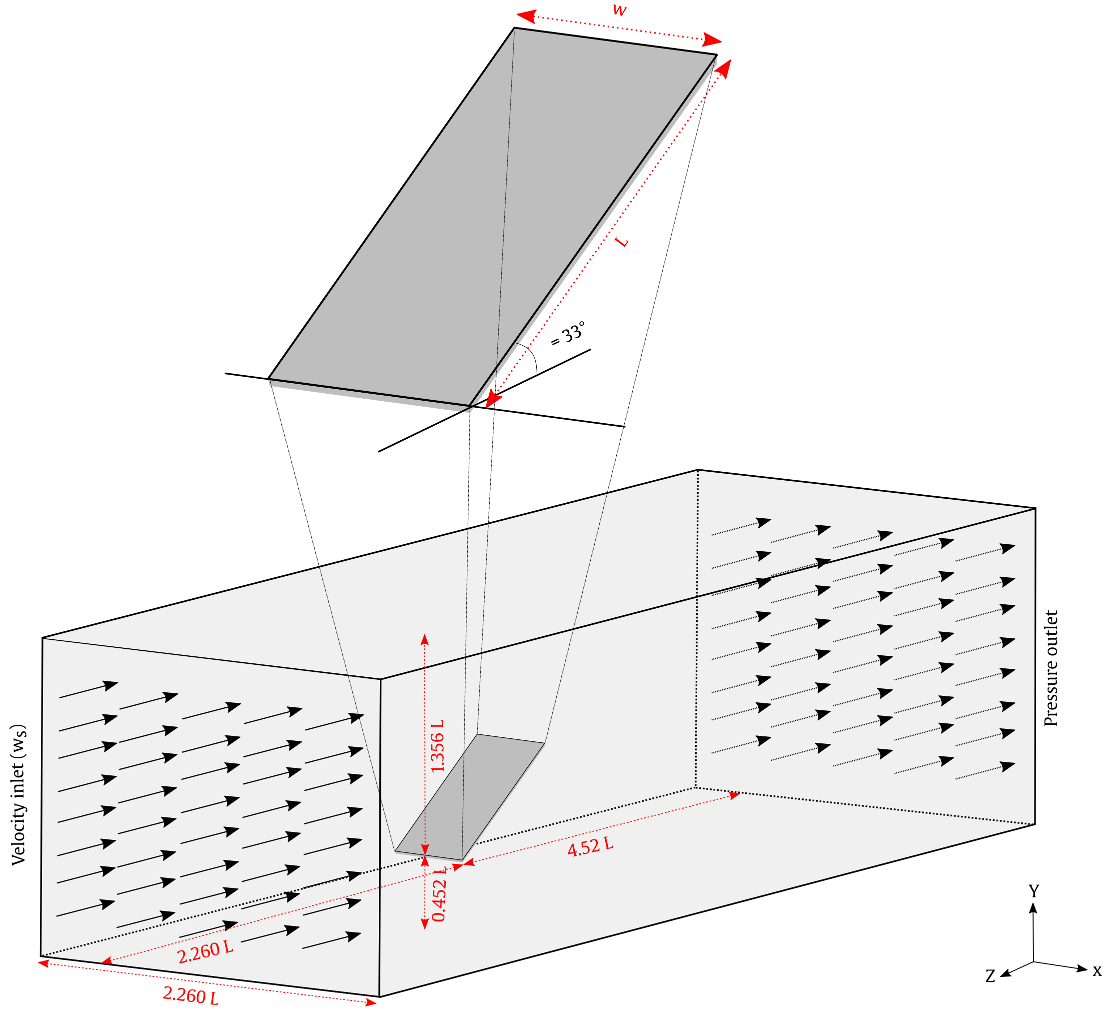

Figure III.1: Photovoltaic module's inclination angle and physical model for the photovoltaic module and surrounding air considered for simulations [171].

Table III.1: Properties of different material for the considered physical model [171].

Material	$\rho\ (kg.m^{-3})$	$k\ (W.m^{-1}.K^{-1})$	$C_p\ (J.kg^{-1}.K^{-1})$	$t\ (mm)$	$\mu\ (Pa.s)$
Glass	2515	0.98	820	3.2	−
EVA	960	0.31	2090	0.4	−
Cells	2330	150	712	0.4	−
TPT	1162	0.23	1465	0.35	−
Air	1.225	0.024	1006.43	−	$1.7894.10^{-5}$

III.2.2 Mathematical formulation

For simulations of fluid flow and heat transfer, the Navier-Stokes equations usually need to be solved numerically, along with the energy equation. In scenarios where turbulence is a significant factor, additional modeling equations are often necessary. Several approaches exist for modeling turbulence, including Large Eddy Simulations (LES), the eddy viscosity modeling techniques, and various hybrid combinations of these methods. Although LES method is computationally demanding, the eddy viscosity approximation, involving the solution of Reynolds Averaged Navier-Stokes equation, or in short, the RANS equations, is less resource-intensive and offers acceptable results. Hence, in this study, the two-equation k-ϵ model, a commonly utilized turbulence model for such applications [114, 119, 134], is employed for the solution of the governing equations to determine the temperature distribution, the flow field and calculate the surface temperature of the module.

III.2.2.1 Governing equations

For the stand-alone photovoltaic module being studied, the adjacent air is assumed to be incompressible, with constant thermos-physical properties, and the flow is considered turbulent. In light of those hypotheses, the continuity, RANS and the energy equations can be expressed as follows:

$$\frac{\partial(\rho u_i)}{\partial x_i} = 0 \tag{III.1}$$

$$\frac{\partial(\rho u_i)}{\partial t} + \frac{\partial(\rho u_i u_j)}{\partial x_j} = -\frac{\partial p}{\partial x_i} + \frac{\partial}{\partial x_i}\left[\mu\left(\frac{\partial u_i}{\partial x_j} + \frac{\partial u_j}{\partial x_i} - \frac{3}{2}\delta_{ij}\frac{\partial u_j}{\partial x_j}\right)\right] + \frac{\partial}{\partial x_j}\left(-\rho\overline{u_i' u_j'}\right) \tag{III.2}$$

$$\frac{\partial(\rho c_p T)}{\partial t} + \nabla.\left(\rho u_i c_p T\right) = \nabla.q + S_e \tag{III.3}$$

where $\rho\overline{u_i' u_j'}$ is referred to as Reynolds stresses. To provide a closure for the system of governing equations, Reynolds stresses must be modeled; a widely adopted approach is the Boussinesq hypothesis, frequently used in different eddy viscosity turbulence models. In this work, the $k - \epsilon$ turbulence model is implemented for simulations, which is presented in the section of numerical procedure.

In Eq. (III.3), the source term (S_e) denotes the heat source per unit volume within the solid photovoltaic module, and is comprised of two key terms: the absorbed solar radiation, which is a positive contribution, and the generated power output delivered by the photovoltaic module, which serves as a negative contribution. The modeling of this source term is presented as follows:

$$S_e = \frac{AG - P_{pv}}{V} \tag{III.4}$$

$$P_{pv} = \eta_{ref}\left(1 - \mu_{ref}\left(T - T_{ref}\right)\right)AG \tag{III.5}$$

In this formulation, A and V are respectively, the area and volume of the photovoltaic module, P_{pv} is its power output, η_{ref} is its efficiency at STC, T_{ref} denotes the module's temperature at reference state, μ_{ref} represents the temperature coefficient, that is assumed to be constant for simplicity, while T stands for the module's operating temperature.

III.2.2.2 Boundary and initial conditions

Within this work, various inlet velocities corresponding to the collected experimental wind speed data are assigned at the inlet of the domain, along with the ambient temperature. regarding the outlet, a pressure outlet boundary condition is implemented. The temperatures at the other boundaries of the domain are specified to be maintained at ambient temperature (left and right sides), whereas at the top side (sky), the temperature is calculated using Eq. (III.6) [130]. While at the bottom side (ground), temperature is approximated using Eq. (III.7) [172]:

$$T_{sky} = 0.0552\, T_a^{1.5} \tag{III.6}$$

$$T_{gr} = 17.898 + 0.951 T_a \tag{III.7}$$

Initially, pressure, velocity and temperature fields within the domain were set to a domain averaged constant value by solving a suitable Laplace equation for each variable. Furthermore, Table III.2 provides a summary of the various boundary conditions assigned at the domain's boundaries, which align with the relevant experimentally recorded data that is used to achieve the numerical solution.

Table III.2: The boundary conditions considered for the simulations.

Boundary	Boundary condition	Value
Inlet	Velocity inlet	Wind speed (W_s) values
Outlet	Pressure outlet	Zero gage pressure
Top side (Sky)	No slip wall, $T = T_{sky}$	Calculated by Eq. (III.6)
Bottom side (Ground)	No slip wall, $T = T_{gr}$	Calculated by Eq. (III.7)
Right and left sides	No slip wall, $T = T_a$	Ambient temperature (T_a) values

III.2.3 Numerical procedure

The simulation of fluid dynamics and heat transfer around a photovoltaic module necessitates solving the continuity, RANS, and the energy equations to establish the temperature flow and fields. To address the presence of turbulence in the flow, the $k-\epsilon$ model is utilized in this study. Consequently, the transport equations for two additional quantities, that is the turbulent kinetic energy and its dissipation rate, are solved concurrently with the aforementioned governing equations. The subsequent section will introduce the $k-\epsilon$ turbulence model.

III.2.3.1 Modeling turbulence

In order to study the phenomena of transient fluid flow and heat transfer within the photovoltaic module, as well as its surrounding air field, the computational fluid dynamics (CFD) software ANSYS Fluent was utilized. The Fluent solver, which is a finite volume method based CFD code, offers the possibility to numerically solve the governing equations of continuity, momentum, and energy equation. For this purpose, the standard $k-\epsilon$ turbulence model was implemented to solve the Reynolds-Averaged Navier-Stokes (RANS) equations. This model is a well-validated turbulence model recognized for its effectiveness in fully turbulent flows, as well as its efficiency and robustness in terms of computational cost. The transport equations for the turbulent kinetic energy k and the turbulence dissipation rate ϵ are expressed as follows [173]:

$$\frac{\partial(\rho k)}{\partial t}+\frac{\partial(\rho k u_j)}{\partial x_j}=\frac{\partial}{\partial x_j}\left[\left(\mu\frac{\mu_t}{\delta_k}\right)\frac{\partial k}{\partial x_j}\right]+G_k+G_b-\rho\epsilon-Y_M+S_k \tag{III.8}$$

$$\frac{\partial(\rho\epsilon)}{\partial t}+\frac{\partial(\rho\epsilon u_j)}{\partial x_j}=\frac{\partial}{\partial x_j}\left[\left(\mu\frac{\mu_t}{\delta_\epsilon}\right)\frac{\partial\epsilon}{\partial x_j}\right]+\rho C_1 S\epsilon-\rho C_2\frac{\epsilon^2}{k+\sqrt{\nu\epsilon}}+C_{1\epsilon}\frac{\epsilon}{k}C_{3\epsilon}G_b+S_\epsilon \tag{III.9}$$

Here, μ_t represents the eddy viscosity, which is calculated using the following expression:

$$\mu_t = \rho C_\mu \frac{k^2}{\epsilon}$$

In this context, C_μ is constant, and the model constants are: $C_{1\epsilon} = 1.44$, $C_{2\epsilon} = 1.92$, $\delta_k = 1.0$, $\delta_k = 1.0$ and $\delta_\epsilon = 1.3$. More elaborate information on the equations of the model is provided in reference [173]. being empirically determined, these model constants can lead to uncertainties in simulation results. Moreover, uncertainties related to turbulence modeling may also arise from various factors, including turbulence closure assumptions, modeling effects in the near-wall region, and conditions related to free-stream and inlet turbulence specifications.

III.2.3.2 Modeling radiation

In order to integrate radiation heat transfer into the numerical simulations, the surface-to-surface (S2S) radiation model was utilized. This model, available within ANSYS Fluent, is widely used and validated in the literature, recognized as a computationally efficient model, and also for its capability to support steady-state, as well as transient simulations. It operates under the assumption of gray and diffuse surfaces, meaning that for the participating surfaces, the emissivity and absorptivity are independent of the wavelength, with emissivity equaling absorptivity. Additionally, the model assumes that the surfaces are opaque, allowing the neglect of transmissivity. For diffuse surfaces, the reflectivity is treated as unaffected by either outward or inward directions. [173]. Consequently, the radiative energy emitted from a specific surface k is described by Eq. (III.10):

$$q_{out,k} = \epsilon_k \sigma T_k^4 + \rho_k q_{in,k} \tag{III.10}$$

where ϵ_k is the surface's emissivity, σ is the Stefan-Boltzmann constant, and ρ is $1 - \epsilon_k$, whereas $q_{in,k}$ is the flux of energy received by same surface. The magnitude of that radiative energy depends on the "view factor F_{jk}". The incoming radiative heat flux $q_{in,k}$ can be calculated using the following equation:

$$A_k q_{in,k} = \sum_j^n A_j q_{out,j} F_{jk} \tag{III.11}$$

Here, A_k is the area of the surface k and F_{jk} is the view factor between the area j and k. n is the number of contributing surfaces. The emissivity coefficients for the different surfaces in the model are shown in Table III.3.

Table III.3: Emissivities of the surfaces participating in radiative heat transfer.

Surface	Glass	TPT	Sky	Ground
ϵ	0.91	0.85	0.91	0.94

III.2.3.3 Mesh sensitivity test

To eliminate potential uncertainties, a sensitivity test on the mesh quality was conducted to verify the solution’s accuracy and omit any discrepancies related to inadequate mesh refinement level or near walls regions and boundaries treatment. The numerical results in all simulations were derived utilizing the standard $k-\epsilon$ turbulence model alongside the enhanced wall functions, aiming for Y^+ values of one (1) for resolving the near-wall region numerically and to guarantee reliable predictions of the wall shear stress and heat transfer. Moreover, first-order and second-order accurate schemes of discretization were utilized for the temporal and spatial terms in the governing equations, respectively. For the pressure-velocity coupling, the Coupled algorithm was employed in all simulations. Although it is computationally intensive, this fully implicit algorithm offers advantages over alternative methods. Results and specifics of the mesh sensitivity test are presented in Table III.4. highlighting mesh element counts, simulation times, and the rate at which the module’s back temperature (T_{back}) changes. Notably, mesh 04, illustrated in Figure III.2, can be considered as the optimal mesh for subsequent investigations as it yielded reliable bac-side temperature predictions, with any further refinement resulting in merely increased computational costs.

Table III.4: Results of mesh sensitivity analysis.

Mesh #	Number of elements	T_{back} $(°C)$	Abs. Change
01	714558	47.840	−
02	828688	47.860	0.020
03	993695	47.877	0.017
04	1188376	47.900	0.023
05	1499054	47.905	0.005

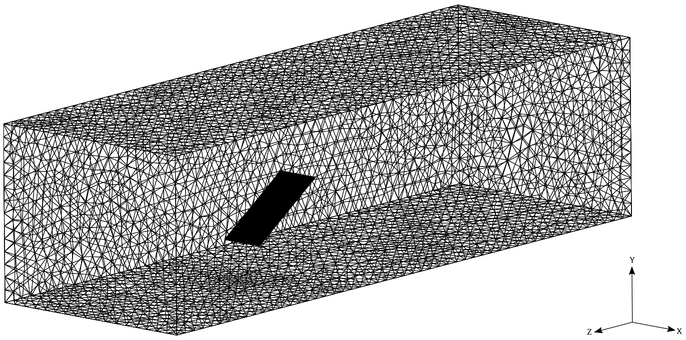

Figure III.2: 3-Dimensional perspective of chosen mesh.

III.2.3.4 Validation

For the verification and validation of the developed numerical model’s accuracy in this work, the experimental study conducted by Aly et al. [82] was simulated with the measured data from their study. This simulation was performed with similar ambient conditions of ambient temperature, solar radiation, and wind speed as observed on June 25, 2014, utilizing similar material properties and dimensions outlined in their research, while applying the CFD code developed in this study. As shown in Figure III.3, the results from the current CFD code closely matched the experimental data, demonstrating a high level of accuracy in predicting the photovoltaic module operating temperature throughout the daytime on June 25, 2014. This strong agreement indicates that the model used in this work is both suitable and reliable for the subsequent investigation. Additionally, the MAE of simulation results was at 2.379, while the MSE was at 7.12, with a MAPE of 7.171% and an R^2 of 0.991, indicating accurate prediction by the CFD model.

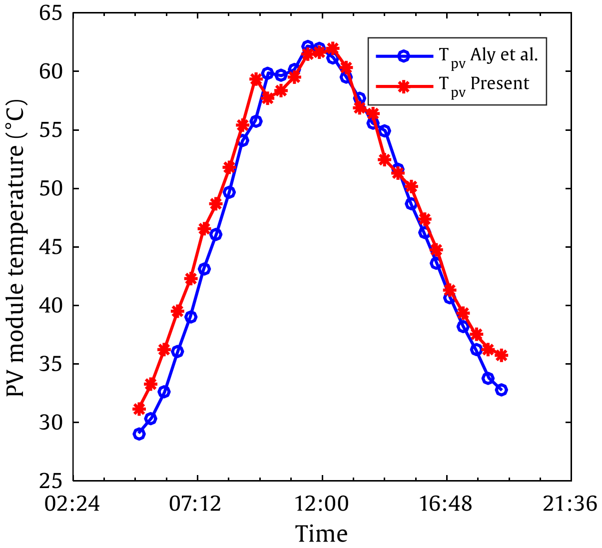

Figure III.3: Validation of the simulation model with study performed by Aly et al. [82].

III.3 Thermal modeling

III.3.1 Energy balance method

It is well established that the temperature of a photovoltaic module can be affected by various factors, including ambient temperature, solar radiation, and wind speed. Consequently, when conducting an energy balance to determine the operating temperature of the photovoltaic module, basic heat transfer mechanisms must be taken into account. Such mechanisms typically involve all three modes of heat transfer (conduction, convection, and radiation), occurring on both the top and back sides of the module. The standard equation for conducting an energy balance on the module is given as follows:

$$(\tau\alpha)G = \eta_{pv}G + U_{top}(T_{cell} - T_a) + U_{back}(T_{cell} - T_a) \qquad \text{(III.12)}$$

It is important to note that in Eq. (III.12), the heat loss is referenced relative to T_a for simplicity. Whereas, in reality, the various heat exchanges between a photovoltaic module and its environment are illustrated in Figure III.4, Here, the radiative heat transfer taking place on the module's top and back sides is regarded as it is with respect to T_{sky} and T_{gr}, respectively, which is the approach taken in this study. In Eq. (III.12), the first term on the right-hand side, represents the power output delivered by the module, where η_{pv} denotes the module's efficiency, which can be expressed as Eq. (III.13):

$$\eta_{PV} = \eta_{ref}\left(1 - \mu_{ref}\left(T_{cell} - T_{ref}\right)\right) \qquad \text{(III.13)}$$

where η_{ref} represents the module's efficiency under Standard Test Conditions, T_{ref} is the module's temperature at reference conditions, μ_{ref} denotes the temperature coefficient. For simplicity, this coefficient is assumed to be constant in this study. The subsequent section provides further details on the determination of U_{top} and U_{back}, as well as the heat conduction through the various layers of the module.

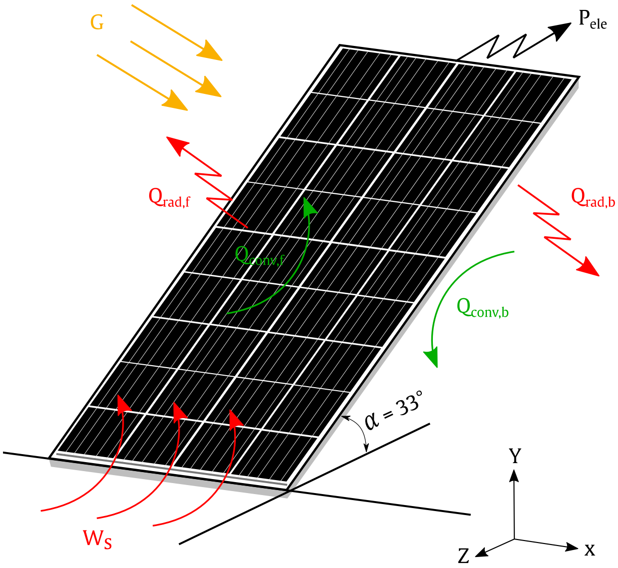

Figure III.4: Schematic illustration of various exchanges of heat between the PV module and its environment [174].

III.3.2 Modeling approach

This section focuses on photovoltaic modules’ thermal modeling, with the primary aim of determining the convective and radiative heat losses from the module to its environment, as well as modeling heat transfer (conduction) across the various layers of the photovoltaic module. Additionally, this investigation examines and estimates the profiles of temperature for the module’s cells and its top and back surfaces. This analysis ultimately facilitates the estimation of module temperature, efficiency, and power output. To achieve this, an equivalent thermal resistances model, as illustrated Figure III.5, is considered for examination. The photovoltaic module under consideration consists of five distinct layers: glass, Ethylene Vinyl Acetate (EVA), photovoltaic cells, EVA, and a back-sheet made of Tedlar Polyester Tedlar (TPT). The thermal conductivity and the thickness of each layer are presented in Table III.5

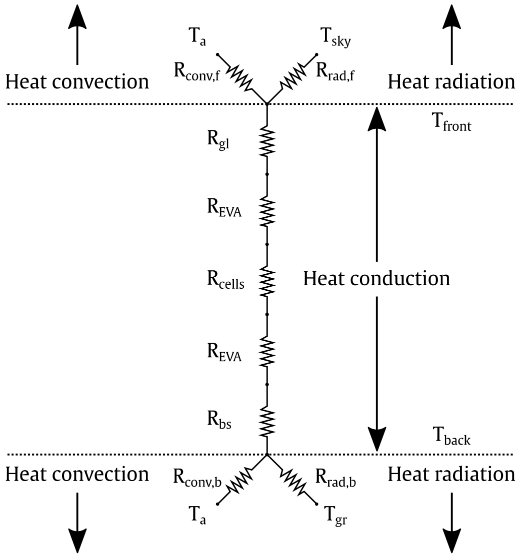

Figure III.5: Equivalent thermal resistances model [174].

Table III.5: Thermal conductivity and thickness of each layer in the PV module [174].

Material	$k\ (W.m^{-1}.K^{-1})$	$t\ (mm)$
Glass	0.98	3.2
EVA	0.31	0.4
Cells	150	0.4
TPT	0.23	0.35

III.3.3 Convective heat losses

The heat transfer by convection from the photovoltaic module to its ambient environment plays a crucial role in predicting the cell temperature T_{cell}. This process is characterized by the convective heat transfer coefficient h_{conv} on the top and back sides of the module. Consequently, it can be generally expressed by Newton's law of cooling, represented per unit area in Eq. (III.14).

$$q'' = h_{conv}(T_s - T_f) \tag{III.14}$$

In this context, T_s and T_f refer to the solid surfaces and the fluid (air) temperatures, respectively. The amount of convection heat transfer is influenced by ambient conditions, particularly the ambient temperature and wind speed on the top and back sides of the photovoltaic module. In cases with high wind speed (W_s) forced convection is anticipated.

III.3.3.1 Forced convection

Over the surface of the PV module, the convective heat transfer coefficient, h_{conv} can be determined using empirical correlations. The flow conditions are characterized by the Reynolds number (Re) which indicates whether the flow is laminar, transitional, or fully turbulent. Specifically, the flow is classified as fully laminar when Re is in the range of 1×10^5, fully turbulent when Re exceeds 3×10^6, and transitional flow occurs in between these values [175]. The empirical correlations for the average Nusselt number Nu_{ave} for various flow conditions are provided below [15], with Nu_{ave} calculated as follows:

$$Nu_{ave} = \frac{h_{conv} L}{k_f} \tag{III.15}$$

For laminar flow:

$$Nu_{ave} = 0.664 Re^{1/2} Pr^{1/3} \tag{III.16}$$

For turbulent flow:

$$Nu_{ave} = 0.037 Re^{4/5} Pr^{1/3} \tag{III.17}$$

For mixed boundary layers:

$$Nu_{ave} = (0.037 Re^{4/5} - A) Pr^{1/3} \tag{III.18}$$

where $A = 0.037 Re_c^{4/5} - 0.664 Re_c^{0.5}$, and $Re_c = 5 \times 10^5$. It is essential to note that the properties of the fluid (air) are calculated at $T_{film} = (T_s + T_f)/2$. Instead, other models are presented in the literature (Table III.6), these models can be used to calculate h_{conv}. Sparrow et al. [176, 177] suggested a model equations for h_{conv} of the form $j = aR_e^b$; where $j = (h_{conv}/\rho C_p W_s) Pr^{2/3}$. Whereas Test et al. [178], Kumar et al. [179], and Jayamaha et al. [180] showed that the wind heat transfer coefficient can be calculated through a simple linear equation, such as: $h_{conv} = aW_s + b$. Furthermore, Sartori [181] suggested that, grounded on the Nusselt number correlations, h_{conv} can be calculated using model equations of the form $h_{conv} = aW_s L^b$. Moreover, details on calculation of h_{conv} and its estimating equations can be found in [182].

Table III.6: Samples of model equations for the wind heat transfer coefficient [174].

No.	Author(s)	h_{conv} equation	W_s limit	Eq.	Ref.
1	Nusselt–Jurges	$h_{conv} = 3.95W_s + 5.8$	$W_s \leq 5\ m/s$	(III.19)	[182]
2	McAdams	$h_{conv} = 3.8W_s + 5.7$	$W_s \leq 5\ m/s$	(III.20)	[183]
3	Sparrow et al.	$j = 0.86R_e^{1/2}; j = (h_{conv}/\rho C_p W_s)Pr^{2/3}$	–	(III.21)	[177]
4	Watmuff et al.	$h_{conv} = 3W_s + 2.8$	$W_s \leq 5\ m/s$	(III.22)	[184]
5	Test et al.	$h_{conv} = 2.56W_s + 8.55$	$W_s \leq 5\ m/s$	(III.23)	[178]
6	Kumar et al.	$h_{conv} = 4.687W_s + 10.03$	$W_s \leq 5\ m/s$	(III.24)	[179]
7	Sharples and Charlesworth	$h_{conv} = 2.2W_s + 8.3$ $h_{conv} = 3.3W_s + 6.5$	$W_s \leq 6\ m/s$	(III.25) (III.26)	[185]
8	Sartori	$h_{conv} = 3.83W_s L^{-0.5}$ $h_{conv} = 5.74W_s L^{-0.2}$ $h_{conv} = 5.74W_s L^{-0.2} - 16.46L^{-1}$	Lam. flow Turb. flow Mixed flow	(III.27) (III.28) (III.29)	[181]
9	Kumar and Mullick	$h_{conv} = 3.87W_s + 6.9$ $h_{conv} = 6.63 + 3.87W_s^{0.8} L^{-0.2}$	$W_s \leq 1.12\ m/s$	(III.30) (III.31)	[186]
10	Schott	$h_{conv} = 5.79W_s^{0.8} L^{-0.2}$	$W_s \geq 0.3\ m/s$	(III.32)	[95]
11	Jayamaha et al.	$h_{conv} = 1.444W_s + 4.955$	$W_s \leq 4\ m/s$	(III.33)	[180]
12	Shakerin	$j = 1.23R_e^{-1/2}; j = (h_{conv}/\rho C_p W_s)Pr$ $j = 0.9R_e^{-1/2}; j = (h_{conv}/\rho C_p W_s)Pr$	–	(III.34) (III.35)	[187]

III.3.3.2 Free convection

Regarding the back side of the photovoltaic module, a widely recognized correlation for the average Nusselt number Nu_{ave} is employed to calculate the convective heat transfer coefficient h_{conv} across the entire range of Rayleigh numbers Ra number, This is represented in Eq. (III.36) taking into account that g is replaced by $g\cos\theta$ and $0 < \theta < 60°$, (θ being measured from the vertical) [188, 189].

$$Nu_{ave} = \left(0.825 + \frac{0.387(Ra_L cos\theta)^{1/6}}{(1 + (0.479/Pr)^{9/16})^{8/27}}\right)^2 \tag{III.36}$$

where $Ra_L = GrPr = g\beta(T_s - T_f)L^3/\nu\alpha$, and $\beta = 1/T_{film}$. Furthermore, Fujii and Imura [190, 191] suggested that the average Nusselt number Nu_{ave} on an inclined plate's rear surface can be calculated using Eq. (III.37) This equation is applicable for Rayleigh number values $Ra_L cos\theta$ ranging from 10^5 to 10^{11} and for angles of inclination greater than 2°, whereas, Kaplani and Kaplanis [130] noted that this equation is valid for angles up to approximately 30°, beyond which, Eq. (III.36) is recommended.

$$Nu_{ave} = 0.56(Ra_L cos\theta)^{1/4} \tag{III.37}$$

Regarding the top surface of the photovoltaic module, and since it usually operates at a with superior temperature values than its surrounding, the boundary layers become disrupted, leading to the formation of thermal plumes on the upper side of the module. This phenomenon enhances the heat transfer rate compared to a vertically oriented plate [192]. Accordingly, Fujii and Imura [190] proposed that the Nusselt number for the upper face of a heated inclined plate can be determined using the following correlation:

$$Nu_{ave} = 0.13\left(GrPr^{1/3} - Gr_c Pr^{1/3}\right) + 0.56(Gr_c Pr\, cos\, \theta)^{1/4} \tag{III.38}$$

where Gr_c represents the Grashof number at which the flow begins to transition from laminar to turbulent behavior. The corresponding values for Gr_c related to different angles θ can be found in literature [130, 191, 193].

III.3.3.3 Mixed convection

The heat transfer by convection is classified as mixed if the influence of both forced and free convection are equivalent, making it impossible to disregard either effect. Specifically, convection is regarded as free when $Ri \gg 1$, forced when $Ri \ll 1$, and mixed when the Richardson number (Ri) number is in between those limits ($Ri \sim 1$), where $Ri = Gr/Re^2$. The average Nusselt number Nu_{ave} for mixed convection can be expressed as follows [15]:

$$Nu_{ave} = \left(Nu^n_{ave,forced} + Nu^n_{ave,free}\right)^{1/n} \tag{III.39}$$

The exponent n ranges from 3 to 4, with optimal results typically achieved at $n = 3$, However, values of 3.5 and 4 may be more appropriate for transverse flows involving horizontal plates and cylinders (or spheres), respectively [15].

III.3.4 Radiative heat losses

In this study, radiative heat transfer between the photovoltaic module and its surroundings is accounted for using Eq. (III.40) which expresses the radiative heat flux per unit area.

$$q'' = \sigma\epsilon(T_s^4 - T_{surr}^4) \tag{III.40}$$

In this equation, σ denotes the Stefan-Boltzmann constant, and ϵ signifies the material's emissivity, with T_s indicating the temperature of the module's top or back surface. The temperature of the sky, T_{sky}, is calculated using Eq. (III.41) [130], while the ground temperature, T_{gr}, is estimated using Eq. (III.42) [172], Both of these temperatures are represented as T_{surr} in Eq. (III.40).

$$T_{Sky} = 0.0552\, T_a^{1.5} \tag{III.41}$$

$$T_{gr} = 17.898 + 0.951 T_a \tag{III.42}$$

It's important to highlight that T_a, T_s, and T_{surr} must be expressed in Kelvin (K). Furthermore, because radiative heat transfer is a surface phenomenon that relies on the orientation of surfaces, the concept of the view factor is essential for determining the proportion of radiation emitted from one surface that is intercepted by another. The view factor, F, is crucial in modeling the thermal behavior of photovoltaic modules and can be calculated using Eqs. (III.43) to (III.46) [130, 194]:

$$F_{f-sky} = (1 + \cos(\alpha))/2 \tag{III.43}$$

$$F_{f-gr} = (1 - \cos(\alpha))/2 \tag{III.44}$$

$$F_{b-sky} = (1 + \cos(\pi - \alpha))/2 \tag{III.45}$$

$$F_{b-gr} = (1 - \cos(\pi - \alpha))/2 \tag{III.46}$$

Therefore, in this study, the radiative heat transfer from the photovoltaic module to the surrounding surfaces can be expressed adequately by the mean of a radiative heat transfer coefficient h_{rad} as follows:

$$q'' = h_{rad}(T_s - T_{surr}) \tag{III.47}$$

where h_{rad} is the heat transfer coefficient for radiation, and it takes the linearized form of Eq. (III.48):

$$h_{rad} = F\sigma\epsilon\,(T_s^2 + T_{sur}^2)(T_s + T_{sur}) \tag{III.48}$$

III.3.5 Overall heat transfer coefficient

As it is evident from Eq. (III.12), the model equation for T_{cell} can be expressed in an equation similar to that of Ross model [89], as shown in Eq. (III.49), where $T_{cell} - T_a$ is linearly correlated with the incoming solar radiation, with constant scaling factor known as k.

$$T_{cell} = T_a + kG \tag{III.49}$$

Here, k is given by $\left(\tau\alpha - \eta_{pv}\right)G/U_{loss}$, and $U_{loss} = U_{top} + U_{back}$. These two quantities are calculated from Eqs. (III.50) and (III.51), respectively.

$$U_{top} = \left[\frac{1}{h_{conv.f} + h_{rad.f}} + R_{cond.f}\right]^{-1} \tag{III.50}$$

$$U_{back} = \left[\frac{1}{h_{conv.b} + h_{rad.b}} + R_{cond.b}\right]^{-1} \tag{III.51}$$

However, calculating the values of U_{top} and U_{back} for both side of the module inherently requires determining the temperature at these surfaces. For instance, for the glass (top) side of the module, the amount of heat released per unit area from the photovoltaic cells, for an average cells temperature T_{cell} to the top side (glass) at an average temperature T_{top} is described by Eq. (III.52). The heat transfer from the glass to the surroundings at temperatures T_a and T_{sky}, is expressed by Eq. (III.53):

$$q''_{top} = \frac{1}{R_{cond.f}}(T_{cell} - T_{top}) \tag{III.52}$$

$$q''_{top} = h_{conv.f}(T_{top} - T_a) + h_{rad.f}(T_{top} - T_{sky}) \tag{III.53}$$

Consequently, T_{top} and T_{back} must be determined numerically using an iterative approach to solve Eqs. (III.52) and (III.53) for h_{rad} and T_{top}, and likewise for the back side. Ultimately, the solutions to all these equations must satisfy the energy balance equation (Eq. (III.49)), which is solved for T_{cell}. It is important to note that h_{rad} can be linearized with respect to T_a for convenience [16, 104].

III.3.6 Proposed simulation algorithm

For the calculation of module operating temperature, a simulation algorithm is presented for the predictive modeling in this study, along with an investigation into the heat transfer exchanges between the module and its surrounding and the various wind and heat transfer coefficients involved. As depicted in Figure III.6 the overall workflow of the algorithm begins with loading the ambient temperature (T_a), wind speed (W_s), and solar irradiance (G). The algorithm then initializes the temperatures at the different layers of the module, specifically T_{top}, T_{back}, and T_{cell}, and calculates the film temperature (T_{film}) on top and back sides of the module.

Following this, the air properties are calculated, and the Reynolds number (Re), Grashof number (Gr), Richardson number (Ri), and Rayleigh number (Ra) are computed to establish the flow conditions. The algorithm then calculates the convective (h_{conv}) and radiative (h_{rad}) heat transfer coefficients based on the initial estimates of T_{top} and T_{back}. After these values are obtained Eqs. (III.52) and (III.53) are solved to refine the initial estimates of T_{top} and T_{back}, followed by solving for T_{cell} using Eq. (III.49).

If the specific convergence criterion of 1% error is met for all values of the different surfaces temperature, the solution for that time step is considered converged, and the algorithm progresses to the next time step. If the convergence criterion is not satisfied, the initial values of temperature are updated, and the loop is repeated.

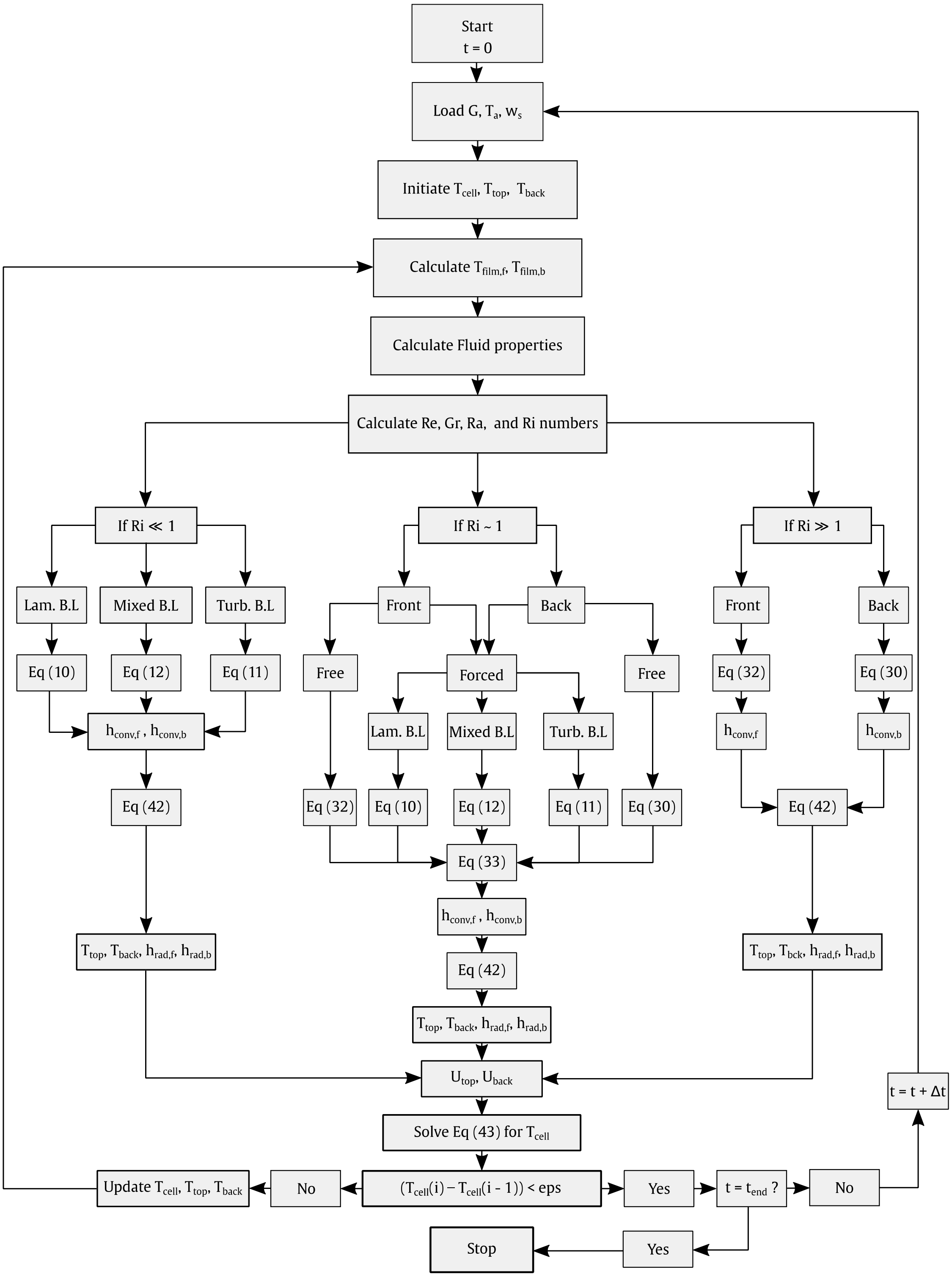

Figure III.6: Overall simulation algorithm procedure [174].

III.3.7 Model validation

For the validation of the thermal model developed in this study and to evaluate its accuracy, simulations were carried out based on the experiments carried out by Aly et al. [82] utilizing the measured data from their work. The simulations were set to match the ambient weather data of air temperature, solar radiation, and wind speed conditions observed on June 25, 2014, which served as the inputs for the model. The primary output of interest was the back temperature T_{back}, The results demonstrated that the current thermal model reasonably estimates T_{back} with a high degree of precision, as illustrated in Figure III.7.

Additionally, the validation results from the simulation algorithm were evaluated through multiple approaches. Firstly, the coefficient of determination (R^2) was found to be 0.986 with an adjusted R^2 of 0.984, indicating a strong correlation between the estimated values and the measured data based on the model inputs used. Secondly, numerous error indictors were evaluated and analyzed, revealing that the predicted module temperature had a mean absolute error (MAE) of 1.322 °C, a root mean squared error (RMSE) of 1.556 °C, and a mean square error (MSE) of 2.420 °C. The mean absolute percentage error (MAPE) was 3.56%, and the standard error was only 1.624 °C.

Furthermore, the residuals of the estimated operating temperature of the module, shown in Figure III.7 indicated that only about 12.5% of the prediction errors exceeded the 2.5 °C limit, and merely 2.08% of errors surpassed 3 °C. Additionally, the relative error recorded by the simulation algorithm was only 0.947% at maximum, which is well below the established convergence criterion of 1%. These findings reinforce the adequacy, relevance, and robustness of the thermal model in this context.

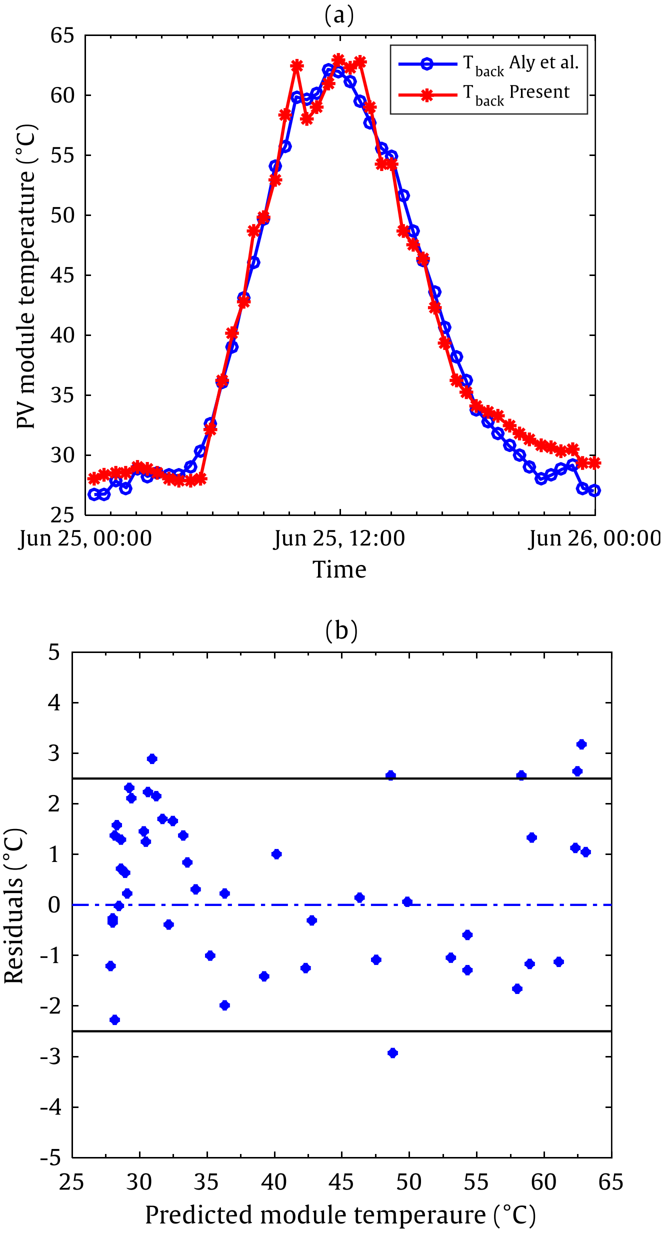

Figure III.7: Validation of current simulation algorithm with data from the study carried out by Aly et al. (a) measured against estimated T_{back}, and (b) residuals' scatter plot [82].

III.4 Conclusion

In CHAPTER III, the opted modeling approaches for this work have been reported and detailed. Firstly, the physical model for the CFD simulations was presented, with the system’s governing equation, boundary, and initial conditions. Additionally, details on modeling turbulence and radiation during simulation were also presented. Furthermore, a mesh independency test and model validation have been conducted and presented for reliability of simulation model. Similarly, the thermal modeling based on the energy balance approach was described in this Chapter, where firstly, the equivalent thermal resistances model was described, after that, governing equations of heat transfer from the module to its surroundings were presented in details, then, the proposed simulation algorithm was described and validated to establish the foundation for the subsequent investigations.

CHAPTER IV : RESULTS AND DISCUSSION

IV.1 Introduction

This chapter presents the key findings from both the data-driven and numerical modeling approaches used to predict photovoltaic (PV) module power output and temperature. The performance of machine learning algorithms is evaluated, focusing on their accuracy in predicting power output under different environmental conditions. Results are analyzed using metrics such as Mean Absolute Error (MAE) and Root Mean Squared Error (RMSE) and compared to actual measurements. Additionally, the outcomes of the thermal modeling and Computational Fluid Dynamics (CFD) simulations are discussed to examine the effects of ambient factors such as wind speed and ambient temperature on photovoltaic modules efficiency. Finally, the results are analyzed to offer insights into optimizing photovoltaics system performance, while discussing potential limitations and areas for future improvement.

IV.2 Power output prediction

In this section, to predict the power output of a photovoltaic (PV) module, simultaneous weather data collection and module power generation recording are conducted. A dataset spanning six days is used for the training, validation, and testing of a feedforward neural network (FFNN) and establishing six the comparison of (06) Distinct training techniques and their influence on the prediction performance of the artificial neural network (ANN). Additionally, multiple linear regression (MLR) analysis is conducted to develop exportable predictive models that effectively estimate the power generation of a photovoltaic module based on climatic data. A further nonlinear model is also suggested. Of the six-day dataset, the initial three days are designated for training the network, the following two days for prediction, while the final day is reserved to test the models’ overall performance in comparison with those proposed in previous studies. The subsequent section is dedicated to an in-depth presentation and analysis of the findings obtained in this study.

IV.2.1 Effective attributes

Pearson’s coefficient of correlation, R, between each feature pair and the output was calculated and visualized as a heatmap in Figure IV.1, which shows that solar radiation exerts the strongest influence on the power output of the PV module, with a correlation coefficient (R) of 0.98, indicating a highly significant relationship. Ambient temperature ranks next, with an R value of 0.613, suggesting moderate importance. Other variables show comparatively lower correlations with power output. Further analysis of the correlations shows that wind direction, having a low R value of 0.259 (less than 0.3), can be excluded from the model's inputs with no significant loss of information. Consequently, the model inputs include ambient air and module temperature, solar radiation, wind speed, and relative humidity, with power generation as the target output.

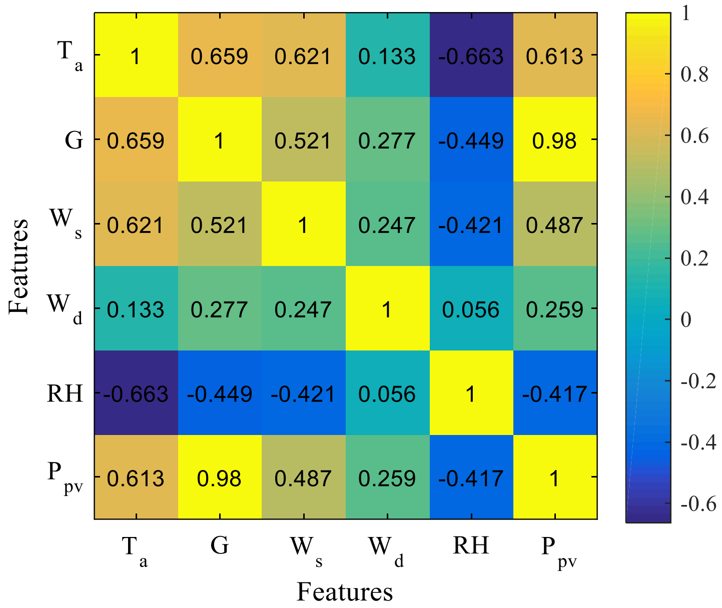

Figure IV.1: Heatmap of correlation coefficient for various input parameters and the output variable in the dataset.

The module operating temperature T_{pv} is omitted from analysis in Figure IV.1 (first dataset) for its strong correlation with ambient temperature T_a, introducing collinearity that may impact model accuracy. This key parameter will instead be examined directly (in the second dataset), alongside irradiation, to assess its impact on module performance and power output [74]. Additionally, the PV panel's operating temperature is significantly influenced by weather conditions [194], which supports grouping these effects into a single parameter, T_{pv}.

To validate this assumption and compare the datasets, correlations between T_{pv} and ambient conditions confirm the expected relationships, as shown in Table IV.1. Here, the strongest correspondence is observed in the relation among the ambient and module temperature ($R = 0.868$), while W_s and RH were exhibiting positive and negative correlations, respectively, with wind speed at $R = 0.621$ and relative humidity at $R = -0.663$. Whereas, wind direction showed a weak correlation with $R = 0.228 < 0.3$.

Table IV.1: Results of correlation analysis of ambient variables and T_{pv}.

	T_a	W_s	W_d	RH	T_{pv}
T_a	1	0.621	0.133	-0.663	0.868
W_s	0.621	1	0.247	-0.421	0.599
W_d	0.133	0.247	1	0.056	0.228
RH	-0.663	-0.421	0.056	1	-0.575
T_{pv}	0.868	0.599	0.228	-0.575	1

IV.2.2 Results of Training algorithms

In order to evaluate the effect of various training algorithms on prediction accuracy, a three hidden layers ANN model—containing 6, 4, and 2 neurons each—was employed. Following a widely accepted data division strategy [195, 196], the dataset was split into 70% for training, 15% for validation, and 15% for testing. For consistency, the number of hidden layers, the number of neurons in each layer, and activation functions were held the same across all simulations to isolate the influence of the training algorithm on the model performance.

Six (06) different training algorithms were examined, and their performance was assessed during the testing phase. As summarized in Table IV.2, the Levenberg-Marquardt algorithm attained minimal error scores, at 1.265 for MAE, 8.543 for MSE, and 2.923 for RMSE, alongside the best coefficient of determination ($R^2 = 0.995$). Though it required slightly more iterations than other algorithms, Levenberg-Marquardt algorithm yielded optimum performance in terms of statistical accuracy and model robustness. Consequently, the Levenberg-Marquardt algorithm was selected for use in this study due to its superior predictive capability. This finding aligns with results reported by Ayan and Toylan [61] and Al-Dahidi et al. [197], further reinforcing its reliability for ANN training in this context.

Table IV.2: Comparative analysis of the considered algorithms.

Training algorithm	Iterations	MAE	MSE	RMSE	R^2
Levenberg-Marquardt	152	1.2650	8.5430	2.9230	0.9950
Resilient Backpropagation	109	1.6180	13.3750	3.6570	0.9930
Scaled Conjugate Gradient	140	1.8080	15.9670	3.9960	0.9920
Fletcher-Powell Conjugate Gradient	150	2.1070	18.6510	4.3190	0.9900
Polak-Ribiére Conjugate Gradient	62	2.4420	27.0700	5.2030	0.9860
One Step Secant	110	1.9720	16.0020	4.0000	0.9920

IV.2.3 Artificial neural network predictions

Once the developed artificial neural network model was tuned, it is then trained and validated on 70% and 30% of the first dataset, respectively, using three days' worth of data (November 26–28, 2022). The dataset includes weather conditions such as ambient temperature (T_a), solar radiation (G), wind speed (W_s), and relative humidity (RH) as inputs, with photovoltaic electrical output (P_{pv}) as the target.

As illustrated in Figure IV.2. the trends of environmental conditions during the training period follow expected daily patterns. Solar radiation and ambient temperature rise from morning until noon, then gradually decrease as the day progresses. Conversely, relative humidity exhibits an inverse trend, decreasing from morning to noon and increasing again towards evening. Wind speed, however, shows a more unpredictable variation throughout the day. This characteristic data behavior provides a representative basis for the model to learn and predict the PV module's power output effectively across different times of the day and under various environmental conditions.

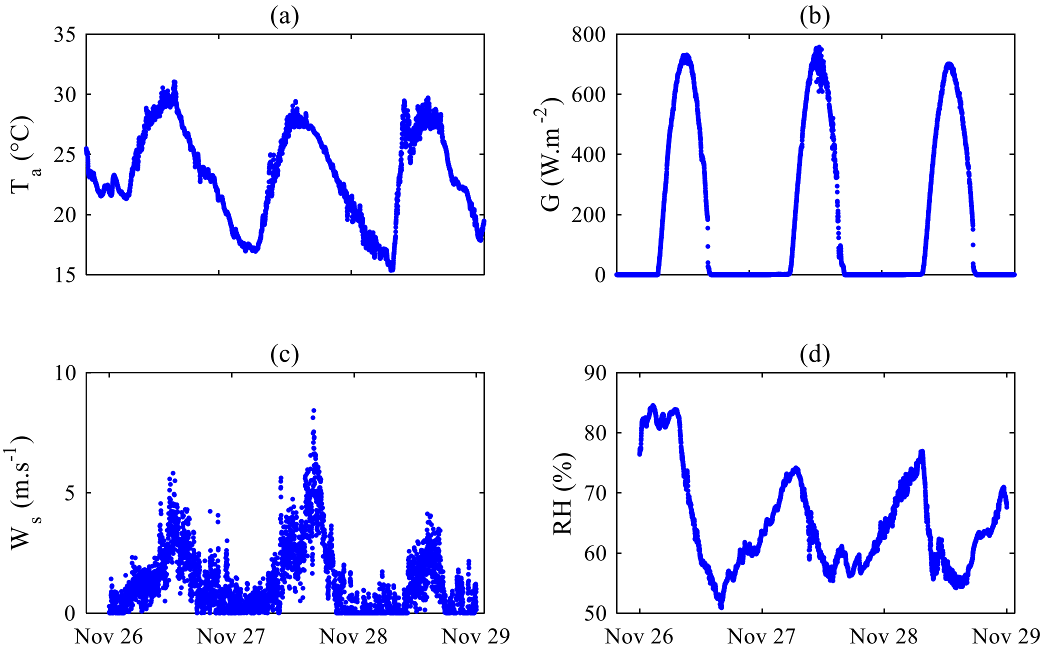

Figure IV.2: Weather data gathered during the period from November 26 to 28 for training purposes, illustrating (a) ambient temperature, (b) solar radiation, (c) wind speed, and (d) relative humidity.

Figure IV.3, demonstrates the strong performance by model during the validation stage, showcasing its effectiveness in predicting photovoltaic power output. The scatter plot comparing predicted and measured values indicates a high level of agreement, suggesting that the model accurately captures the relation between environmental conditions (variables) and power output. Additionally, the performance plot shows that the model achieved its lowest mean squared error (MSE) after 78 epochs, indicating efficient learning and convergence.

These results highlight the model's good predictive capability, even in comparison with other models reported in the literature. The relatively simple architecture of this ANN model thus provides an effective and reliable tool for power prediction, showing promising performance for the testing stage.

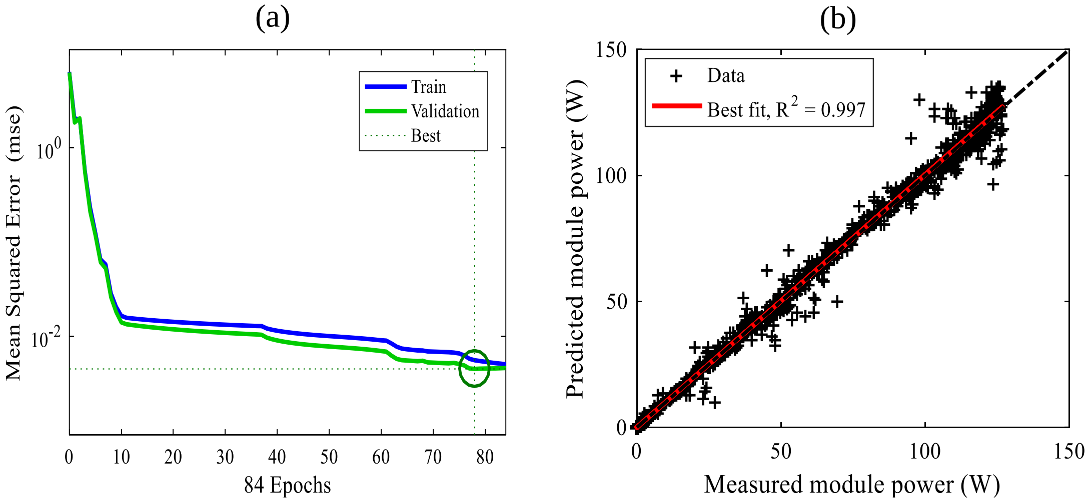

Figure IV.3: Performance of the ANN model's validation, shown in (a), alongside (b) a scatter plot comparing measured versus estimated power output.

Upon using the dataset of forecasting days (29–30 November) with the trained ANN model, it demonstrated strong predictive accuracy in predicting the power output of the photovoltaic module, utilizing a hyperbolic tangent sigmoid activation function across all three hidden layers. As illustrated in Figure IV.4, the predicted power output closely aligns with the measured values, underscoring the model's precision and reliability.

The minimal discrepancies between the predicted and actual power outputs observed in. Figure IV.4 confirm the model's robust predictive performance for short-term forecasts, providing a reliable tool for estimating photovoltaic power generation based on environmental conditions. This high accuracy suggests that the ANN model is well-suited for real-time forecasting applications, particularly for optimizing PV system operations.

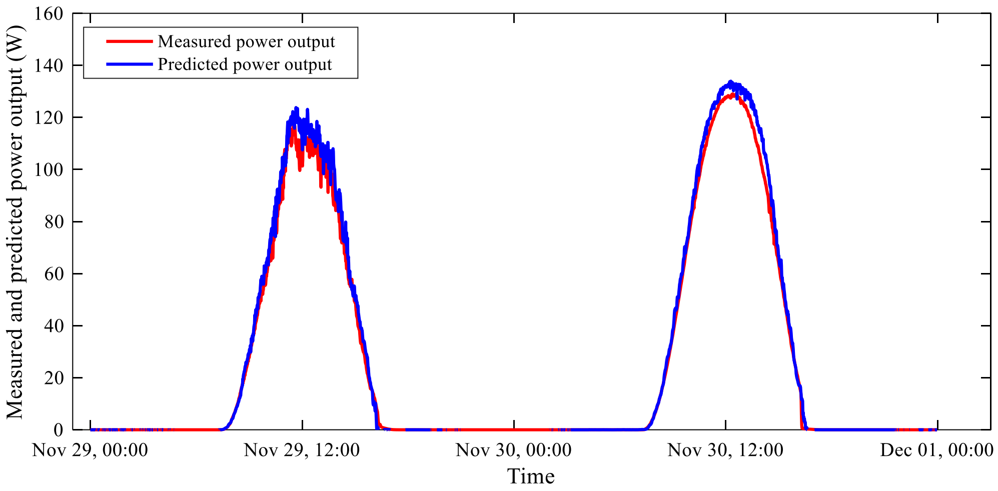

Figure IV.4: Comparison between the actual and predicted module's power output using all-weather variables dataset.

The statistical metrics for the ANN model further reinforce its accuracy and reliability in predicting the power output of the photovoltaic module. Achieving a Mean Absolute Error (MAE) of 1.998, Mean Squared Error (MSE) of 16.810, and Root Mean Squared Error (RMSE) of 4.100, alongside a high correlation coefficient ($R = 0.997$), underscores that 99.7% of the variability in the predicted electrical power is well-explained by the weather inputs used in the model. This high predictive accuracy validates the model's robustness and reliability. As demonstrated in Figure IV.5, the scatter plot comparing predicted and actual power output data reveals predictions clustered closely around the 45-degree line, suggesting minimal deviation from ideal predictions. Such performance not only highlights the ANN model's potential for accurate forecasting in real-time applications but also indicates its suitability for reliable power output estimation under varying weather conditions.

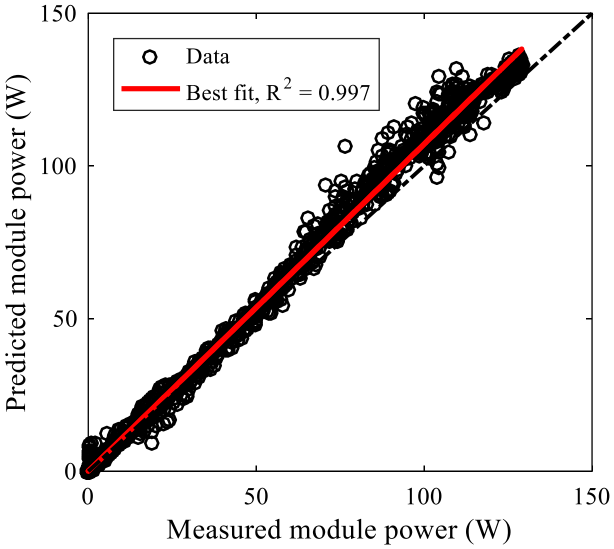

Figure IV.5: Scatter plot illustrating the relationship between predicted and actual power output of the PV panel utilizing all-weather variable dataset.

In a similar fashion, to highlight the effects of module temperature and based on the correlation analysis results presented in Table IV.1, the established ANN model, was modified to be trained using only solar radiation and the module’s temperature, as a different subsection from the training dataset, as illustrated in Figure IV.6, with the objective to estimate the power generation during forecasting (testing) days. Throughout the training phase, the developed model attained the least MSE of 0.0081 at 41 epochs, that is marginally higher than that achieved with the complete dataset of all-weather variables. However, this approach required fewer computations in terms of iterations.

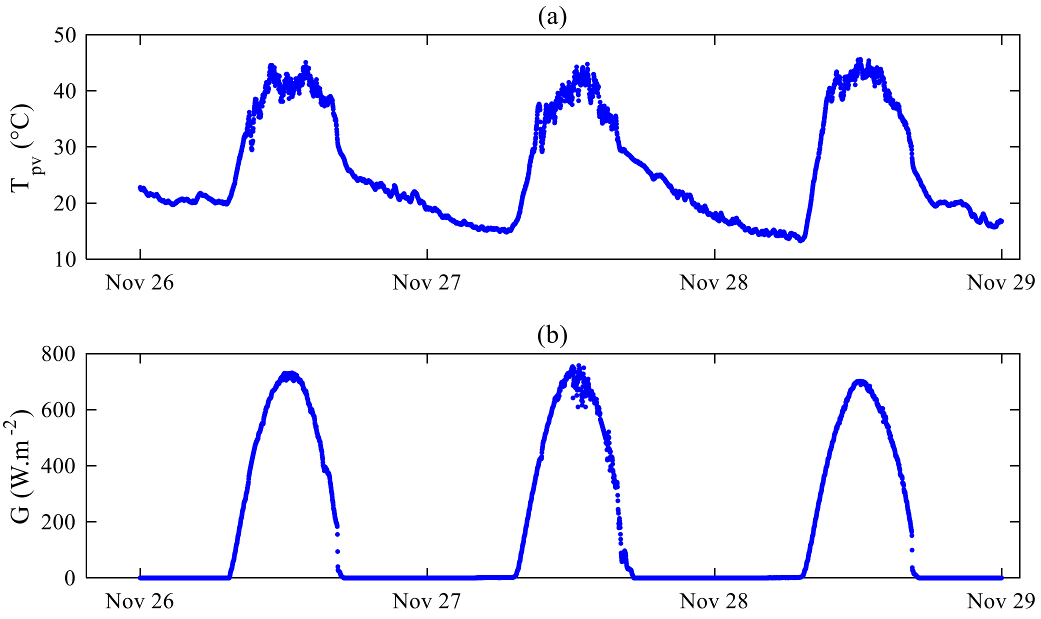

Figure IV.6: Data collected for training from November 26 to 28, depicting (a) module temperature and (b) solar radiation levels.

After the model's training with the subset of data that included solar radiation and operating temperature, the same input variables—T_{pv} and G—were utilized to predict the photovoltaic module's power output. Comparison of the measured and predicted P_{pv}, as shown in Figure IV.7, demonstrate a commendable level of accuracy. The results indicate that using only the two input variables (solar radiation and module temperature) yields outcomes comparable to those obtained when all weather variables are considered. This finding underscores the conclusion that the power output of a photovoltaic module is primarily driven by solar radiation and its operating temperature. Consequently, this reduces the necessity to incorporate a multitude of weather conditions for effective power output predictions, thereby simplifying the modeling process while maintaining accuracy. This streamlined approach can enhance the practicality and efficiency of forecasting power generation in real-world applications.

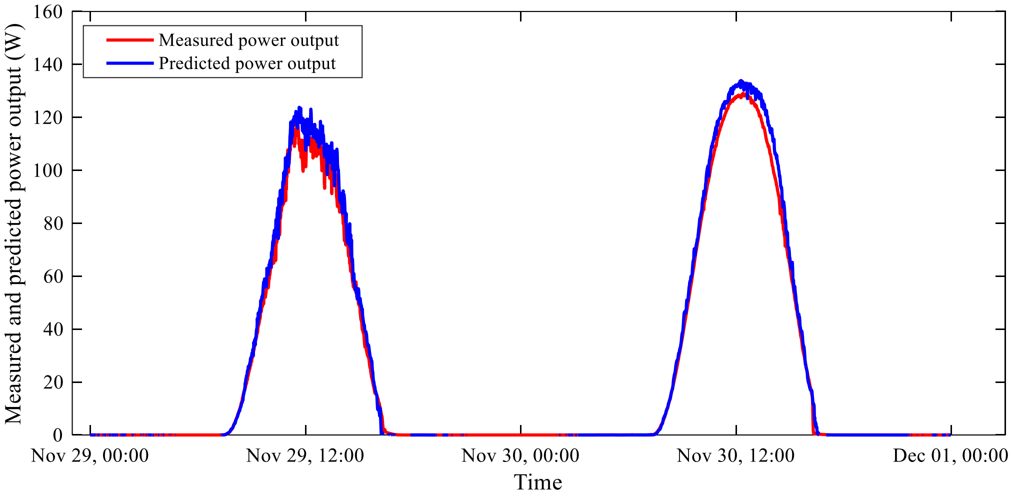

Figure IV.7: Comparison of actual versus forecasted power outputs using module temperature (T_{pv}) and solar radiation (G).

Evaluated by statistical metrics, the prediction of the module's power output using only solar radiation and module's operating temperature, resulted in a Mean Absolute Error (MAE) of 2.046, a Mean Squared Error (MSE) of 21.109, and a Root Mean Squared Error (RMSE) of 4.594. The model also achieved a high correlation coefficient of 0.995, as illustrated in Figure IV.8). This reflects that 99.5% of the variance in the module's power output can be attributed to variations in solar radiation and operating temperature. Notably, this is only a slight decrease of 0.2% compared to the 99.7% variation explained when all weather conditions were included as inputs. These findings emphasize that solar radiation and operating temperature are indeed the key parameters influencing the prediction of power generation and overall module performance. The model demonstrated its capability to estimate the power generation of the photovoltaic module accurately, using both all-weather variables and just the two selected inputs (solar radiation and module's operating temperature). This highlights the predictive reliability and robustness of the developed model. Consequently, the ANN model proves to be suitable for applications in predicting power production for PV panels based on weather data and module temperature. Its effectiveness positions it well for further applications in controlling, designing, and supervising photovoltaic systems, paving the way for optimized performance and operational efficiency in renewable energy management.

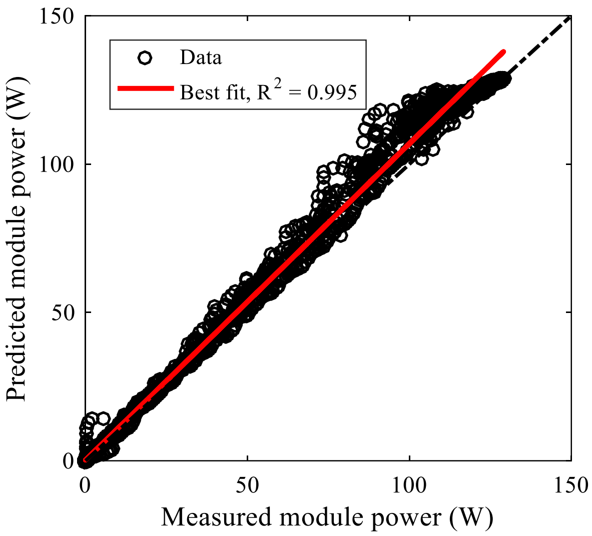

Figure IV.8: Scatter plot illustrating the relationship between measured and predicted power output of the PV panel using module temperature (T_{pv}) and solar radiation (G).

IV.2.4 Regression models' results

To rapidly estimate the power output of a photovoltaic module, based on the provided results from the neural network model, a multiple linear regression (MLR) model is established. This regression model provides a simplified yet effective way to estimate the power output by using key weather parameters as inputs. The MLR equation is represented as:

$$\mathrm{P_{pv}} = -1.258\ \mathrm{T_a} + 0.176\ \mathrm{G} - 1.357\ \mathrm{W_s} - 0.110\ \mathrm{RH} + 30.566 \qquad \text{(IV.1)}$$

In an interpretation of the model's coefficients (i.e., MLR model 01) in Eq. (IV.1), suggests that solar radiation has the most significant positive influence on power output, which aligns with known PV module behavior. Specifically, each increase of $0.176\ W/m^2$ in solar radiation corresponds to a $1\ W$ increase in module power output, when holding other variables constant. Conversely, variables like wind speed, ambient temperature, and relative humidity show negative contributions. For instance, a drop of $1.357\ m/s$ in W_s, with all other parameters held constant, would similarly rise the power output by $1\ W$. The regression statistics—an R^2, adjusted R^2, and predicted R^2 of 0.9652, 0.9652, and 0.9651, respectively—along with p-values below 0.05 and a standard error of 7.789, reinforce the accuracy and reliability of this model. However, examining the predicted versus actual outputs and the residuals in Figure IV.9 (a) and (b), reveals some inconsistencies. The non-uniform and abnormal distribution of residuals in the scatter plots imply that certain weather variables may introduce stochastic variations, affecting prediction accuracy. These observations suggest that while MLR provides a robust first approximation, the underlying stochastic nature of certain inputs may limit linear modeling's effectiveness. Consequently, a nonlinear model is proposed to capture the more complex relationships and enhance predictive precision.

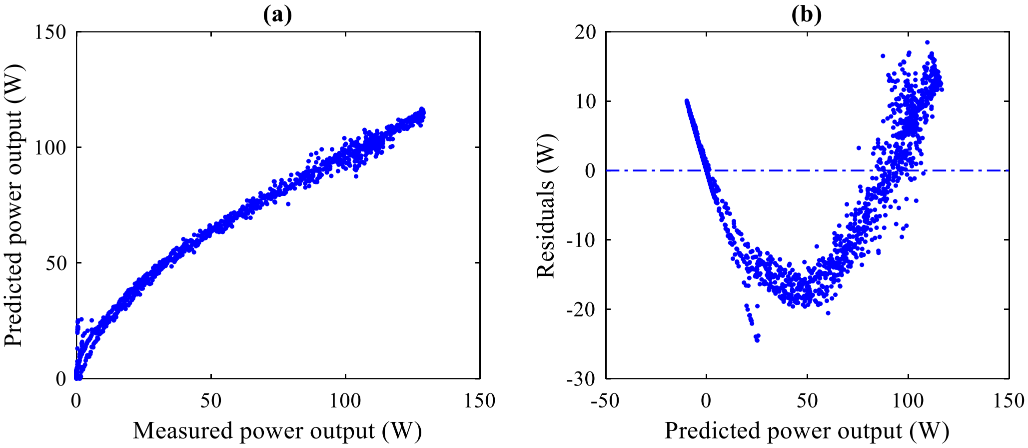

Figure IV.9: Scatter plots of, (a) estimated power generation against the measured one, and (b) residuals of the estimated power generation, for the MLR Model 01.

Given the significant variance contributed by solar radiation and its likely role in introducing stochastic behavior, it's logical to capture its nonlinear influence more effectively. Observations of residuals relative to irradiation suggest that using a quadratic or power law term for irradiation could improve representation of its effect. This approach allows a more flexible response to varying irradiation, capturing its Power-Law tendency. A Rational-Power-Law (RPL) model is thus proposed, structuring positively contributing terms—particularly solar radiation—in the numerator and raising it to a fitted power coefficient, with negatively contributing factors like wind speed, temperature, and humidity in the denominator. This emphasizes irradiation's impact on power output while incorporating the interactions of all predictors in both linear and nonlinear forms. The model is represented in Eq.(IV.2):

$$\mathrm{P_{pv}} = \frac{\mathrm{aG^b}}{\mathrm{T_a}} \frac{1}{\mathrm{e}^{\mathrm{c}\left(\frac{\mathrm{Ws}}{\mathrm{RH}}\right)} + 1} \tag{IV.2}$$

The constants derived for the Rational-Power-Law model are $a = 0.0298$, $b = 1.879$, and $c = 0.297$. While interpreting these coefficients may be less intuitive than those in the MLR model, this model aligns more closely with the underlying physical processes, as suggested by correlation analysis. The model's performance is supported by strong statistical metrics, yielding R^2, adjusted R^2, and predicted R^2 values of 0.9968, 0.9967, and 0.996, respectively, alongside a low standard error of 2.375. The predicted versus experimental power outputs and the prediction residuals in the form of scatter plots shown in Figure IV.10 (a) and (b), further confirm the model's predictive power, showcasing a strong match with low residuals and well-distributed prediction errors. Collectively, these results illustrate that the Rational-Power-Law model outperforms the MLR model, delivering higher predictive accuracy and robustness with reduced variance in residuals.

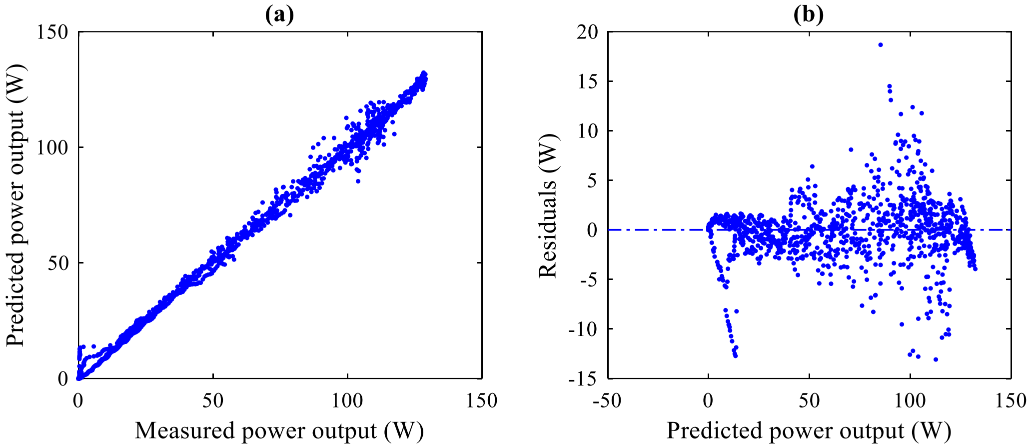

Figure IV.10: Scatter plot of the proposed Rational-Power-Law model. (a) predicted versus experimental electrical output, and (b) prediction residuals.

IV.2.5 Effect of module temperature

When estimating the electrical power generation using only solar radiation and module temperature, a multiple-linear regression can provide a linear equation that relates power generation to these input variables. This model is represented in Eq. (IV.3) as follows:

$$\mathrm{P} = 0.208\ \mathrm{G} - 1.271\ \mathrm{T}_{\mathrm{pv}} + 20.081 \qquad \text{(IV.3)}$$

According to statistical metrics, this model (i.e., MLR model 02) estimates the photovoltaic module's electrical output with an R^2 of 0.9672, an adjusted R^2 of 0.9672, and a predicted R^2 of 0.9671. Both input variables are highly significant ($p - values \ll 0.05$) with a standard error of 7.564. This designates that a 2.88% accuracy improvement in comparison to the former MLR model, showing slight improvement in precision than the first model, which used all ambient variables. This model encapsulates the effect of most weather conditions by summarizing their effects through T_{pv}, demonstrating that module temperature has a negative influence on power production. Specifically, holding other parameters constant, a 1.27 $°C$ increase in module temperature leads to a 1 W decrease in power output, while an increase of about 0.2 W/m^2 in solar radiation increases the power output by 1 W. Though expressive and slightly more accurate, this model's linear form limits its ability to capture the system's nonlinearity.

An analysis of model statistics, residual scatter plots, and variable variance reveals that both input variables exhibit a nonlinear trend, particularly with respect to the scatter pattern of solar radiation (G) and module temperature (T_{pv}), suggesting a power-law relationship. To balance variable magnitudes and enhance predictive accuracy, each variable is normalized by a constant. The resulting nonlinear equation associating the power generation with solar radiation and operating temperature thus takes the Power-Law (PL) form, denoted in Eq. (IV.4) as follows:

$$\mathrm{P_{pv}} = \left(\frac{\mathrm{aG}}{\mathrm{G_{ref}}}\left(\frac{\mathrm{T_{pv}}}{\overline{\mathrm{T}}}\right)^{\mathrm{b}}\right)^{\mathrm{c}} \tag{IV.4}$$

In this model $\mathrm{G_{ref}}$ and $\overline{\mathrm{T}}$ represent the reference solar radiation (1000 W/m²) and the daily average temperature of the module (°C), respectively. The coefficients $a = 19.858$, $b = -0.109$, and $c = 1.880$ were obtained through iterative procedures. Statistically, the model demonstrates strong predictive capability with an R^2 of 0.9962, an adjusted R^2 of 0.9961, and a predicted R^2 of 0.996. The standard error for this Power-Law prediction is low, at 2.574, which is only 8.37% error than the more complex nonlinear Rational-Power-Law (RPL) model that considers all climatic parameters inputs, showing this simpler model's efficiency and accuracy.

In summary, both the Rational-Power-Law model using all parameters and the Power-Law model with only solar radiation and operating temperature of the module as inputs, prove significantly higher precision compared to linear models, particularly at low solar radiation values in the morning and evening. Figure IV.11 illustrates a comparative view of each model's performance over forecasting days, confirming that the nonlinear models (RPL and PL) achieve results close to those from the ANN model, whereas MLR models fall short in capturing prediction nonlinearity, with considerably larger errors when compared with experimental data.

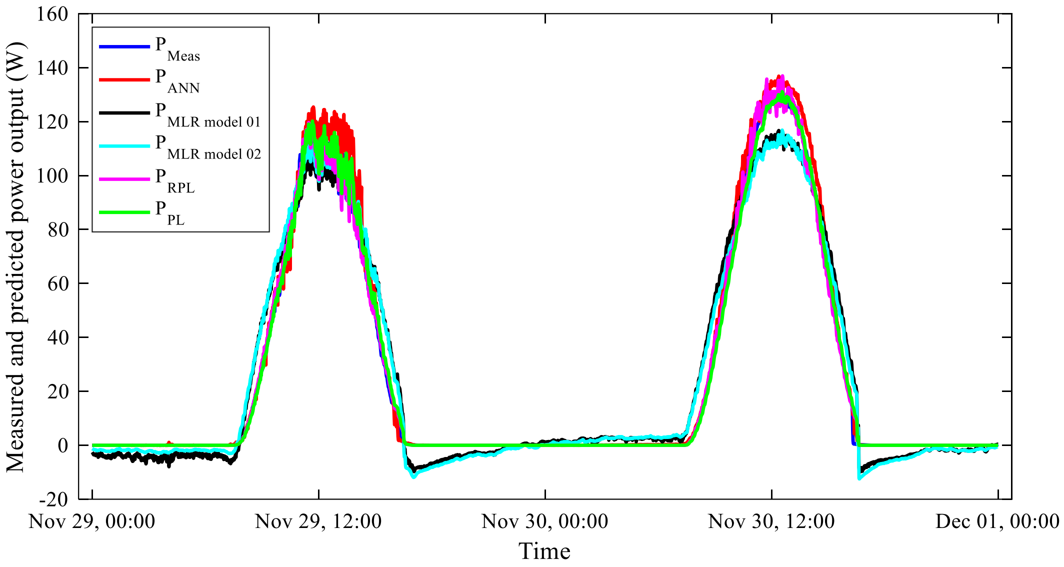

Figure IV.11: Comparison of prediction results from various models, including ANN, MLR models 01 and 02, RPL and PL models, against the actual power output.

IV.2.6 Comparison with existing models in literature

To evaluate the performance of the models developed in this work, various estimating models for predicting PV module power output from literature [29, 198, 199] were compared with the models provided in this work, including the ANN model and Eqs. (IV.1), (IV.2), (IV.3), and (IV.4)). For this comparison, distinct datasets were utilized, with weather data and module's power output recorded on December 1 and December 4, 2022, which represented partially cloudy and sunny conditions, respectively. These datasets provided a solid basis for testing the predictive capabilities of all considered models. Those models' equations from literature, designated as M 01, M 02, and M 03, are provided in Eqs. (IV.5), (IV.6), and (IV.7), respectively:

$$P_{pv} = \frac{G}{G_{ref}} P_{ref}(1 + \mu_p(T_{pv} - T_{ref})) \tag{IV.5}$$

$$P_{pv} = A(0.128G - 0.239 \times 10^{-3} T_a) \tag{IV.6}$$

$$P_{pv} = \eta_{ref} AG(\tau\alpha)(1 - \beta_{ref}(T_{pv} - T_{ref})) \tag{IV.7}$$

where G and G_{ref} denote the measured and reference solar radiation value, T_{pv} and T_{ref} represent the operating and reference temperatures of the module, whereas P_{pv} and P_{ref} are the measured and reference (maximum) electric power output of the module.

The prediction findings from all considered models are illustrated in Figure IV.12 (a) and (b). The graph clearly indicates that the highest precision in forecasting the electrical power output is achieved with the ANN model and both Power-Law models (RPL and PL) developed in this study (Eq. (IV.2) and Eq. (IV.4)) from this work. Following these, the MLR models (Eq. (IV.1) and Eq. (IV.3)) exhibit a good level of performance; however, they tend to overestimate predictions during the morning and afternoon hours while underestimating them for the remainder of the day. In contrast, model M 01 demonstrates significant overestimation during the early and late hours of the day, while equations M 02 and M 03 also exhibit substantial prediction errors throughout their estimations.

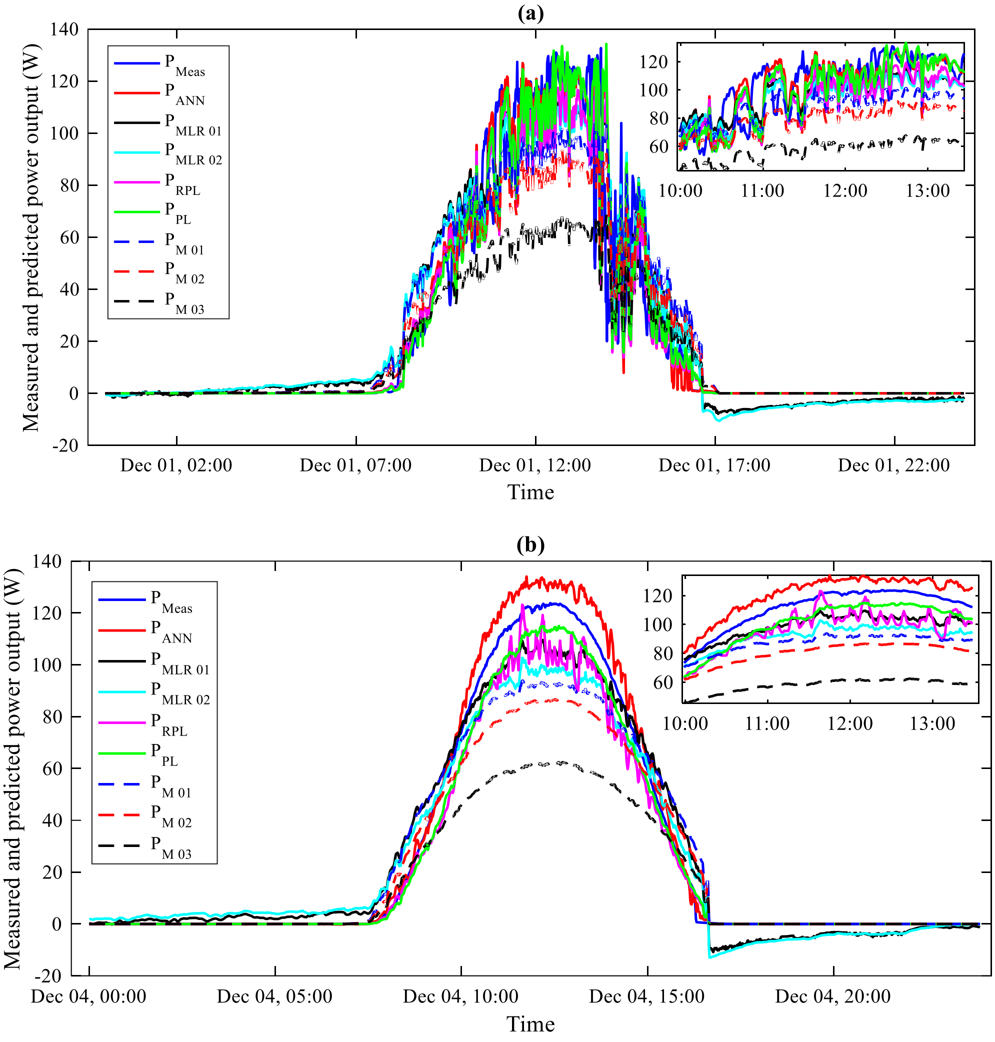

Figure IV.12: Comparison of models’ results versus measured data: (a) for cloudy day and (b) for sunny day.

Table IV.3 below presents the evaluation of predicted against experimental results using various statistical metrics. The findings indicate that the ANN model achieved optimal performance, followed closely by the suggested Power-Law (PL) and Rational-Power-Law (RPL) models developed in this study. These models recorded high coefficients of determination, with the ANN model reaching 0.9159, while the PL and RPL models achieved values of 0.9128 and 0.9120, respectively, during the cloudy day scenario. In terms of error indicators, these models also performed well, achieving similar values for MAE at 4.570, 4.519, and 4.975; MSE at 137.682, 140.350, and 144.463; and RMSE at 11.733, 11.846, and 12.019, respectively. The MLR models 01 and 02 followed not far behind, with R^2 values of 0.8972 and 0.8840 and RMSE values of 12.866 and 13.603, respectively. Model M 01 and M 02 outperformed M 03, though all three models displayed lower accuracy, characterized by relatively low coefficients of correlation and higher error in comparison to other considered models and measured data. Their primary advantage lies in requiring fewer input variables during implementation.

On sunny days, a similar trend was observed across all models. The R^2 values for the ANN, PL, and RPL models were 0.9985, 0.9982, and 0.9949, respectively, with remarkably low MAE values of 2.461, 2.662, and 3.705. RMSE values for these models were recorded at 4.758, 4.908, and 7.246, respectively, suggesting marginally better performance for the PL model over the RPL model, which underscores the significance of the operating temperature of the module in representing other ambient conditions.

Table IV.3: Assessment of different predictive models compared to measured data under cloudy conditions using error indicators.

Model	MAE	MSE	RMSE	R^2
ANN model	**4.570**	**137.682**	**11.733**	**0.9159**
MLR model 01	8.133	165.553	12.866	0.8972
MLR model 02	8.681	185.062	13.603	0.8840
Rational-Power-Law model	**4.975**	**144.463**	**12.019**	**0.9120**
Power-Law model	**4.519**	**140.350**	**11.846**	**0.9128**
M 01	7.498	193.712	13.918	0.8829
M 02	7.270	209.395	14.470	0.8989
M 03	9.970	449.970	21.212	0.8906

IV.3 Module temperature prediction

IV.3.1 Data-driven modeling

Within the context of present study, local climatic parameters and the module operating temperature were utilized to train various machine learning (ML) and regression algorithms with the objective of predicting the back-side temperature of the photovoltaic module and subsequently its power generation. The dataset, spanning ten (10) days, was employed to train, cross-validate, and test the different machine learning algorithms employed in this research. Following a data preparation phase that included feature selection and engineering, 70% of the dataset was allocated to train and validate the models, while the remaining 30% was reserved for forecasting purposes. The prediction of T_{pv} involved not only simple multiple linear regression and least squares regression but also other linear regularized regression techniques such as Ridge regression, LASSO, and Elastic Net. Additionally, non-linear, tree-based, kernel-based, and probabilistic machine learning algorithms were applied, including artificial neural networks (ANN), Random Forest Regression, Support Vector Regression (SVR), and Gaussian Process Regression. The next section will provide an in-depth overview and discussion of the results achieved in this study.

IV.3.1.1 Data preprocessing

In this study, a comprehensive dataset was gathered over a ten-day period from December 23, 2022, to January 1, 2023. Measurements were taken at three-second intervals, resulting in 28,800 samples for each attribute daily. As illustrated in Figure IV.13, the entire dataset was partitioned into two main subsets: 70% for training and validation, and 30% for forecasting. The 70% subset consisted of data collected from December 23 to 29 and was more split into training (80%), cross-validation (10%), and testing (10%) sets. Meanwhile, the 30% subset included data from December 30, 2022, to January 1, 2023, which was reserved for forecasting the temperature of one photovoltaic module.

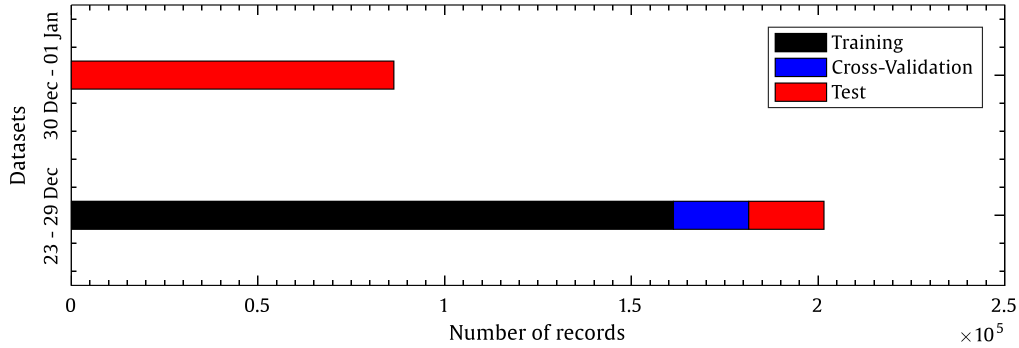

Figure IV.13: Division of the dataset into training, validation, and testing sets.

IV.3.1.2 PCA analysis

In this analysis, as shown in Figure IV.14, ambient temperature, solar radiation, and the operating temperature of the module exhibit high correlations with one another, and also with the second principal component (PC2). In contrast, the above-mentioned variables are exhibits a negative correlation with relative humidity, and weak correlation with PC1. Wind speed demonstrates a correlation with both PC1 and the second principal component (PC2), although the correlation with PC2—and consequently with module temperature—is stronger. Additionally, wind direction displays a strong correlation with PC1 and exhibits high variance, however, it shows an insignificant correlation with the other inputs, suggesting that it should be excluded from the model inputs. Therefore, each model will utilize ambient temperature, solar radiation, wind speed, and relative humidity as inputs, as they demonstrate the highest correlation with the operating temperature of the module, which will be treated as the output.

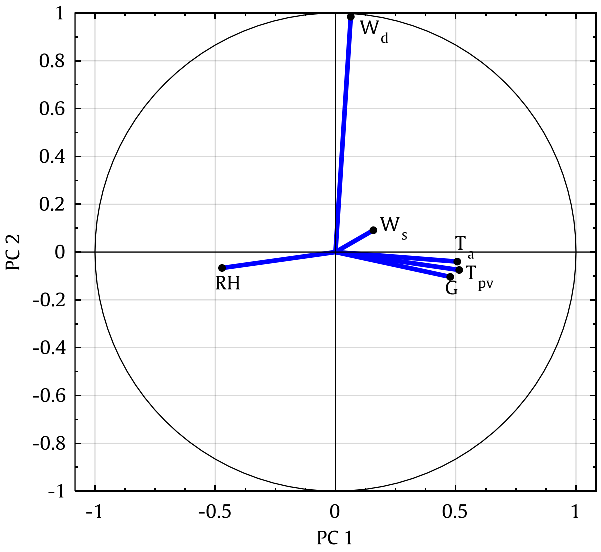

Figure IV.14: Principle component analysis of training data in the form of correlation circle.

The training data from this study is illustrated in Figure IV.15 revealing a similar trend in solar radiation and ambient temperature, both of which increase during the morning, peak at noon, and subsequently decline toward the evening. In contrast, relative humidity exhibits an inverse pattern. Meanwhile, wind speed values show a more erratic behavior, lacking a consistent trend.

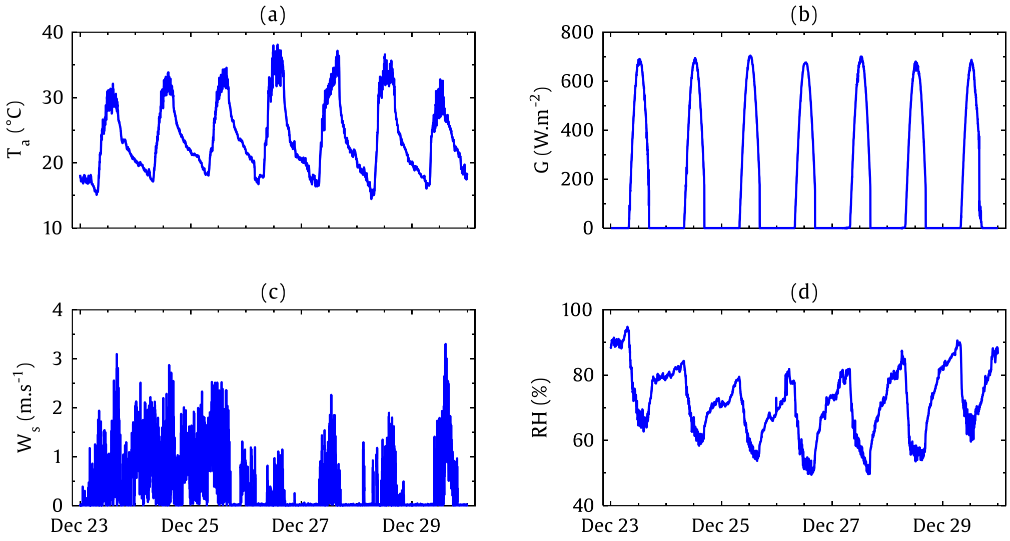

Figure IV.15: Weather data recorded during December 23-29, showing (a) ambient temperature, (b) solar radiation, (c) wind speed, and (d) relative humidity

IV.3.1.3 Linear models

Various linear regression techniques are employed to establish exportable models for predicting PV module temperature. Initially, a Multiple-Linear Regression is conducted, where the loss function $L(x)$ defined as $||Ax - b||_2$, with the goal of minimizing this function through ordinary least squares. Within this approach, all features are considered significant, resulting in a non-zero coefficient for each variable in the resulting equation. The derived model from the regression analysis is expressed in the form of Eq. (IV.8) as follows:

$$T_{pv} = 1.2138\, T_a + 0.027\, G + 0.3359\, W_s + 0.0495\, RH - 10.2595 \qquad \text{(IV.8)}$$

The above-stated equation estimates T_{pv} for the considered inputs from the dataset, achieving an R^2 of 0.977, an adjusted R^2 of 0.974, and a predicted R^2 of 0.971. The Standard Error (SE) of the model is notably low at 2.011, indicating a strong fit. This model indicates that, with all other parameters held constant, an increase in ambient temperature corresponds to a 1.2 °C rise in module operating temperature, a rise of 0.027 W/m² in solar radiation, or a rise of approximately 0.34 m/s in W_s, whereas the influence of RH is fairly minimal in this context.

By incorporating the l_2 penalty term into the regression problem through Ridge regression, the solution of a loss function of the form $L(x) = \|Ax - b\|_2 + \alpha\|x\|_2$ must be established. This approach effectively mitigates the impact of uncertainty and noise in the target variable vector (T_{pv}), regularizes significant fluctuations and discrepancies in x, and addresses multicollinearity among predictors. However, similar to ordinary least squares in the Multiple Linear Regression (MLR) model, Ridge regression keeps assuming that each entry in x is significant and thus treated as influential parameters. The resulting model from this Ridge regression is expressed in Eq. (IV.9):

$$T_{pv} = 0.8933\,Ta + 0.026\,G + 0.5594\,W_s - 0.1136\,RH + 9.1418 \qquad \text{(IV.9)}$$

The Ridge regression model demonstrated slightly lower accuracy compared to the previous MLR model, attaining an R^2 of 0.973, an adjusted R^2 of 0.968 and a predicted R^2 of 0.963. with a Standard Error of 2.233. This represents approximately an 11% decrease in accuracy relative to the MLR model. The coefficients of the model indicate a more balanced distribution of attribute weights and their impacts on T_{pv}. Specifically, the influence of ambient temperature is diminished by 26.4%, while solar radiation's effect is reduced by 3.7%. Conversely, the impact of wind speed has increased by 66%, and a significant decline of 329% is noted for the relative humidity effect.

In contrast, incorporating the l_1 penalty term to regularize the regression and mitigate overfitting through the LASSO algorithm, minimizing a loss function of the form $L(x) = \|Ax - b\|_2 + \lambda\|x\|_1$, yielded the model presented in Eq. (IV.10):

$$T_{pv} = 1.0996\,T_a + 0.0274\,G + 0.2386\,Ws - 4.0129 \qquad \text{(IV.10)}$$

This statistical model demonstrates a distinct approach, as it has penalized the influence of relative humidity, resulting in its coefficient being reduced towards zero. Consequently, the variation in the operating temperature of the module is therefore primarily correlated with ambient air temperature, contributing nearly 1.1 °C for each unit increase in T_{pv}, alongside an increase of 0.0274 W/m² for the same rise in T_{pv}. Wind speed also plays a role, contributing approximately 0.24 m/s. Regarding the model's statistics, it achieved an R^2 of 0.977, an adjusted R^2 of 0.974 and a predicted R^2 of 0.971. With a standard error (SE) of 2.006, it outperforms the MLR model by 0.24% and the Ridge regression model by 10.16%. This performance is quite commendable, as the adjusted R^2 and predicted R^2 values are nearly equivalent to the coefficient of determination(R^2).

By integrating the effects of both Ridge and LASSO algorithms, the Elastic Net algorithm considers a loss function of the form $L(x) = \|Ax - b\|_2 + \lambda\|x\|_1 + \alpha\|x\|_2$ This approach achieves a balance between obtaining a sparse solution and preventing overfitting while also mitigating the impact of multicollinearity within the data. The derived model via this approach is expressed in Eq. (IV.11):

$$T_{pv} = 0.9849\, T_a + 0.0268\, G + 0.4067\, Ws - 0.0592\, RH + 2.886 \tag{IV.11}$$

Leveraging the strengths of both algorithms, this Elastic Net model outperformed the Ridge regression model. It attained an R^2 of 0.975, an adjusted R^2 of 0.971 and a predicted R^2 of 0.968, whereas the Standard Error was 2.104. Compared to other models, this performance is 4.6% and 4.9% lower in accuracy compared to the MLR and LASSO models, respectively, yet 5.77% less error compared to the Ridge regression model. Additionally, while LASSO model demonstrated enhanced results if evaluated by statistical indicators, the inclusion of the relative humidity effect in the Elastic Net model may negatively impact its overall performance due to the relatively high variance associated with this predictor.

A comparison of the measured and predicted module temperatures from the linear models is illustrated in Figure IV.16 for three successive days. All linear models achieved a good level of accuracy in predicting T_{pv}, with results showing similarities across models. Notably, the MLR and LASSO regression models demonstrated slightly higher accuracy. The superior performance of the LASSO model suggests that relative humidity may have a less significant impact on predicting T_{pv} compared to the other parameters.

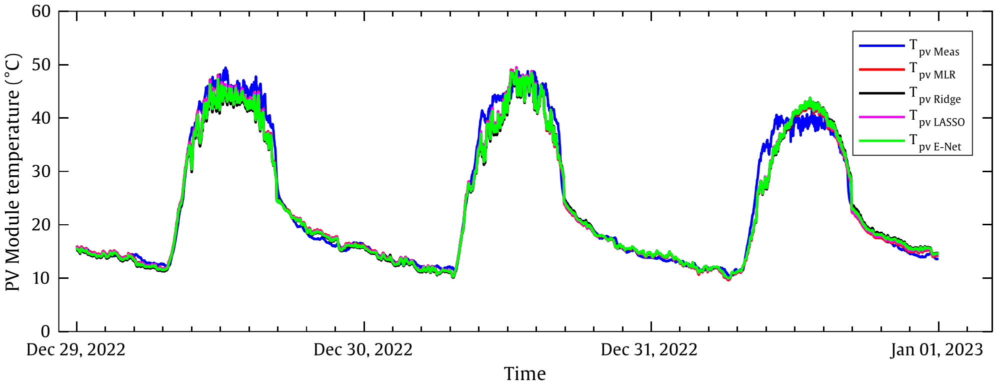

Figure IV.16: Comparison between experimental and estimated module operating temperature using linear models.

Table IV.4 presents an assessment for the predictions of various linear models utilized in this work. As indicated by the coefficient of determination (R^2), more than 97% of the variation in the operating temperature of the module is due to changes in ambient temperature (T_a), solar radiation (G), wind speed (W_s), and relative humidity (RH) demonstrating a reasonable level of accuracy across all models. The MLR and LASSO regression models achieved superior performance, with RMSE values of only 2.01 and 2.005, MAE values of approximately 1.227 and 1.278, and MSE values of 4.042 and 4.022, respectively, along with MAPEs of 4.798% and 4.788%. In contrast, Ridge and Elastic Net regression exhibited slightly higher errors across all statistical indicators and lower R^2 values. Even with the exclusion of RH in the LASSO model, its accurate estimation highlighted the benefits of feature selection and regularization in preventing overfitting during predictive modeling. Additionally, the l_1 norm encourages sparsity, resulting in models that are more robust against outliers.

Table IV.4: Statistical assessment of various models compared to measured values.

	R^2	$RMSE$	MAE	MSE	$MAPE$ (%)
MLR model	0.977	2.01	1.227	4.042	4.798
Ridge model	0.973	2.232	1.460	4.983	5.463
LASSO model	0.977	2.005	1.278	4.022	4.788
Elastic Net model	0.975	2.103	1.341	4.422	5.014

IV.3.1.4 Tree-Based models

This section adopts a different approach to predict module temperature using three distinct tree-based models. Initially, a decision tree model is developed, with training, tuning, and cross-validation using 80% of the training data and 10% for validation, leaving the remaining 10% for testing. The optimal decision tree model was identified with a maximum of 25 splits and 51 nodes, yielding the minimal cross-validation mean squared error (MSE) of 2.09 and a test error of 1.806. This model is subsequently utilized for predicting T_{pv}. The second tree-based model employed is a random forest, which functions as an ensemble of decision trees. It was determined that a random forest model with 98 trees achieved optimal performance, resulting in cross-validation and testing MSEs of 0.4452 and 0.2299, respectively. The final model in this category is the gradient boosting algorithm, which also utilizes decision trees as base models. For this model, 600 decision trees were integrated to enhance performance, producing cross-validation and testing MSEs of 1.177 and 1.0188, respectively. These models were then applied to predict T_{pv} during the testing days. Figure IV.17, compares the outcomes of all tree-based models with measured data. The decision tree model exhibits limited flexibility, often averaging temperatures to a uniform value during prolonged durations. However, substantial improvements are observed with the random forest model, where predictions are derived from 98 decision trees, and further enhancements are achieved with the gradient boosting model, which employs a total of 600 trees to estimate module temperature effectively.

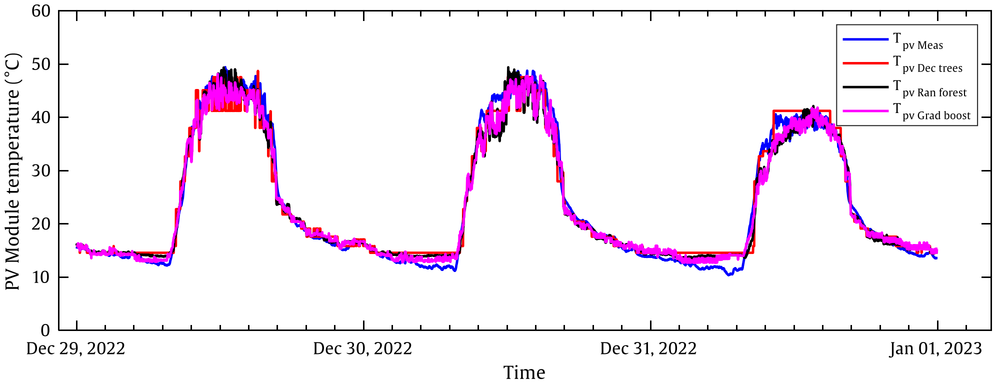

Figure IV.17: Comparison between experimental and estimated module temperatures using tree-based models.

The performance of each model was evaluated statistically using various metrics, as outlined in Table IV.5. The decision tree model demonstrated a coefficient of determination (R^2) of 0.968, explaining 96.8% of the variance in T_{pv} based on the input parameters of ambient temperature (T_a), solar radiation (G), wind speed (Ws), and relative humidity (RH). It achieved prediction errors with RMSE, MAE, and MSE values of 2.365, 1.758, and 5.595, respectively, resulting in a reasonable level of precision, reflected by a mean absolute percentage error (MAPE) of 8.49%. The standard error (SE) for the prediction of the decision tree model was 2.366, which is 13.3% more than the standard error normally observed in linear models. In contrast, the ensemble models (random forest and gradient boosting) exhibited an enhanced accuracy, providing higher R^2 values, nearly 0.98, alongside less prediction errors. The gradient boosting model showed a slight advantage, achieving a standard error of 1.945 compared to 2.001 for the random forest model. Additionally, the adjusted R^2 and predicted R^2 values for both models were 0.974 and 0.969 for the random forest, and 0.975 and 0.971 for the gradient boosting model, indicating enhanced predictive capabilities for the latter. The gradient boosting model's superior performance can be attributed to its iterative nature, which continuously aims to minimize predictive error by adding weak learners, thereby improving accuracy and enhancing overall predictive power. This characteristic highlights the effectiveness of gradient boosting in capturing complex patterns within the data.

Table IV.5: An assessment of various tree-based models compared to measured data for module temperature prediction.

	R^2	$RMSE$	MAE	MSE	$MAPE$ (%)
Decision trees model	0.968	2.309	1.694	5.331	8.260
Random forest model	0.978	2.004	1.451	4.017	6.885
Gradient boost model	0.982	1.925	1.340	3.706	5.932

IV.3.1.5 Kernel methods

Support Vector Regression (SVR) and Kernel Ridge Regression (KRR) are kernel-based machine learning algorithms utilized in this study to predict the operating temperature of the module and model its relation with the considered parameters, including solar radiation, ambient air temperature, relative humidity, and wind speed. The optimal models from both algorithms were selected after conducting cross-validation, where 80% of the data was used for training and 10% for validation, leaving the remaining 10% for testing. The SVR model was trained using the Sequential Minimal Optimization (SMO) algorithm with a linear kernel function, allowing it to identify a hyperplane that fits the data the best. In contrast, the KRR model employed a polynomial kernel function, enabling it to account for non-linear patterns and interactions among the inputs that may be represented as polynomial functions. The operating temperature of the module predictions from both SVR and KRR were evaluated against measured data, as shown in Figure IV.18. The figure demonstrates that both models achieved highly accurate predictions, with the KRR model yielding slightly more accurate predictions. This performance suggests that the polynomial kernel of KRR effectively captures the complex relationships between input features and module temperature, thereby enhancing the model's predictive capability.

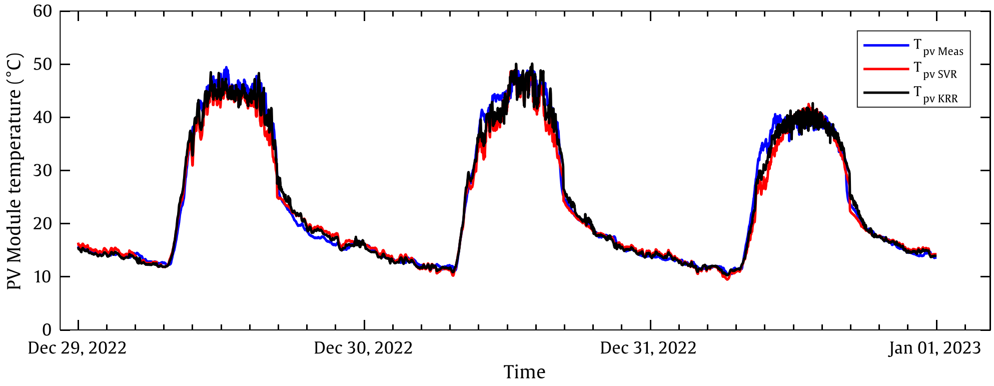

Figure IV.18: Comparison of experimental vs. estimated module temperatures using Support Vector Regression (SVR) and Kernel Ridge Regression (KRR).

The quantitative analysis of the models further confirms the superior performance of the kernel-based algorithms, particularly the Kernel Ridge Regression (KRR) model, which outperformed all aforementioned approaches. The KRR achieved a coefficient of determination of 0.985, along with an adjusted R^2 of 0.984 and a predicted R^2 of 0.984. These metrics underscore the high accuracy and predictive power of the model. In terms of error metrics, KRR produced a Root Mean Squared Error (RMSE) of 1.55, a Mean Squared Error (MSE) of 2.402, and a Mean Absolute Error (MAE) of only 1.041, all of which are significantly low. Additionally, the Mean Absolute Percentage Error (MAPE) for the KRR model was 4.081%, demonstrating its strong estimation accuracy and overall performance. On the other hand, the Support Vector Regression (SVR) model demonstrated somewhat lower accuracy R^2 values of 0.977, an adjusted R^2 of 0.972 and a predicted R^2 of 0.968 While these results are yet quite accurate, they fall a bit short compared to the performance of the KRR model. The error metrics for the SVR model included an RMSE of 2.064, an MSE of 4.262, and an MAE of 1.321, resulting in a MAPE of 5.061%, which is approximately 1% higher than that of the KRR model. Figure IV.19 illustrates that the predicted versus measured data points for the KRR model are well-clustered around the perfect regression line, indicating its strong predictive capability compared to the SVR model, which had a standard error (SE) of 2.065, in contrast to the KRR's SE of 1.55. This visual representation reinforces the conclusion that KRR provides more accurate predictions of module temperature.

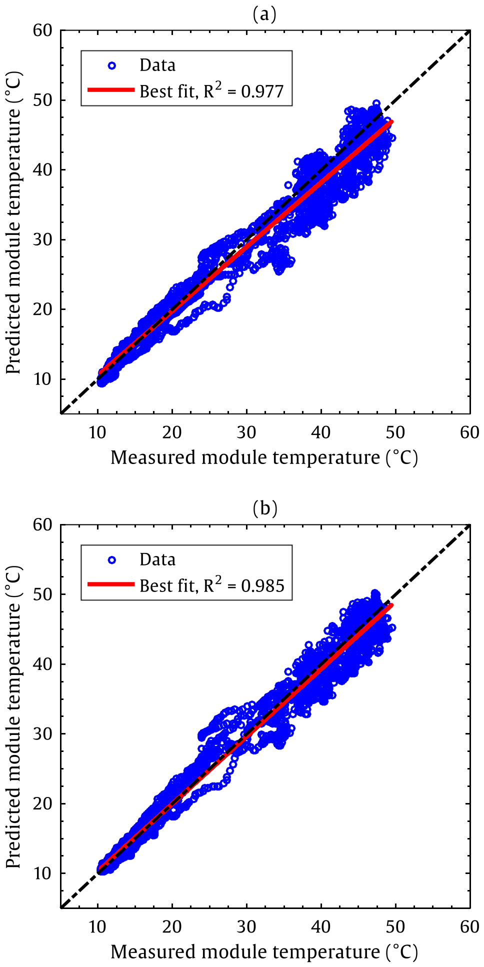

Figure IV.19: Scatter plots of experimental vs. estimated module temperatures for, (a) SVR model and (b) KRR model.

IV.3.1.6 Artificial Neural Network model

The ANN model designed for predicting module temperature demonstrated robust performance after an extensive hyperparameter tuning phase. The final model architecture comprises three hidden layers with 4, 3, and 2 neurons, respectively, utilizing the hyperbolic tangent activation function. After testing multiple training algorithms, the Levenberg-Marquardt algorithm was selected as it delivered the lowest errors and highest coefficient of determination. For inputs, the model used ambient temperature (T_a), solar radiation (G), wind speed (W_s), and relative humidity (RH), while the module temperature (T_{pv}) was the target variable. During training, the model showed strong predictive accuracy, achieving convergence with a mean squared error (MSE) of 0.0064 and a coefficient of determination (R^2) of 0.993 by epoch 195, as shown in Figure IV.20. This high level of accuracy indicates that the ANN model is well-suited for capturing the complex, nonlinear relationships between the input variables and the module temperature.

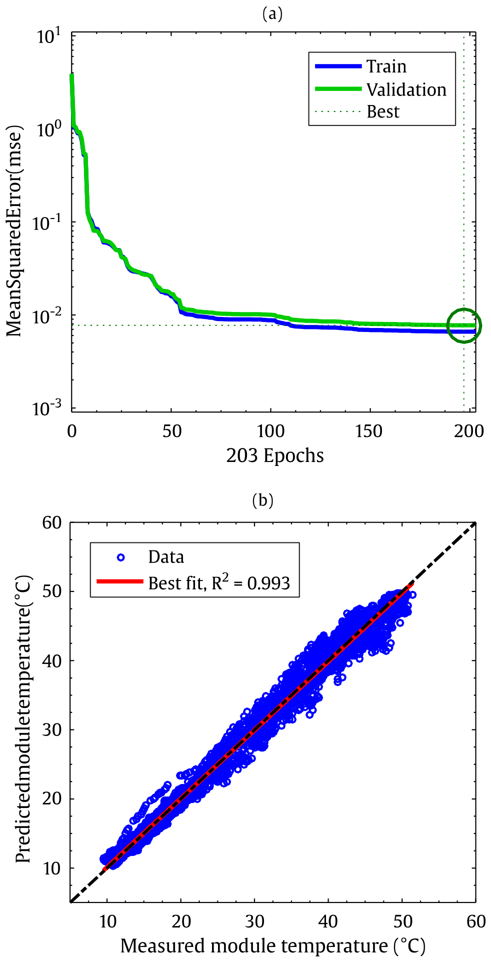

Figure IV.20: (a) The performance ANN model's training phase, and (b) estimated versus experimental module temperature scatter plot.

Upon introducing the forecasting dataset to the trained and validated ANN model, it demonstrated impressive predictive capability in estimating the module temperature. As it is evident in Figure IV.21, the discrepancies between measured and predicted module temperatures are minimal, highlighting the accuracy of the ANN model.

The model's success in accurately forecasting T_{pv} can be attributed to its ability to capture the complex nonlinear relationships within the PV system. This includes the dynamics influenced by various heat transfer mechanisms, such as conduction, convection, and radiation, which occur during the heat exchanges between the module and its surroundings. The ANN's proficiency in handling these intricate interactions allows it to make highly reliable predictions, confirming its suitability for PV temperature forecasting tasks.

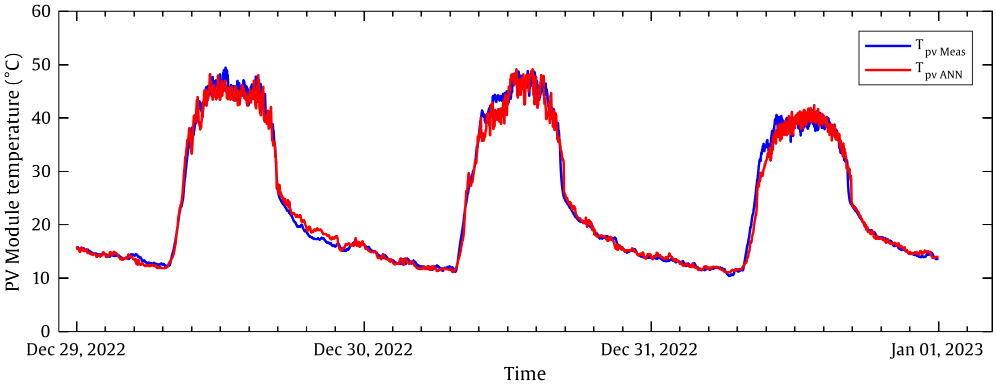

Figure IV.21: Comparison of the experimental and measured operating temperature of the module obtained from the ANN model.

Statistical analysis further validates the highly accurate results of the ANN model in predicting module temperature (T_{pv}). The model attained an impressive coefficient of determination (R^2) of 0.986, indicating that it explains 98.6% of the variance in T_{pv} based on the input variables (solar radiation, ambient air temperature, wind speed, and relative humidity). Error metrics reinforce this, with very low values across all indicators: RMSE of 1.477, MAE of 0.982, and MSE of 2.181, and a MAPE of only 3.88%. These values reflect a level of precision that surpasses all other models implemented, confirming the ANN's superior predictive accuracy. Additionally, Figure IV.22 further emphasizes the model's performance with scatter plots comparing predicted and measured module temperatures, where most data points align closely with the 45-degree line representing ideal predictions. The residuals plot shows that only 11% of errors exceed 2.5°C, and the model achieved a standard error of just 1.477. The adjusted R^2 of 0.986 and predicted R^2 of 0.985 also imply that the ANN model would maintain its accuracy on unseen data, suggesting strong generalization and robustness in predicting module temperature based on given environmental conditions.

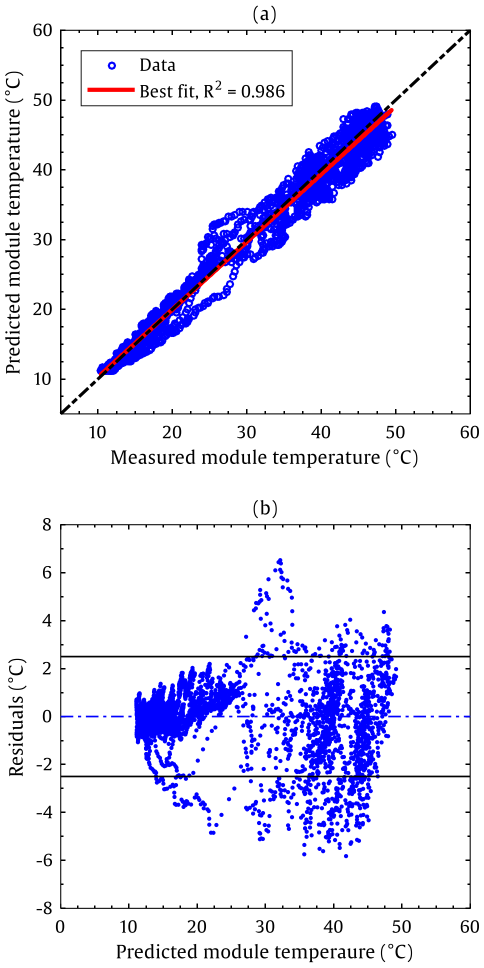

Figure IV.22: Scatter plot displaying the predicted module temperature versus measured values from the ANN model (a), along with (b) prediction residuals.

IV.3.1.7 Probabilistic model

Gaussian Process Regression (GPR) offers valuable insights into complex, non-linear relationships between the module temperature (T_{pv}) and environmental factors, such as ambient temperature, solar radiation, wind speed, and relative humidity. The model uses a Squared Exponential kernel, allowing it to capture intricate interactions and produce smooth predictions Figure IV.23, illustrates the predictive performance of the GPR model, which successfully learns the underlying relations and dynamics influencing T_{pv}. During training, the GPR model achieved a cross-validated MSE of 0.152, highlighting its accuracy. However, as a probabilistic method that treats T_{pv} as a distribution over possible functions, the GPR model naturally exhibits some uncertainty, especially in periods where outliers or abrupt changes affect predictions. This sensitivity to anomalies can introduce uncertainty intervals, which is visually evident in the figure. Despite this, the GPR model remains effective, balancing linear and non-linear dependencies within the dataset and offering a nuanced perspective on the behavior of module temperature.

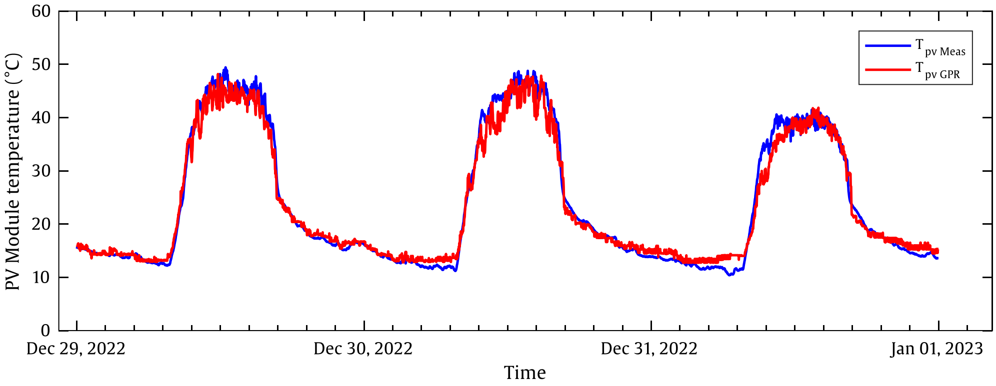

Figure IV.23: Comparison of the measured and predicted module temperature utilizing the Gaussian Process Regression (GPR) model.

The scatter plot in Figure IV.24 for predicted versus experimental module operating temperature (T_{pv}) demonstrates the accuracy and reliability of the Gaussian Process Regression (GPR) model, with the data points falling within a satisfactory range of error. Statistically, the model achieves a Standard Error (SE) of 2.066, indicating a relatively low prediction variance.

The GPR model's performance is further validated by several error metrics: it achieved a Mean Absolute Error (MAE) of 1.405, a Mean Squared Error (MSE) of 4.265, and a Root Mean Squared Error (RMSE) of 2.065. The coefficient of determination (R^2) was 0.977, signifying that nearly 98% of the variance in T_{pv} is described by the input parameters, such as ambient temperature, solar radiation, wind speed, and relative humidity.

Additionally, the adjusted R^2 and predicted R^2 values of 0.972 and 0.968, respectively, confirm the GPR model's robustness and its predictive power, even for unseen datasets. This model's performance underscores its capability to accurately predict module temperature and manage both linear and non-linear relationships within the data.

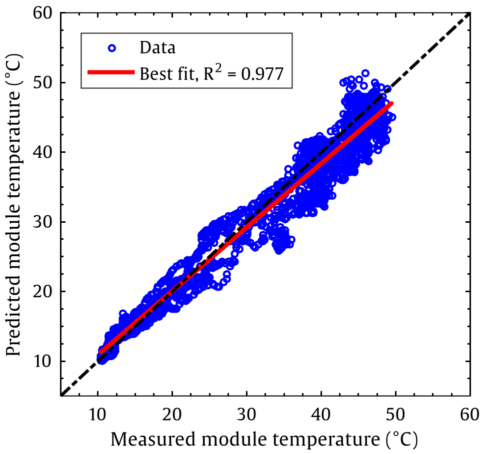

Figure IV.24: Scatter plot comparing the measured module temperature with the predicted values obtained from the GPR model.

IV.3.1.8 Proposed Non-linear model

Focusing on building an exportable model for the prediction of photovoltaic module operating temperature, that is reliable, efficient, interpretable, and easy to implement, the results obtained from all tested ML algorithms and their analysis were consider. In addition to, not only the comprehension of the problem and the fundamentals of heat transfer mechanisms occurring between the photovoltaic module and its environment, but also by closely inspecting residuals and variances between input parameters, as illustrated in Figure IV.25, for the MLR model, it becomes evident that residuals display an abnormal distribution across the ranges of T_a, and W_s, Furthermore, a non-linear trend in residuals versus solar radiation is also observed. Similar patterns are evident in other linear models, such as LASSO and Ridge regression, indicating limitations in accurately modeling the complex dynamics.

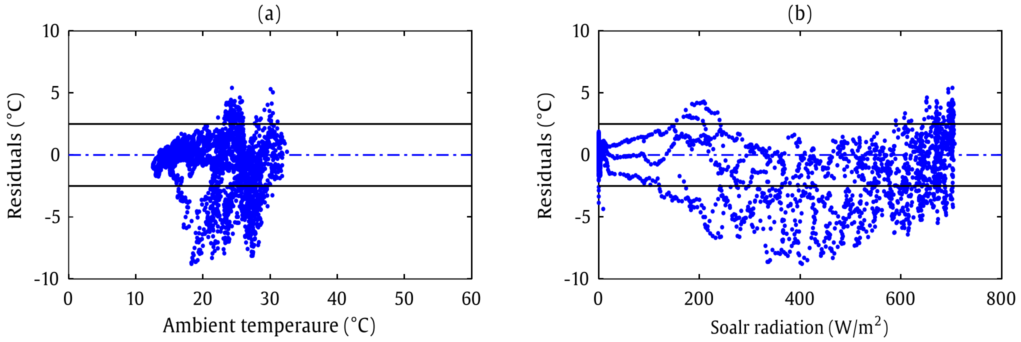

Figure IV.25: Scatter plots illustrating the residuals in relation to the predictors: (a) ambient temperature and (b) solar radiation.

Therefore, a non-linear regression equation is introduced, utilizing T_a, G, and W_s, as inputs, with the goal of predicting T_{pv}. It is important to note that relative humidity is excluded from the non-linear model, implicitly grounded on the variable selection outcomes obtained through the LASSO algorithm. In this suggested model, T_a is scaled by with a constant parameter to regulate its influence on the operating temperature of the module. In contrast, solar radiation is raised to a constant power parameter to capture its power-law tendency, whereas wind speed is positioned in the denominator, reflecting its negative impact on the module temperature. The formulated model is represented as follows in Eq. (IV.12):

$$T_{pv} = aT_a + \frac{bG^c}{e^{dW_s}} \tag{IV.12}$$

The coefficients in the above equation are derived iteratively by implementing a least squares loss function, yielding the following values: $a = 0.912$, $b = 0.159$, $c = 0.743$, and $d = 0.01$. This model indicates that the output variable (T_{pv}) is linearly correlated with the ambient air temperature T_a which is multiplied by a constant parameter of 0.912. This implies that, while keeping other variables constant, an increase of approximately 0.9°C in T_a would result in a 1°C rise in the module temperature. Conversely, the relationship between the module temperature and solar radiation is characterized as a power-law, where both the constant power and scaling coefficient determine how sensitively changes in G impact T_{pv}. The divisor of the second term features an exponential function in W_s, introducing the non-linear nature of wind speed to the model and causing the dependent variable (T_{pv}) to decline swiftly as wind speed increases—consistent with expectations from heat transfer analysis—. Figure IV.26. illustrates the comparison of predicted module temperature with experimental values. Despite relying on just three input parameters, namely, T_a, G, and W_s. the model demonstrates a reasonable level of accuracy, effectively fitting the data and capturing the relationship between the input features and the target variable T_{pv}.

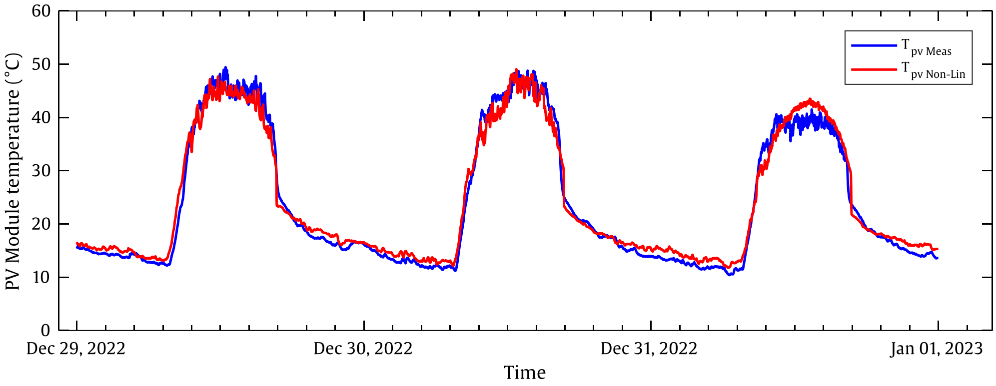

Figure IV.26: Comparison of experimental and estimated operating temperature of the module utilizing the proposed non-linear model.

To further evaluate the proposed model's performance, a comprehensive analysis of its forecasts versus measured data was conducted, revealing reasonable prediction errors that effectively account for variations in the output variable based on the considered inputs. Particularly, the model accounts for 98.1% of the entire variance in T_{pv}, demonstrating a strong agreement with experimental measurements. The adjusted R^2 was calculated to be 0.977, slightly lower than the R^2 (0.981) indicating satisfactory model performance. This suggests that incorporating additional input variables, such as relative humidity (RH), may not yield significant improvements in explained variance or predictive power, particularly when considering the overfitting risk by the model. Furthermore, the predicted R^2 was found to be 0.975, suggesting that on unseen datasets, the model is more likely to perform well.

Statistically, the prediction residuals for the model were plotted versus T_a and G in Figure IV.27 (a) and (b), respectively. The plots reveal a more even residuals distribution throughout the range of inputs, more uniformly concentrated around zero. Notably, only 14% of the residuals exceed 2.5°C, that is just 3% higher compared to the ANN model. Additionally, the model's standard error (SE) was recorded at 1.862, while the root mean squared error (RMSE) of its predictions stood at 1.861. The mean absolute error (MAE) and mean square error (MSE) also indicated a good model fit, with values of 1.476 and 3.464, respectively. The mean absolute percentage error (MAPE) was well below 10%, at 7.015%, reflecting remarkable prediction accuracy and a close alignment with the experimental data. Overall, these results underscore the solid performance, reliability, and suitability of the model for practical real-world applications.

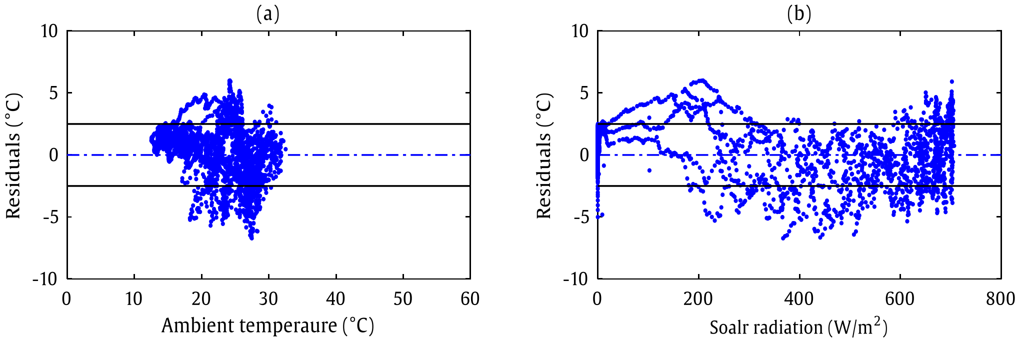

Figure IV.27: Residual plots of predicted module operating temperature obtained from the proposed model.

IV.3.1.9 Comparative analysis with counterpart models

To facilitate a comparison with models from the literature and assess the robustness and generalizability of the proposed model, several equations for estimating module temperature were selected. An additional dataset was utilized for this purpose, specifically for out-of-sample testing. The dataset included measurements for the operating temperature of the module, and other weather parameter, and the power output of the photovoltaic module, collected on January 2 and January 3, 2023. These particular days were chosen as they provided suitable conditions for validation the models developed in this study; January 2 was partially cloudy, while January 3 was sunny.

In Figure IV.28. the experimentally measured module temperature is compared with predictions from the proposed model (T_{prop}) and various models from the literature, as detailed in Table I.3. The results reveal varying performance among the models in estimating T_{pv}. Notably, all models generally perform well during periods of low to no solar radiation. However, Bailek and Ross models exhibit contrasting behaviors, with Bailek's model underestimating T_{pv} and Ross's model overestimating it.

During daylight hours, Skoplaki's model appears to overfit the experimental data, failing to generalize adequately. In contrast, the model suggested in this study and the model by King, both demonstrate strong performance, a close fit with measured data and accurately account for the underlying patterns. The results indicate some advantage for the model suggested in this study, showcasing its effectiveness in predicting module temperature under varying environmental conditions.

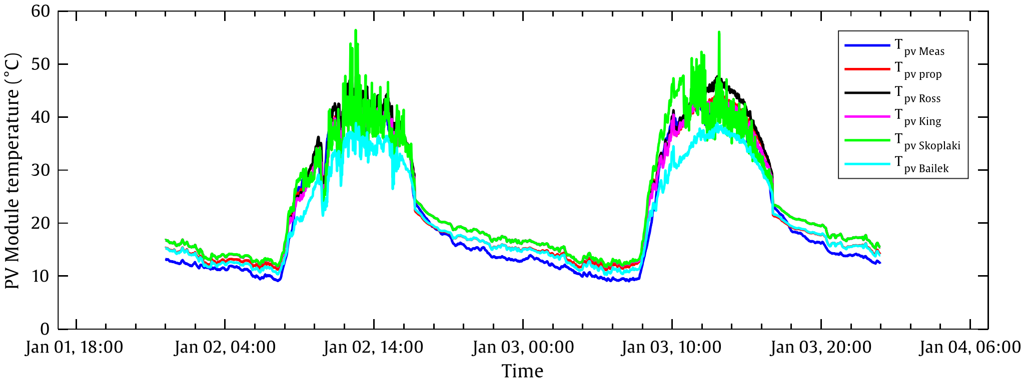

Figure IV.28: Comparison of measured operating temperature of the module T_{pv} as predicted by the suggested model against counterpart models.

For the statistical comparison of predictions made by each model Figure IV.29. displays the histogram of residuals for all tested models. The histogram reveals that the residuals from the proposed model closely align with a normal distribution, as evidenced by their narrow range and symmetrical centering around zero. In contrast, the other models exhibit skewness and a wider distribution of residuals. This suggests that the proposed model is more effectively capturing the underlying behavior and overall trend of the data, leading to consistently well-aligned predictions with the real values. To underscore this point, the predictive error for all models was evaluated. The suggested model demonstrates a general advantage, achieving an R^2 value of 0.983, a Mean Absolute Error (MAE) of 1.819, a Mean Squared Error (MSE) of 4.42, and a Root Mean Squared Error (RMSE) of 2.102. Additionally, the adjusted and predicted R^2 values for the proposed model were 0.967 and 0.964, respectively.

For comparison purposes, King's model also explains 0.983 of the variance in T_{pv}, analogous to the proposed model. However, King's model has lower adjusted and predicted R^2 values of 0.944 and 0.933, respectively. Furthermore, King's model reported higher error rates, with an RMSE of 2.720, a MAE of 2.442, and an MSE of 7.397, which contributes to the biased residuals' distribution illustrated in Figure IV.29. It is important to note that the Mean Absolute Percentage Error (MAPE) for the proposed model is 11.545%, while for King's model, it is significantly higher at 16.657%. The Standard Errors (SE) for the suggested and King's models were found to be 2.104 and 2.722, respectively. An overview of the performance for the similarly tested models from the literature can be found in Table IV.6.

Table IV.6: Statistical assessment of various models from the literature compared to measured data.

	R^2	$Adjus\ R^2$	$Pred\ R^2$	$RMSE$	MAE	MSE	$MAPE$ (%)
Ross model	0.980	0.927	0.928	3.115	2.857	9.704	17.793
Skoplaki model	0.960	0.919	0.909	3.278	2.916	10.746	18.224
Bailek model	0.977	0.920	0.861	3.266	2.549	10.665	11.853

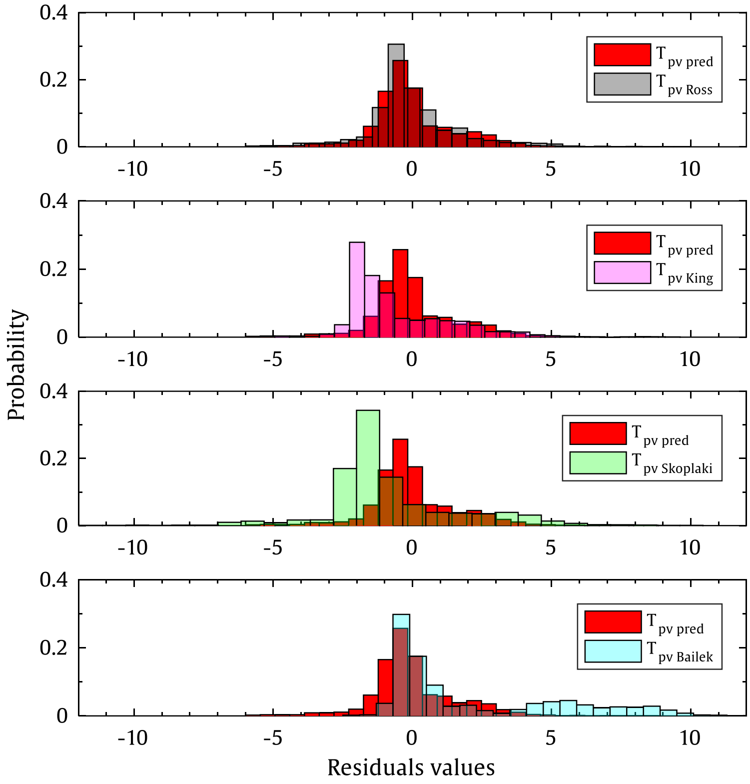

Figure IV.29: Histogram of residuals for the proposed model in comparison to corresponding models from the literature.

IV.3.1.10 Power output prediction

To provide a comprehensive understanding of this research, this section explores the performance of the proposed model in estimating the power output of PV modules, which is intrinsically linked to their temperature. Once the operating temperature of the module is determined, the produced power output of that module may be predicted via the established equations. The power generation of a PV module primarily depends on its temperature, as well as solar radiation levels. Additionally, the investigations into the operating temperature of the photovoltaic module can be expanded to applications such as water heating in photovoltaic/thermal systems or selecting appropriate fluids for the cooling of PV systems.

Now, the motivation is specifically on estimating the power output of the module. The power output of the photovoltaic module was logged on January 2 and 3, 2023. The measured power output (P_{pv}) from the module is assessed against the power output predicted based on the module's operating temperature equation suggested in this work, as expressed in (Eq. (IV.12)). For comparison, the power output prediction model utilized is a recent model equation developed by Keddouda et al. [25], which estimates the power output based on both solar radiation and module temperature. The equations representing these models can be outlined as follows:

$$P_{pv} = \left(\frac{19.858\, G}{G_{ref}} \left(\frac{T_{pv}}{\bar{T}} \right)^{-0.109} \right)^{1.88} \tag{IV.13}$$

where G_{ref} signifies the reference value of G ($1000\ \mathrm{W/m^2}$) and $\bar{T}$ denotes the mean daily module temperature. The results of the experimentally measured versus predicted module power output are presented in Figure IV.30. While a slight more error rate is noted for the cloudy day, the overall accuracy remains commendable, underscoring both the reliability of temperature predictions made by the proposed model and the effectiveness of the photovoltaic power output model. Particularly, the power output is predicted with a R^2 of 0.937 and a RMSE of 10.374. On the average, the variation among the estimated and experimental P_{pv} was merely 3.470, with a Standard Error of 10.383, signifying a strong and good fit by the model and precise operating module temperature estimation. Additionally, the adjusted and predicted R^2 values for the power output estimates were 0.937 and 0.936, respectively, demonstrating a low likelihood of overfitting and reinforcing the robustness of the results yielded by the models.

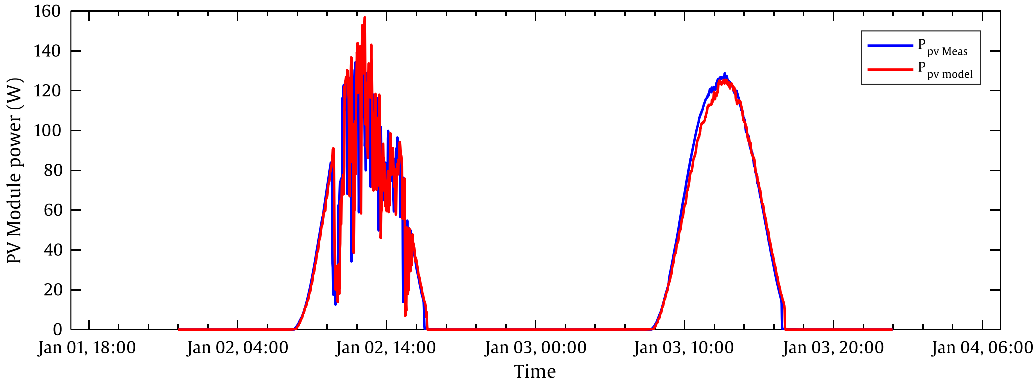

Figure IV.30: Measured versus predicted module power generation based on the proposed temperature model.

IV.3.2 Numerical simulations

In this section, the operating temperature of a stand-alone photovoltaic module (of the type polycrystalline silicon) is being predicted using computational fluid dynamics (CFD) simulations, which may to be used to calculate the power output of the module. Additionally, a separate parametric study investigates the influences of various variables affecting the module’s performance. For these numerical simulations, experimental data were collected, recording ambient temperature (T_a), solar radiation (G) and wind speed (W_s) on December 25, 2022 (sunrise at 07:32 and sunset at 17:30), and January 02, 2023 (sunrise at 07:34 and sunset at 17:35). For instance, Figure IV.31 presents the experimental data for these two days. The environmental conditions during this period demonstrate a typical trend, with solar radiation and ambient temperature increasing from morning to noon and then declining in the afternoon and evening. In contrast, the W_s values exhibit a more erratic pattern.

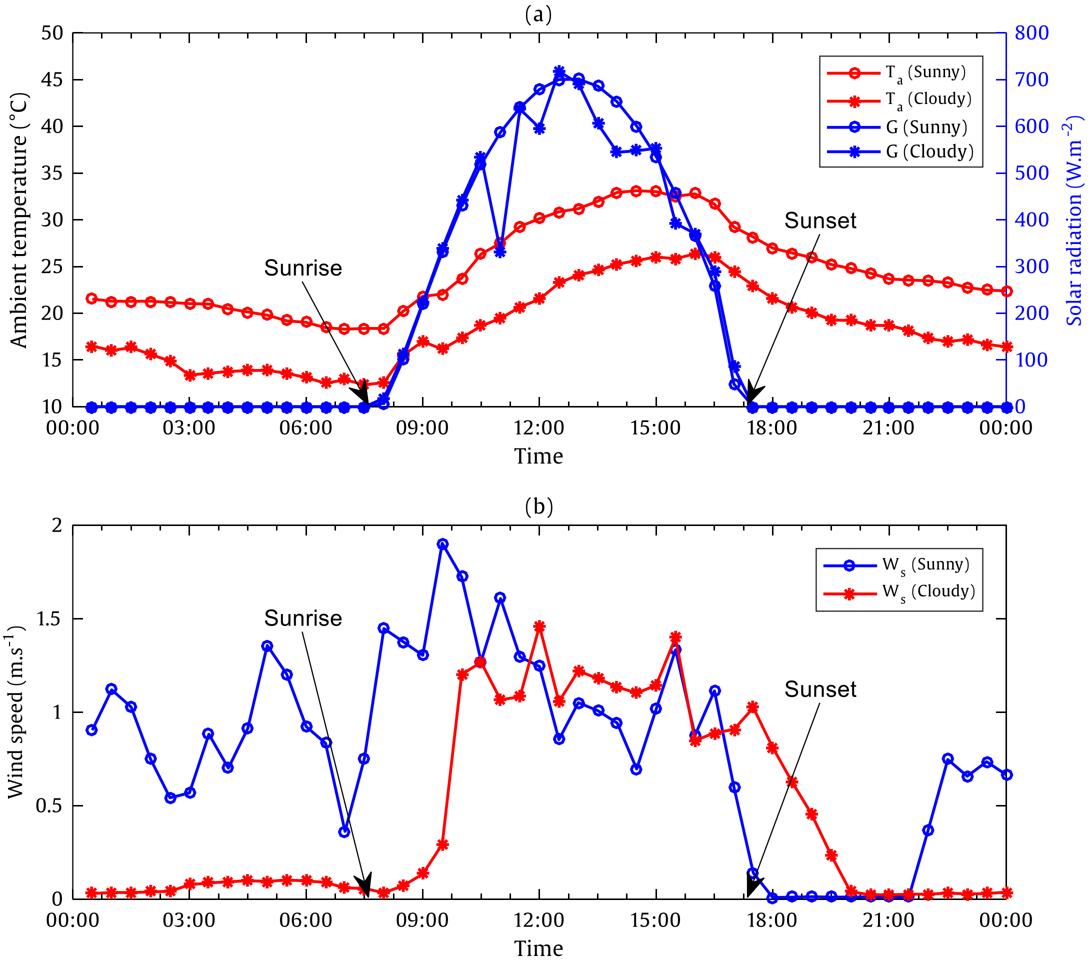

Figure IV.31: Weather data gathered on December 25, 2022: (a) ambient temperature and solar radiation, and (b) wind speed.

IV.3.2.1 Temperature prediction

The distribution of temperature on the top and back surfaces of the module at various hours of the day on December 25, 2022 (a sunny day), is shown in Figure IV.32, revealing a nonuniform temperature profile. This uneven distribution is primarily attributed to the complicated fluid (air) flow phenomena surrounding the solid module, leading to variable heat transfer coefficients. Notably, the back surface of the module exhibits higher temperature values, a result of the reduced rate of heat transfer, produced by the wake effect developed at the module’s rear surface. The bottom edges of the module benefit from cooling due to wind and lower ambient temperatures, while in the morning and late afternoon, the ambient temperature approaches or even exceeds the module’s temperature. Despite the winter season and relatively low temperatures, the module’s temperature can reach significantly higher levels than the ambient temperature during the day, highlighting the potential to harness this heat for various applications.

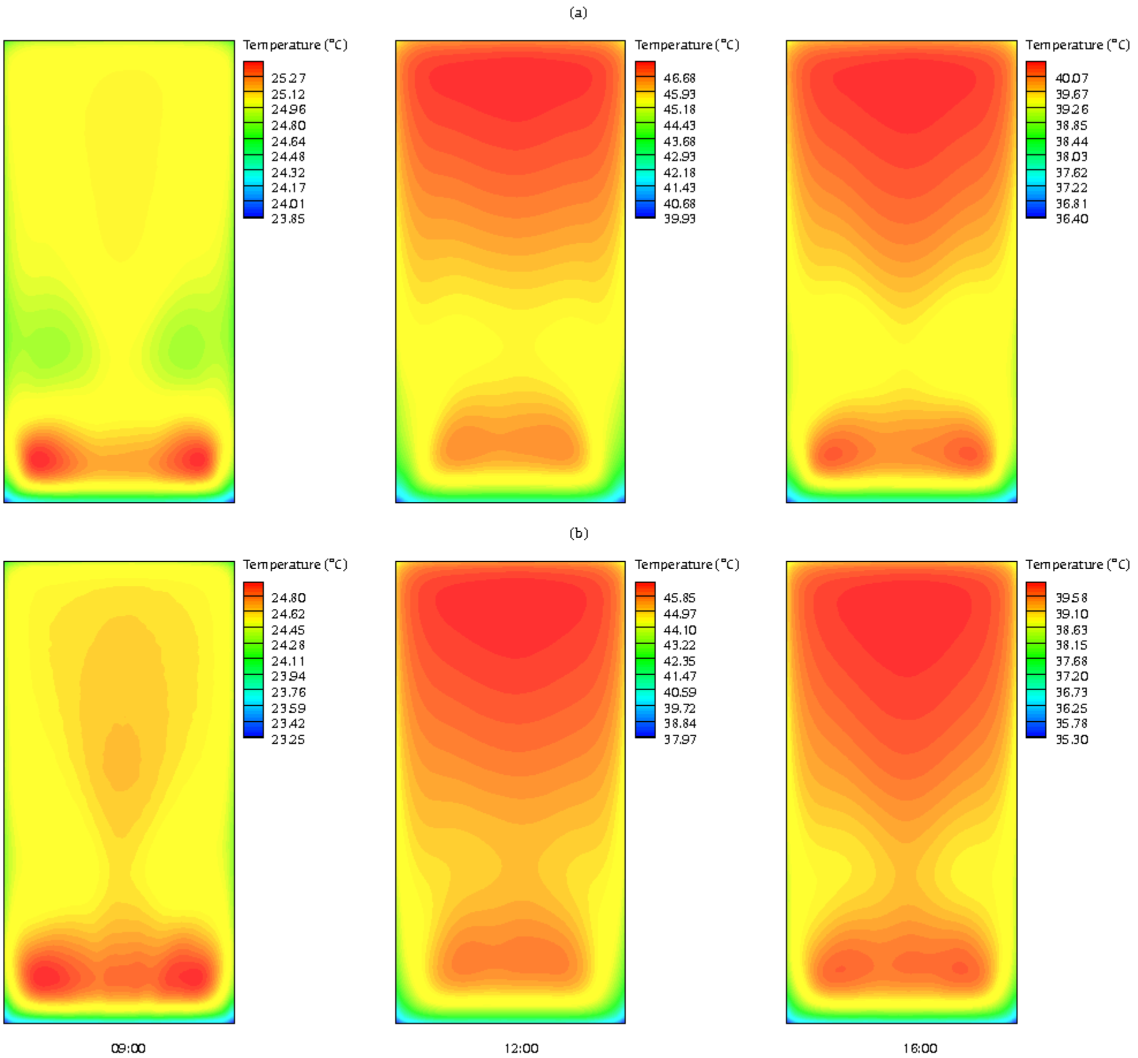

Figure IV.32: Contours of temperature at various time steps on December 25, 2022 (sunny day): (a) back side of the module and (b) top side of the module.

During cloudy day, in general a similar distribution of temperature was observed (Figure IV.33), although the temperature at the back-side was significantly lower during noon time, with a difference of up to 10 °C compared to the sunny day. This temperature variation can be primarily attributed to the reduced solar radiation reaching the module’s surface, compounded by a lower ambient temperature. The highest difference in ambient temperature between the sunny and cloudy days reached 8.62 °C, contributing to the noted drop in the back-side temperature of the module.

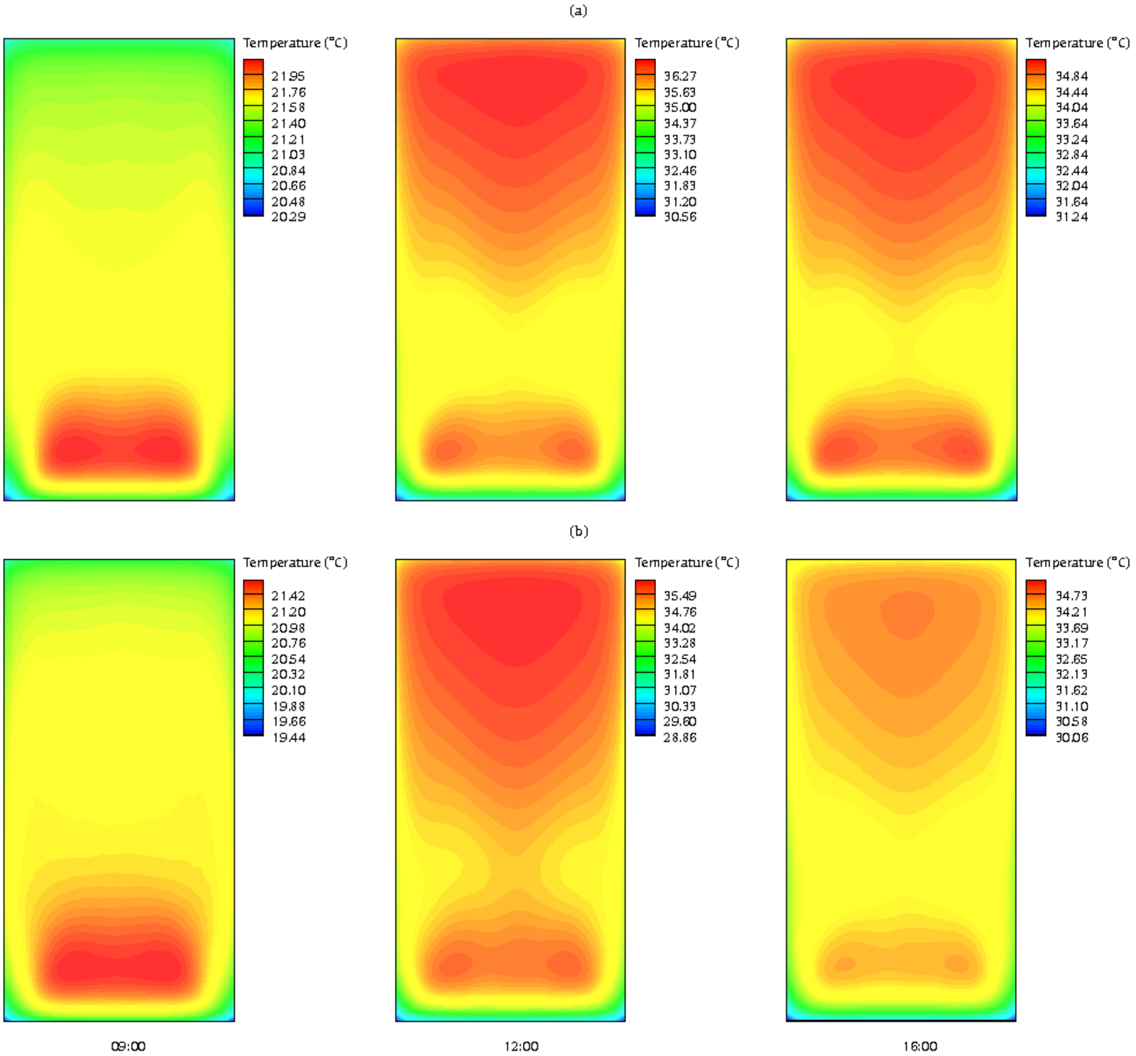

Figure IV.33: Contours of temperature at various time steps on January 02, 2023 (cloudy day): (a) back side of the module and (b) top side of the module.

The CFD simulations also enable the prediction and analysis of heat conduction inside the photovoltaic module. As shown in Figure IV.34, the average variation of temperature across the various layers of the module indicates that, as predicted, the cells layer experiences the highest temperatures, after that is the back-side temperature, whereas the top-side layer maintains lower temperature values. This distribution occurs because the photovoltaic cells layer absorbs the majority of the solar energy. The largest difference in temperature between the cells and back layers $(T_{cells} - T_{back})$ was at $0.797\ °C$, whereas the difference between the cells and top layers $(T_{cells} - T_{top})$ reached $1.470\ °C$, which aligns with intervals noted in the literature. Additionally, the graph illustrates that the temperature differences between the various layers increase at higher solar radiation (G) levels, typically observed during noon, and decrease as G values drop. To evaluate and quantify the deviation and uncertainties in the simulation outputs compared to the measured data, the ASME (American Society of

Mechanical Engineers) approach [200] was employed, Here $E = S - D$, represents the comparison error, with S denoting numerical simulation results and D representing experimental data. For the sunny day, the maximum error recorded was 2.4 °C, with a mean error of only 0.32 °C. On the cloudy day, these values were higher, with a maximum error of 5.3 °C and an average of 0.53 °C.

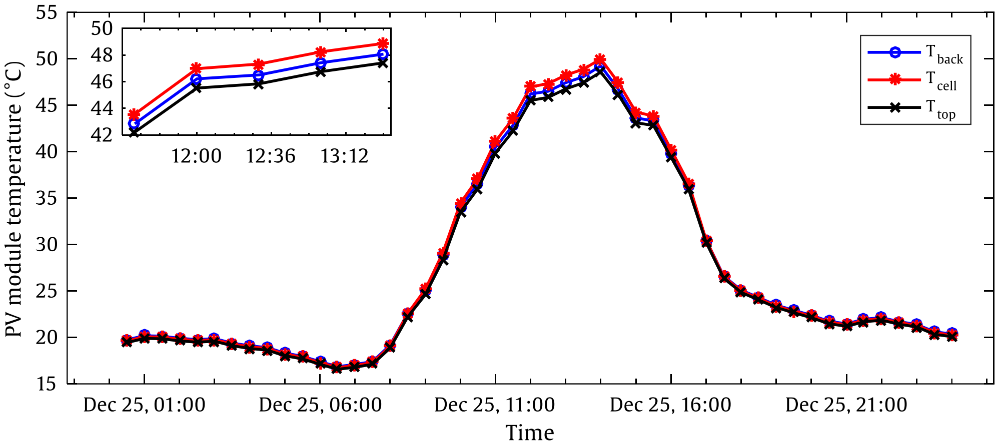

Figure IV.34: Profiles of temperature prediction for the various layers of the module on December 25, 2022.

The results yielded by the simulations for predicting the operating temperature of the module using CFD, are compared with measured data and other established photovoltaic module temperature models. Figure IV.35, presents the comparison results, illustrating that the CFD simulation results align closely with the experimental data. In various climatic conditions, both sunny (Figure IV.35 (a)) and cloudy (Figure IV.35 (b)) days, the simulation approach—grounded in the principles of fluid flow and heat transfer—estimated module temperature accurately, and outperform other literature models. Moreover, incorporating radiative heat transfer and accounting for free convection heat transfer in this study enhanced prediction results, leading to well-estimated photovoltaic module temperatures. Specifically, on sunny days, other models tend to overestimate module temperatures, with average deviations of 2.38 °C for the Ross model, 1.68 °C for the King model, and 1.49 °C for the Skoplaki model, while the numerical simulation achieved a mere 0.32 °C deviation.

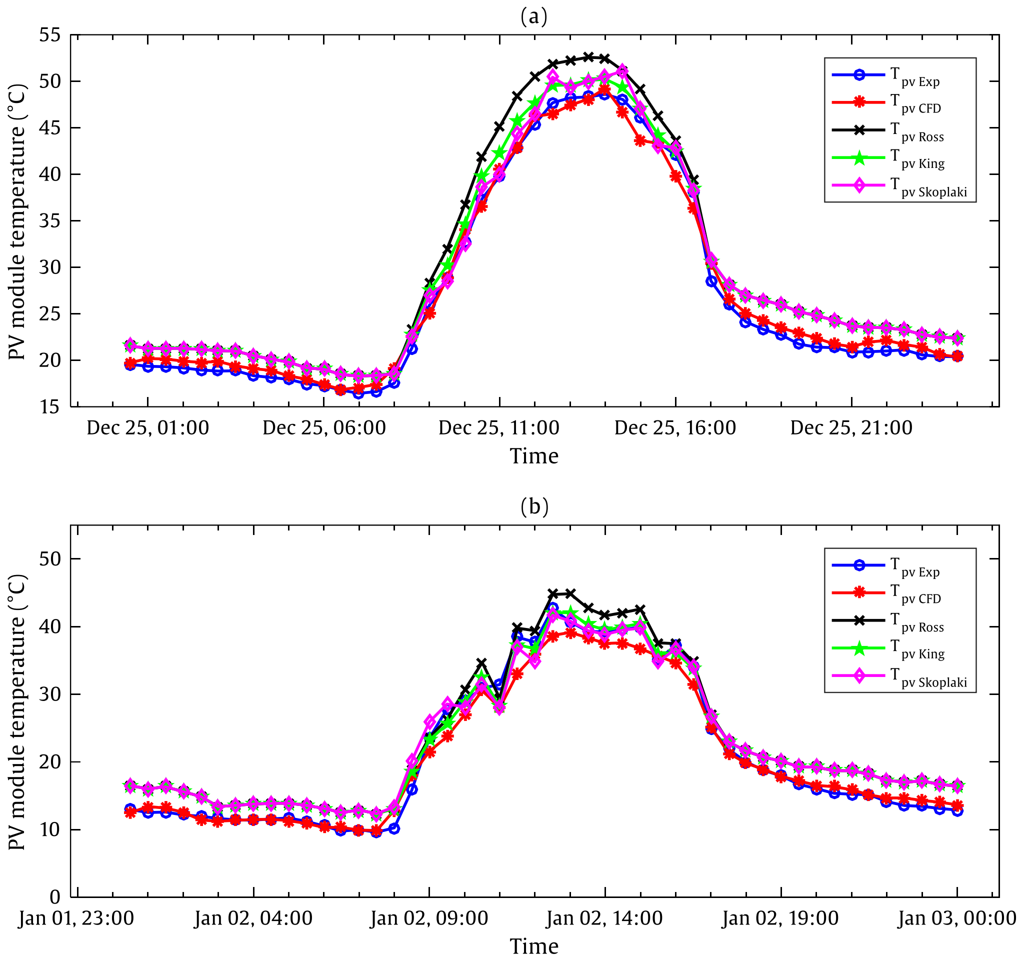

Figure IV.35: Comparison of simulation outcomes with measured data and established temperature models, (a) for sunny day and (b) for cloudy day.

The various models considered in this study are assessed using a number of statistical indicators, as shown in Table IV.7. Notably the numerical simulations conducted in this study demonstrate higher accuracy when in comparison with the measured data, achieving a high R^2 value of 0.995 along with an elevated adjusted R^2 value, as well as the predicted R^2. The errors in the simulation results were also less than that of all other literature models.

Particularly, for December 25, 2022 (a sunny day), the Mean Absolute Error (MAE) of the operating temperature of the module from the simulations results was only 0.822 °C, whereas other models exhibited significantly larger errors: 2.715 °C for the Ross model, 2.016 °C for the King model, and 1.861 °C for the Skoplaki model. Although the errors were somewhat larger on the cloudy day, the CFD simulations remained more accurate in calculating the operating temperature of the module, as indicated by the correlation coefficient and the adjusted and predicted R^2 values. The error values for the simulation-based module operating temperature predictions were 1.702 °C for RMSE, 1.174 °C for MAE, and 2.896 °C for MSE, which were notably better than the results of the other statistical models evaluated in this study. Further details regarding the statistics of the different models can be found in Table IV.7.

Table IV.7: Assessment of various models' performance against experimental data utilizing statistical indicators.

Model	R^2	$adj\ R^2$	$pre\ R^2$	RMSE	MAE	MSE	MAPE (%)
				Sunny day			
Present (CFD)	0.995	0.991	0.991	0.983	0.822	0.966	3.243
Ross	0.996	0.925	0.942	2.912	2.715	8.481	10.386
King	0.996	0.960	0.963	2.128	2.016	4.530	8.669
Skoplaki	0.993	0.963	0.964	2.048	1.861	4.196	8.205
				Cloudy day			
Present (CFD)	0.988	0.974	0.970	1.702	1.174	2.896	5.199
Ross	0.988	0.935	0.939	2.696	2.535	7.271	16.124
King	0.988	0.947	0.939	2.439	2.171	5.947	15.149
Skoplaki	0.990	0.944	0.931	2.518	2.198	6.339	15.420

IV.3.2.2 Parametric study

In this part of the study, a parametric study is conducted to assess and evaluate the impact of various parameters, and their relation to the module operating temperature, and consequently, its power output. The parameters analyzed include wind speed, inclination angle, solar radiation, and ambient temperature. Additionally, the interactions between these parameters are examined to gain a comprehensive understanding of their combined effects on module performance.

1. Effect of solar radiation

First, this study investigates the influence of solar radiation on the temperature of the module, considering a broad range of solar radiation levels from 100 to 1000 W/m². The analysis is conducted at an inclination angle of α = 33° with varying ambient temperatures and wind speeds. The simulation results, presented as temperature contours in Figure IV.36, show that for an ambient air temperature of $30\ °C$ and a wind speed of $1\ m/s$, a solar radiation of $100\ W/m^2$ results in a low and relatively uniform distribution of temperature on the module's back surface. Conversely, higher solar radiation levels, such as 550 and $1000\ W/m^2$, lead to a nonuniform temperature distribution.

Furthermore, T_{back} rises significantly with increasing solar radiation, with temperature differences (ΔT) exceeding $20\,°C$ at $G = 1000\,W/m^2$. As illustrated in Figure IV.37, T_{back} increases linearly with G, corroborating findings in the literature [84, 114]. The slop of the graph ΔT versus G varies with different wind speeds, indicating that W_s significantly impacts the rate of change in module temperature, likely due to variations in convective cooling strength. When examining a constant wind speed of $1\,m/s$ alongside different ambient temperatures, the increase in T_{back} remains consistent; however, it is evident that for a specific solar radiation value, a 30 °C rise in T_a leads to an average increase in module temperature of 5.8 °C.

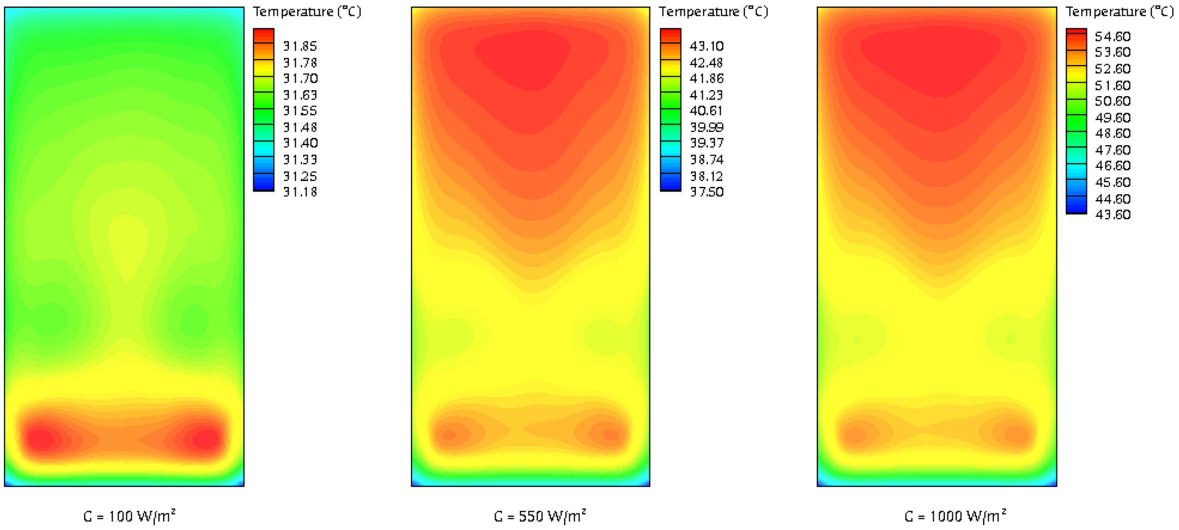

Figure IV.36: Temperature contours of T_{back} at varying solar radiation levels for $W_s = 1$ m/s and $T_a = 30\,°C$.

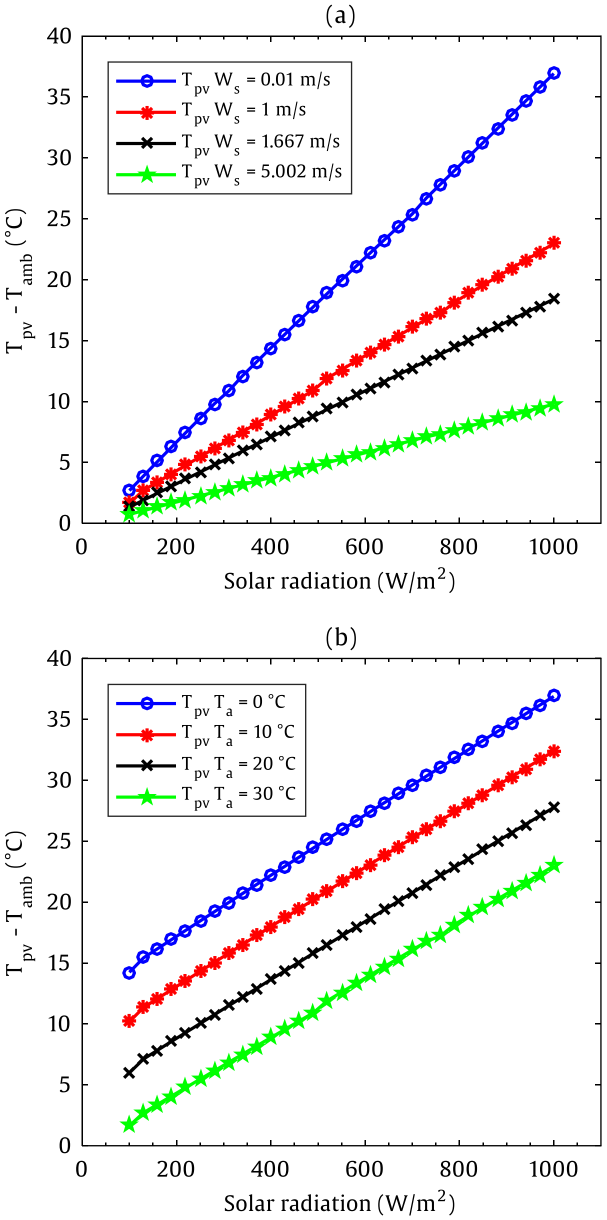

Figure IV.37: Variation of T_{back} as a function of G: (a) for various wind speeds and (b) for different ambient temperatures

2. Effect of ambient temperature

Similarly, a crucial variable in solar photovoltaics performance, is the ambient air temperature, and this study investigates its influence on module operating temperature at various wind speeds. The simulation results are presented as temperature contours of T_{back} for different ambient temperatures at a wind speed of 1 m/s (Figure IV.38), The findings reveal that an increase in T_a at constant solar radiation (G) and wind speed (W_s) leads to a significant rise in T_{back}. Moreover, lower ambient temperatures contribute to reducing T_{back} by enhancing the rate of heat transfer due to a larger gradient of temperature.

Additionally, the relation between T_{back} and T_a is illustrated in Figure IV.39, which demonstrates that module operating temperature exhibits a linear relation with T_a at a steady wind speed values. This observation aligns with measured data and findings from the literature [84], Nevertheless, as wind speed increases, T_{back} decreases owed to wind-induced cooling through forced convection, coupled with increased turbulent forces and the mixing accompanying with higher forces of inertia. It is also noteworthy that the rate of temperature decrease diminishes with increasing wind speed. For instance, as the wind speed increases from nearly no wind speed condition (0.01 m/s) to 1 m/s, a mean temperature drop of 13.97 °C is achieved. In contrast, when the wind speed rises from 3.66 m/s to 5 m/s, the temperature drop is only 1.47 °C.

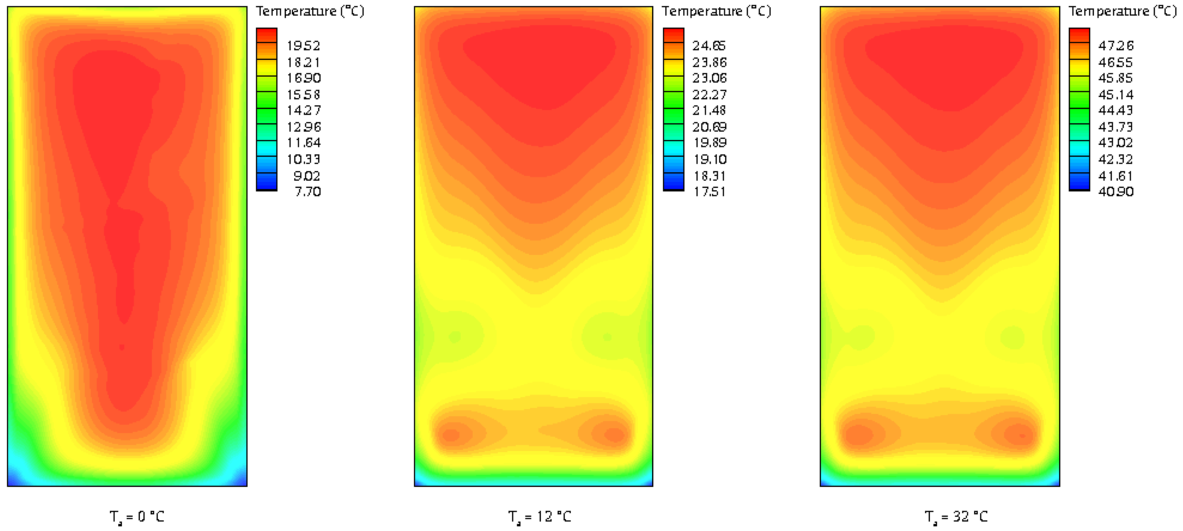

T_a = 0 °C T_a = 12 °C T_a = 32 °C

Figure IV.38: Contours of temperature of T_{back} at varying ambient temperatures for $W_s = 1$ m/s and $G = 700\ W/m^2$.

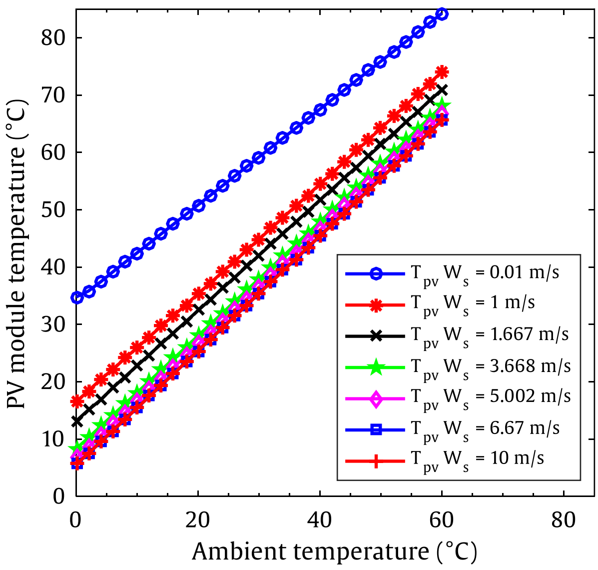

Figure IV.39: Effect of T_a on the module back side temperature (T_{back}) for different wind speeds.

3. Effect of wind speed

Additionally, the wind speed's influence of on the operating temperature was also investigated for different mounting inclination angles (α). The back-side temperature contours at various wind speeds, and for a given angle of inclination of α = 33° are shown in Figure IV.40 The figure illustrates that at low wind speeds, free convection predominates, resulting in more thermal resistance, consequently higher temperatures of the module across the surface. In contrast, as wind speed increases, forced convective cooling becomes more pronounced, effectively reducing the module temperature. Figure IV.41, presents the profiles of T_{back} for different values of wind speed and various inclination angles. In line with expectations, the cooling impact of wind on module temperature increases with the increase in wind speeds, aligning with findings in the literature [113].

Nevertheless, the difference in the cooling impact is minimal for most inclination angles at low wind speeds. This is attributed to the significant influence of buoyancy-induced natural convection at low wind speeds, leading to lower heat transfer coefficients and, therefore, less effective cooling. At higher wind speeds (around 1 m/s and above), the influence of inclination angle (α) on the cooling process becomes significant. The cooling process is quite slow and less efficient when the angle of inclination is high, such as 60° and 90°. In contrast, inclination angles less than 60° result in lower module temperatures and more effective cooling, indicating a more optimal orientation for thermal performance.

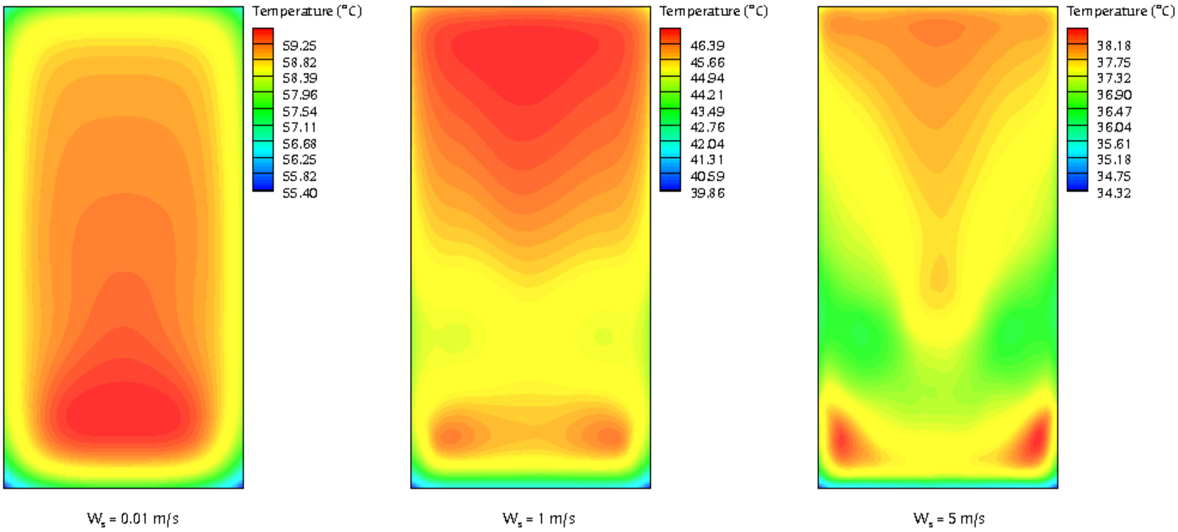

Figure IV.40: Temperature contours of T_{back} at varying wind speed values for $T_a = 30\ °C$, $G = 700\ W/m^2$ and $\alpha = 33$.

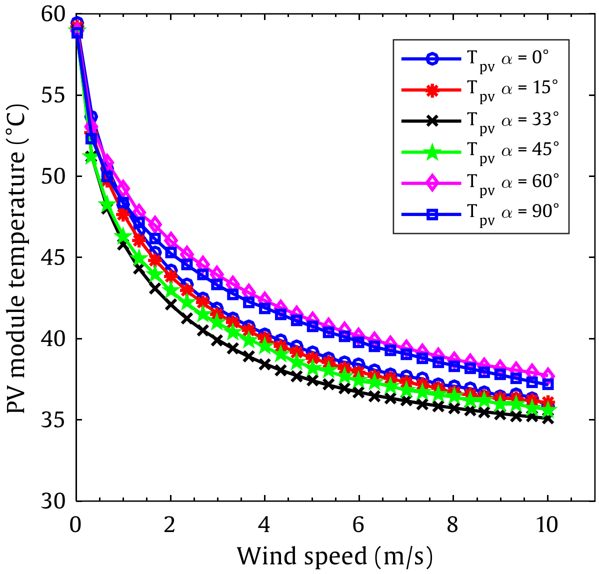

Figure IV.41: Module back-side temperature at various wind speed values and different inclination angles.

4. Effect of angle of inclination

Another critical factor affecting the cooling process for a stand-alone photovoltaic module, is its mounting angle (α). This study investigated the effects of this parameter under controlled conditions—T_a of $30\ °C$, and G of $700\ W/m^2$, and varying wind speeds. Contours of temperature from the simulation output for $\alpha = 0°$, $33°$, and $60°$ are presented in Figure IV.42. The distribution of temperature across the surface of the module is notably affected by the inclination angle, demonstrating that α affects how heat disperses across the module.

Interestingly, as shown in Figure IV.43 the average back-side temperature (T_{back}) of the module is largely unaffected by α, aligning with findings in literature [114]. However, at very low wind speeds, there is a gradual decrease in T_{back} as α increases from 0° to 90°. This trend can be attributed to considerable role of buoyancy-induced natural convection; with the module being at higher temperature than its surroundings, an increasing inclination angle disrupts the boundary layer, forming plumes on the top surface. This, in turn, reduces thermal resistance and enhances heat transfer.

At higher wind speeds, convective cooling effects take precedence, and the optimal cooling performance is observed at α = 33° for all wind speeds. This suggests that while angle may minimally impact average module temperature at moderate-to-high wind speeds, a 33° inclination offers the most effective cooling by leveraging wind-induced convection.

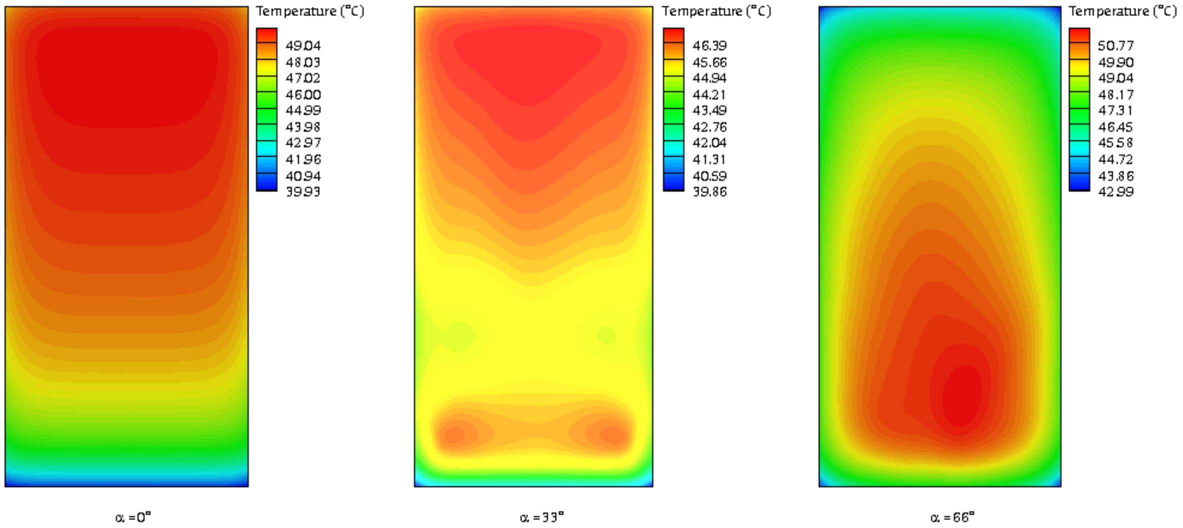

Figure IV.42: Temperature contours of T_{back} for varying inclination angles, at $W_s = 1\ m/s$, $T_a = 30\ °C$, and $G = 700\ W/m^2$.

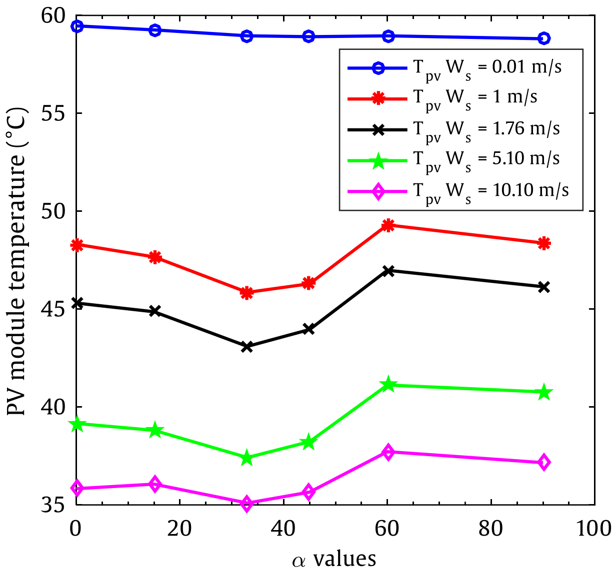

Figure IV.43: Module back-side temperature at varying inclination angles (α) and different wind speed values.

IV.3.2.3 Regression-based temperature model

Supported by the parametric study, alongside measured and numerical findings, a regression-based model was constructed to predict the operating temperature of the module (T_{pv}) using weather variables. The model uses ambient temperature, solar radiation, and wind speed as inputs, in which solar radiation (G) includes a scaling constant factor to adjust for its relatively larger magnitude. Additionally, T_{pv} was found to scale linearly with T_a and tends to decrease exponentially with increasing wind speed. Consequently, T_a is multiplied by a constant coefficient to reflect the linear correlation with the output (T_{pv}), whereas wind speed is scaled by a coefficient within an exponential function to incorporate its negative impact on T_{pv}. The suggested model thus takes the following form in Eq. (IV.14):

$$T_{pv} = aT_a + bGe^{cW_s} \tag{IV.14}$$

In the above equation a, b, and c were determined to be 0.905, 0.0291, and -0.031, respectively. A sensitivity analysis was conducted to evaluate the influence of each input on the predicted target (T_{pv}), revealing that with a solar radiation of $700\, W/m^2$, an ambient air temperature of $30\ °C$, and a wind speed of $1\ m/s$.

Eq. (IV.14) estimates the module temperature at 46.9 °C, which is a reasonable estimate when compared to measured data. The analysis indicated that, with other inputs held constant, increasing T_a from 0 to $47\,°C$ would raise T_{pv} by around $42\,°C$; raising G from 0 to $1000\,W/m^2$ at $T_a = 30\,°C$ and $W_s = 1\,m/s$ would result in a 28 °C increase in the temperature of the module; while, increasing W_s from 0 to $10\,m/s$ at $T_a = 30\,°C$ and $G = 700\,W/m^2$ would reduce T_{pv} by about $5.6\,°C$. These findings confirm the significant effect of each input on the temperature of the module. The suggested equation was further validated on a new data set (03-01-2023) with solar radiation reaching up to $700\,W/m^2$, a maximum ambient temperature of $26\,°C$, and wind speeds up to $2\,m/s$.

Compared with other models, results shown in Figure IV.44, demonstrate that the suggested model accurately align with measured data and provides superior temperature predictions. The model performance statistics revealed a coefficient of determination of 0.989, adjusted and predicted R^2 values of 0.987, a MAE of 1.009, and a MSE of 1.703. Additionally, the model's standard error was only 1.363, delivering a 10.4% improvement in accuracy over the best results from existing models in the literature.

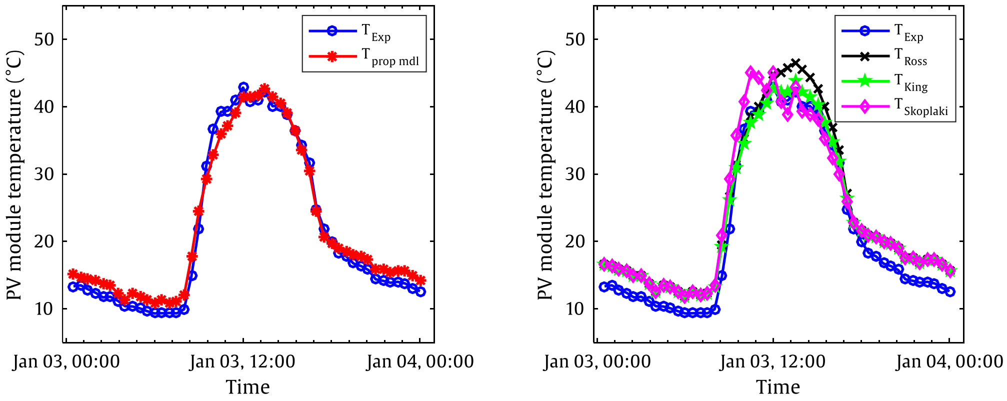

Figure IV.44: Comparison of results from the suggested model with measured data and other models found in the literature.

IV.3.3 Thermal modeling

In this study, the calculation of photovoltaic module temperature evaluated through the suggested algorithm, grounded on heat transfer and fluid flow theories, is carried out. An experimental dataset, which includes recorded values of T_a (ambient temperature), W_s (wind speed), G (solar radiation), and T_{back} (back-side module temperature), was used for the simulation. Data was collected from March 15 to 19, 2023. Figure IV.45 illustrates this recorded data, displaying a typical pattern where ambient temperature (T_a) and solar radiation (G) increase from morning until noon and then decrease toward evening. In contrast, W_s values show a random and unpredictable behavior throughout the day.

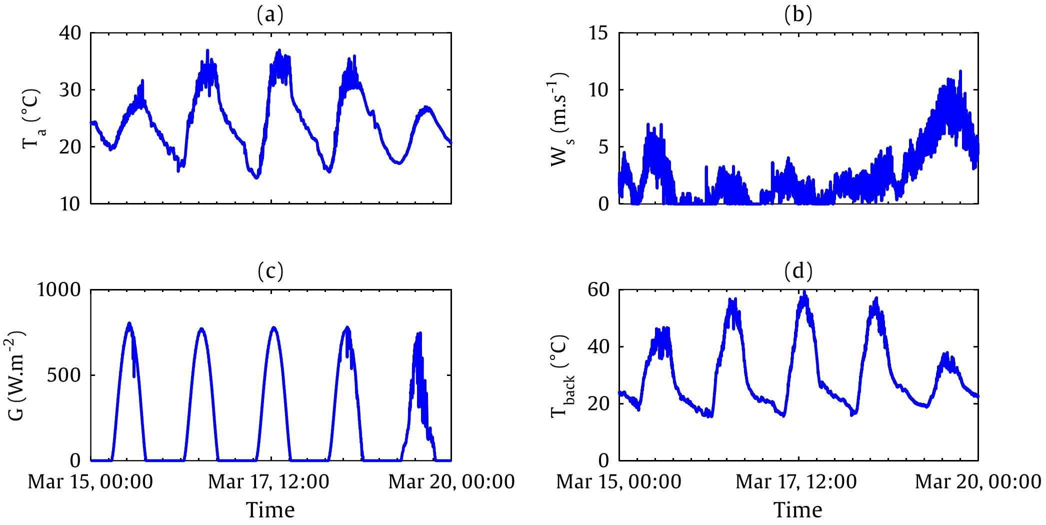

Figure IV.45: Weather data collected between March 15 and 19, 2023: (a) ambient temperature, (b) wind speed, (c) solar radiation, and (d) module temperature.

IV.3.3.1 Heat transfer analysis

To evaluate energy losses from the module to its surroundings, this work quantifies the heat flux leaving each module surface. The energy distribution, as depicted in Figure IV.46, shows that a significant amount of the solar energy absorbed by the solar cells dissipates as heat, primarily through radiative losses from the top surface (T_{top}) to the sky (T_{sky}). Similarly, considerable convective heat transfer occurs on both module sides, matching the radiative heat exchange between the back surface (T_{back}) and the ground (T_{gr}) during sunny conditions. On average, around 16% of the solar energy being absorbed is converted to electricity, whereas roughly 34% is emitted by convection—15.8% from the front side and 18.2% from the rear side. The remainder 50% is wasted by radiation, with 35% from the front side and around 15% from the rear side of the module, indicating that the majority of absorbed energy dissipates as heat. This highlights the possibility for applications such as photovoltaic/thermal (PV/T) systems.

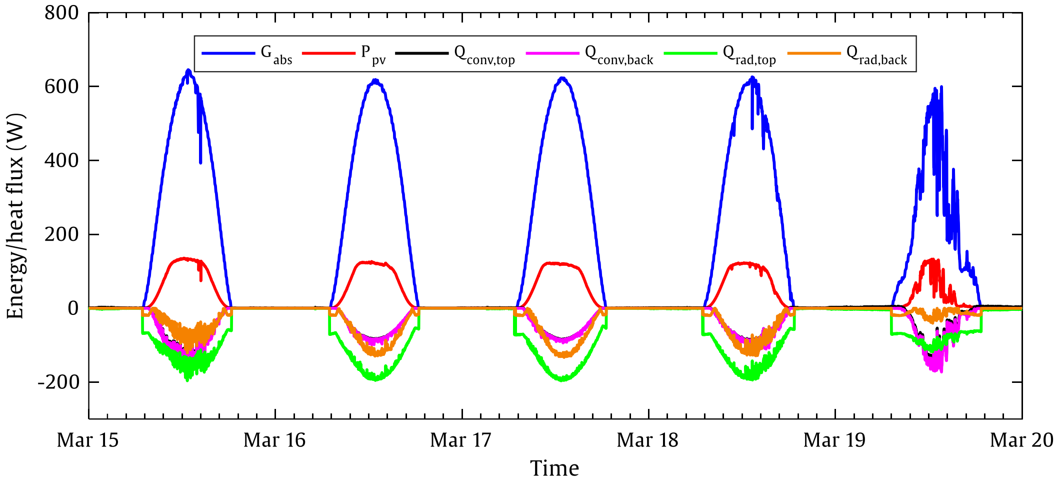

Figure IV.46: Distribution of energy depicted as power output and heat loss.

IV.3.3.2 Wind heat transfer coefficient

The wind heat transfer coefficient (h_{conv}), crucial for predicting T_{back}, was also examined in this study. Simulation results based on experimental data, applying the previously discussed Nu_{ave} correlations, alongside h_{conv} estimates from Eq. (IV.15) and several literature models, are illustrated in Figure IV.47.

The figure reveals that Eq. (IV.15) closely aligns with simulation outputs, while literature models show substantial deviation from the results obtained in this study. Notably, this work's results effectively bridge the gaps in existing models, as both the simulation algorithm results and Eq. (IV.15) fall between the values suggested by Sartori's models for laminar and turbulent flows (III.27) and (III.28), respectively. It is also essential to note that Eq. (IV.15), omits radiative effects and considers only one module side, thereby isolating the convection heat transfer on considered side.

$$h_{conv} = 1.945 W_s^{1.048} \tag{IV.15}$$

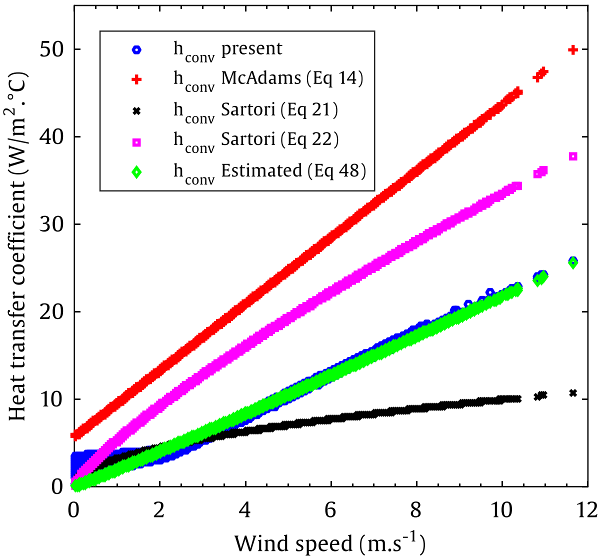

Figure IV.47: Assessment of the wind heat transfer coefficient in this study with equations reported in the literature.

IV.3.3.3 Temperature prediction and model accuracy

In Figure IV.48, the simulation results for predicting T_{back} by the developed algorithm in this work are evaluated against measured data, showcasing a high degree of accuracy. The calculated operating temperature for the module aligns closely with the measured values, indicating the algorithm's effectiveness in predicting module temperatures across varying weather conditions. Built upon heat transfer and fluid flow basics, the simulation algorithm integrates several features, involving free and forced convective heat transfer, radiation and mixed convection heat transfer, as well as the different conditions for the boundary layers (including laminar, turbulent, and mixed flow regimes).

This far-reaching consideration enhances prediction accuracy, yielding reliable estimates of T_{back}. The model's ability to account for complex heat transfer dynamics across various conditions is further reflected in its strong agreement with experimental data. A minor deviation in predicted module temperature compared to the actual data was noted on March 19, 2023, due to abrupt changes in solar radiation, as shown in Figure IV.45. Despite these fluctuations, the model still achieved a reasonable T_{back} approximation, with an average deviation of only 2.490 °C, remaining within a permissible margin of error.

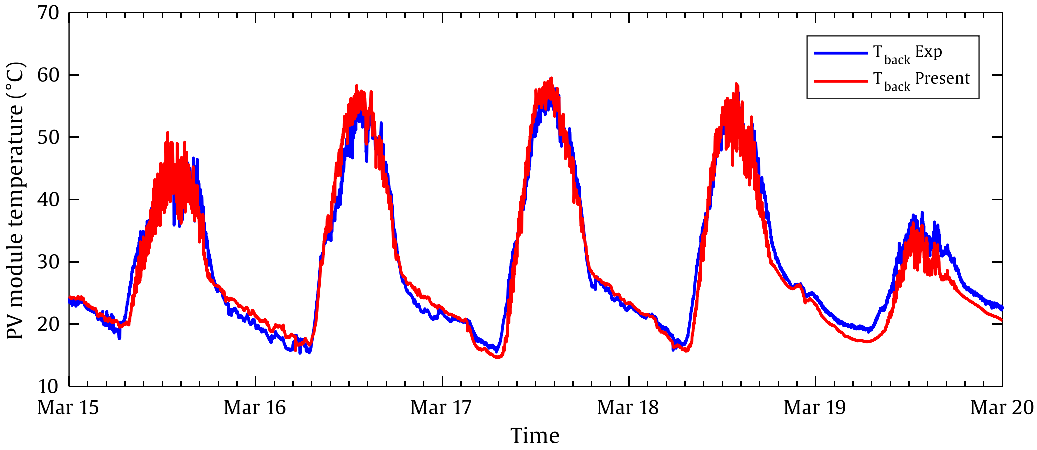

Figure IV.48: Comparison of the predicted T_{pv} values from the algorithm the measured data during the period of March 15 to 19, 2023.

A quantitative evaluation of the predicted module temperature T_{back} using statistical techniques was conducted to evaluate the performance of the simulation algorithm. As shown in Figure IV.49, a scatter plot of calculated against experimental T_{back} demonstrates a concentrated pattern along the 45-degree line of perfect regression, with a linear best fit yielding an R^2 of 0.963, indicative of precise predictions. Additionally, the adjusted R^2 is also high at 0.957, underscoring robust model performance with respect to the considered input parameters.

Regarding error metrics, the predicted T_{back} registered RMSE, MAE, and MSE values of 2.344, 1.883, and 5.495, respectively. The standard error of the predicted temperature was 2.345, and the Mean Absolute Percentage Error (MAPE) stood at just 6.614%, well below the 10% benchmark, confirming the algorithm's high accuracy. Notably, over 96% of the predicted temperature errors were under the 5 °C threshold, a commonly accepted limit that would yield less than a 3% discrepancy in the prediction of the power output of the photovoltaic module, as referenced in studies [99, 102].

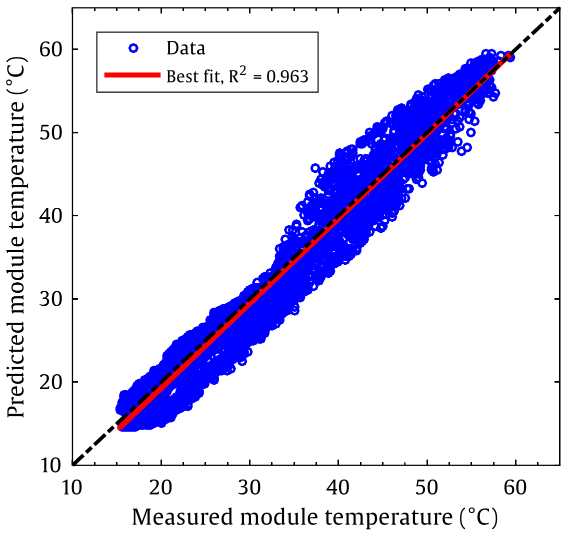

Figure IV.49: Scatter plot comparing the predicted module temperature against the experimentally measured values.

The simulation algorithm was developed to predict heat conduction in the module as well. Analyzing March 17, 2023, as a typical day Figure IV.50, illustrates the temperature profiles across different layers of the photovoltaic module. As anticipated, the cell layer exhibits higher temperature values, with lower temperatures on the back side and the lowest on the top side. This trend results from the thermal pathway: heat must travel greater distances through the encapsulant (EVA) and glass layers at the top compared to the EVA and back-sheet thickness on the back side. Additionally, as noted earlier, convective heat loss is similar on both sides, whereas radiative heat loss is significantly greater on the top side than the back side. The maximum temperature difference between the cell and back side $(T_{cell} - T_{back})$ was approximately 0.7 °C, while the difference between the cell and top side $(T_{cell} - T_{top})$ reached around 1.4 °C, consistent with ranges reported in the literature [171, 194]. In addition, Figure IV.50 shows that these temperature differences correlate with solar radiation (G) values, where higher G values result in larger temperature differences and lower G values yield smaller differences.

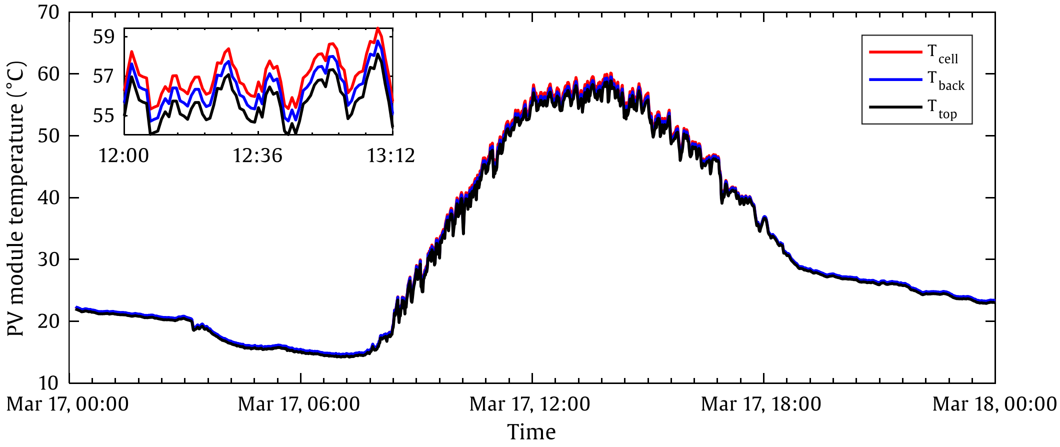

Figure IV.50: Profiles of calculated temperature for the module's top, back side, and cell layers on March 17, 2023.

IV.3.3.4 Comparison with literature models

In a comparison between the simulation algorithm and several temperature models presented in the literature to evaluate its performance, including the NOCT model, PVSyst's model [201-203], and Mattei's model [121]. The results shown in Figure IV.51 indicate that the developed algorithm in this work aligns well with measured data and the literature models. Notably, it consistently provides more accurate predictions compared to the others, demonstrating one of the best overall performances when compared to experimental results and surpassing nearly all other models. Even on cloudy days, characterized by abrupt fluctuations in solar radiation, the algorithm delivers reliable and reasonable outcomes.

In detail, the NOCT model tends to considerably overpredict module temperatures across all situations. On the other hand, the PVSyst model yields satisfactory predictions on sunny days but exhibits substantial errors during cloudy conditions. Mattei's model performs reasonably well on cloudy days, such as March 19, 2023; however, it significantly underestimates module temperatures on days with clear skies. Conversely, the presented simulation algorithm shows an excellent agreement with experimental data under both sunny and cloudy conditions. This success is attributed to the algorithm's ability to account for the dynamic behavior of the module and its surrounding environment.

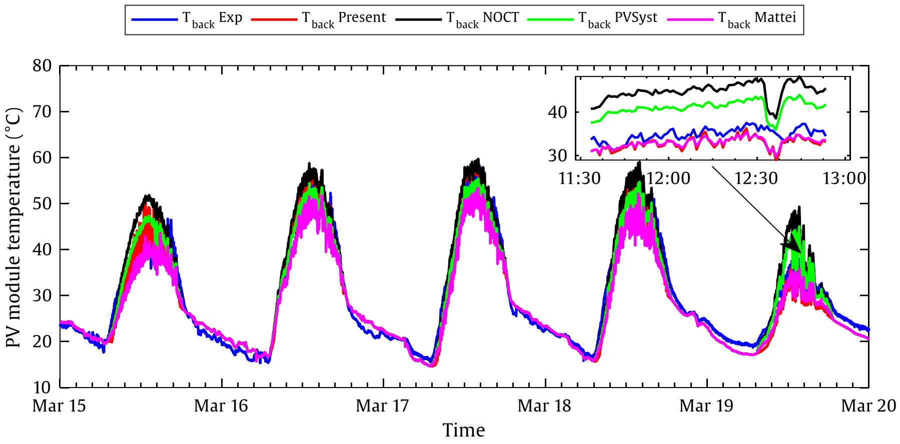

Figure IV.51: Comparison of the simulation algorithm from this study with experimental data and other temperature models.

Table IV.8 presents a statistical assessment of the simulation algorithm's results besides other module temperature models from the literature. The proposed algorithm demonstrates a high R^2 value of 0.963, along with a correspondingly high adjusted R^2. Moreover, the predictive error associated with the simulation results is lower than that of all other considered models. Specifically, the mean absolute error (MAE) for the simulated T_{back} is only 1.883. In comparison, the King model recorded the lowest MAE at 1.663, while the Bailek et al. model exhibited the highest MAE at 3.454. Regarding mean squared error (MSE), the simulation results produced an MSE of 5.495, which is very close to the second-best result of 5.039 achieved by the PVSyst model. Conversely, the Bailek et al. model yielded the largest MSE at 18.781. Additional insights regarding the statistical assessment of those models are provided in Table IV.8.

Table IV.8: Evaluation of the performance of various models compared to experimental data.

Model	R^2	$adj\ R^2$	RMSE	MAE	MSE	MAPE (%)
Present	**0.963**	**0.957**	**2.344**	**1.883**	**5.495**	**6.614**
NOCT [82, 91]	0.957	0.937	2.839	1.993	8.057	6.588
PVSyst [201, 203]	**0.962**	**0.960**	**2.245**	**1.757**	**5.039**	**6.007**
TamizhMani [101]	0.880	0.866	4.136	3.238	17.103	12.686
Mattei [121]	0.968	0.921	3.172	2.468	10.062	7.703
Skoplaki et al. [104]	0.914	0.897	3.633	2.665	13.201	8.359
Bailek et al. [77]	0.963	0.853	4.334	3.454	18.781	10.855
King et al. [102]	**0.973**	**0.966**	**2.068**	**1.663**	**4.277**	**5.843**

IV.3.3.5 Proposed models

Grounded on the algorithm's findings and the investigation conducted in this work, along with the available measured data, a practical, explicit model is proposed for predicting T_{cell}, which resembles Eq. (III.49), This model utilizes solar radiation (G) and ambient temperature (T_a) as input variables, with the constant k set at 0.023. This value reflects the daily average predicted by the simulations and aligns well with findings documented in the literature. Consequently, the proposed model can be expressed in the form of Eq. (IV.16):

$$T_{cell} = T_a + 0.023G \tag{IV.16}$$

While the model presented in Eq. (IV.16) implicitly incorporates convection (effects of wind) and radiation, using k as constant coefficient may not be the most effective approach in all situations. To enhance the model's ability to account for the dynamics and variations in ambient conditions such as T_a, W_s, and T_{cell}, an alternative formulation is proposed. This new model could potentially be expressed in the form of Eq. (IV.17):

$$T_{cell} = T_a + \left(\frac{\tau\alpha - \eta_{ref}(1 - \mu_{ref}(T_{cell} - T_{ref}))}{4.132W_s + 0.088T_{cell} - 7.215}\right)G \tag{IV.17}$$

In this model, $\tau\alpha$ is set to 0.81, while η_{ref} and μ_{ref} denote the efficiency of the module and the coefficient of temperature at the reference state, respectively, with T_{ref} representing the reference temperature $(298.15\ K)$. Because T_{cell} is present on both sides of the expression in Eq. (IV.17), an iterative solution must be employed to calculate it. It is important to note that the temperature values in Eq. (IV.17) are expressed in Kelvin. If the model is applied to T_{back}, the $T_{cell} - T_{back}$ temperature difference reported in this study and in literature should also be taken into account.

To evaluate the effectiveness of the models suggested here, another measured dataset from November 29, 2022, was used. The yielded results produced by Eq. (IV.16) and (IV.17) are illustrated in Figure IV.52, demonstrating that the implicit model is particularly effective at capturing the dynamics of T_{cell} in response to variations in ambient conditions and efficiency.

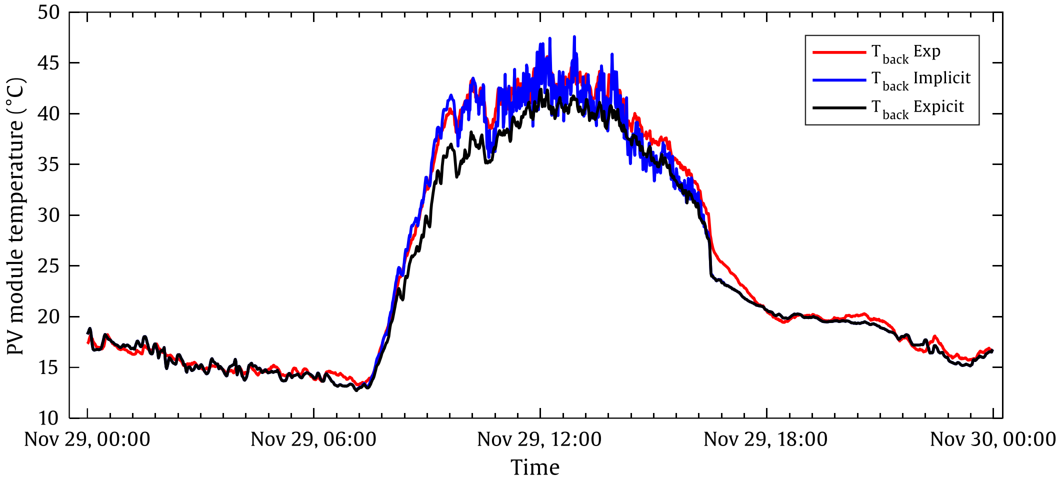

Figure IV.52: Comparison of the predictions of the suggested implicit and explicit equations against measured data using new datasets.

Figure IV.53 presents a Taylor diagram assessing the proposed models' performance on the unseen data, illustrating that these models and the associated simulation algorithm rank among the most effective modeling methodologies. The statistical metrics for the considered models indicate comparable R^2 values of 0.99, with the adjusted R^2 being at 0.989 for the implicit model and 0.970 for the explicit model. Furthermore, the mean absolute error (MAE) was calculated at 0.802 for the implicit model and 1.325 for the explicit model, while the mean squared error (MSE) values were 1.268 and 3.505, respectively. The mean absolute percentage error (MAPE) was found to be 3.036% for the implicit model and 4.438% for the explicit model, with standard errors of 1.127 and 1.874, respectively. This suggests that Eq. (IV.16) can serve as preliminary estimate of T_{cell} or as an initial estimate for the implicit model; yet, for more precise prediction, Eq. (IV.17) is advised.

Overall, numerous advantages in this study and the presented module temperature equations emerge in comparison to existing literature models, particularly regarding the suggested algorithm and the implicit model. In contrast to the model of PVSyst, the current thermal modelling approach accounts for a varying efficiency of the photovoltaic module, which better reflects actual module behavior. This is also the case for the wind induced convection and the wind heat transfer coefficient, which is treated as a linear function of wind speed and the default values in PVSyst assume no relation to wind speed.

Conversely, Sartori's study suggests that the wind heat transfer coefficient might follow a power law function, whereas this work allows for the coefficient to adopt any form based on selected correlations, enabling an evaluation of the most effective representation.

Additionally, many existing studies tend to overlook the effects of radiation on module temperature; however, this factor has been integrated into the presented simulation algorithm and the implicit model. Moreover, this research affords an analysis of energy balance for the module and estimating the energy losses and exchanges between the module and its ambient environment. The proposed simulation algorithm also facilitates the calculation of temperatures for various layers of the photovoltaic module, including the top, cells, and back side.

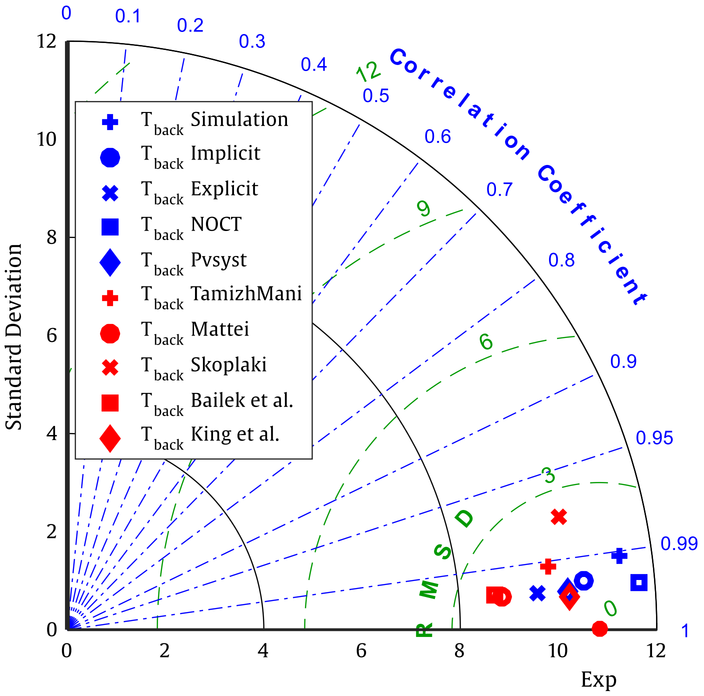

Figure IV.53: Taylor diagram illustrating the assessment of suggested algorithm, models, and literature models using new dataset.

IV.4 Conclusion

Within CHAPTER IV, the demonstration and analysis of the findings achieved in this work was carried out, both experimentally and numerically, have been presented. Due to the extensive investigations performed throughout this work, all concluding point are highlighted in the GENERAL CONCLUSION section. However, the main conclusions are as follows:

- Solar radiation, ambient temperature, and module temperature are pivotal in estimating photovoltaic (PV) module power output, showing strong correlations with P_{pv} at 0.98, 0.613, and 0.907, respectively.
- Comparing the results of all power output prediction models examined in this work, along with those in literature under both sunny and cloudy day situations, indicated that the ANN, RPL, and PL models outperform the linear equations suggested in this work and those found in existing literature.
- Regarding the prediction and linear modeling of T_{pv}, the LASSO algorithm delivers a satisfactorily accurate and sparser model which requires fewer input variables, which is a distinct advantage. By utilizing an l1 norm penalty and feature selection, this algorithm reduces the likelihood of overfitting.
- The R^2 value of the proposed model for predicting T_{pv} was 0.981, with low error metrics of 1.476 and 3.464 in terms of MAE and MSE, respectively. A detailed review of the residuals from the suggested models showed that only 14% of the prediction residuals exceed the 2.5 mark.
- Numerical simulations, based on the principles of fluid flow and heat transfer phenomena around a standalone photovoltaic module, yielded accurate predictions of module operating temperature, thereby enhancing power output estimation.
- CFD simulations yielded a predicted T_{back} with an R^2 of 0.995 and adjusted and predicted R^2 values of 0.991, with a MAE of 0.822. Conversely, the best model from literature achieved R^2 values of 0.993, 0.963, and 0.964, with a MAE of 1.861
- The proposed implicit model, grounded in a thermal modeling algorithm, yielded highly accurate results, providing an R^2 value of 0.99 and a similar adjusted R^2, with a MAE of 0.802 when evaluated on a new dataset.

GENERAL CONCLUSION

In this study, artificial neural networks (ANNs) and regression analysis were initially used to estimate and calculate the power generation of a 160W photovoltaic (PV) module situated in the El-Oued region of Algeria. Data collected over six days, from November 26 to 30 and December 4, 2022, included not only the power output of the PV module but also several climatic variables, such as solar radiation, ambient temperature, wind speed, wind direction, and relative humidity, along with module temperature and power output. Following an investigation into the effects of various training algorithms, prediction results were evaluated using the ANN model and regression models, incorporating different statistical metrics and comparisons with existing literature.

Subsequently, for predicting module temperature, twelve distinct regression and machine learning algorithms were implemented, involving a newly proposed model, focusing on linear, non-linear, tree-based, kernel-based, ANN, and probabilistic modeling approaches to predict the operating temperature of the module using a larger dataset. Experimentations took place in the El-Oued region of Algeria from December 23, 2022, to January 3, 2023. After conducting data preparation, including feature engineering and selection, the above-mentioned regression approaches served as prediction tools, assessed with various error indicators. Additionally, results from the proposed model were compared with literature models, and power output prediction was executed using this model.

Following this, three-dimensional computational fluid dynamics (CFD) simulations were conducted to calculate the back-side temperature of the 160W PV module using measured data from experimental data, where experimentations were conducted in El Oued, southeastern Algeria, on December 25, 2022, and January 2 and 3, 2023. After completing a mesh sensitivity test and validation of the numerical model, the equations governing heat transfer and fluid flow around a stand-alone photovoltaic module were numerically solved via ANSYS Fluent CFD code to determine the operating temperature of photovoltaic module. This study uniquely performed a comprehensive parametric study for the principal variables and parameters and their combinations, accounting for the different heat transfer mechanisms. Furthermore, this work was an original investigation into the prediction of operating temperature of the module under variable environmental conditions in an arid climate. Statistical indicators were used for results assessment, alongside comparisons with literature models, and a parametric study of essential variables was conducted.

Lastly, a thermal model and simulation algorithm were presented to estimate photovoltaic module temperatures utilizing measured data collected from March 15 to 19, 2023. After validating the model, the proposed algorithm was used to determine module temperature, and extensive heat and energy transfer evaluations were carried out. In addition to comparisons with literature models, statistical metrics were employed to evaluate the results. Grounded on the results of these investigations, the subsequent key takeaways can be drawn:

- Solar radiation, ambient temperature, and module temperature are crucial parameters in predicting photovoltaic power output, exhibiting the strongest correlation with P_{pv}. A high correlation between module temperature and ambient climatic conditions simplified the power generation predictions using the module operating temperature, while other parameters had less effect on the delivered output generation of the module.

- The Levenberg-Marquardt training algorithm demonstrated better predictive performance in comparison to other tested algorithms, achieving an R^2 of 99.5% and an RMSE of 2.92.

- The established ANN model predicted module power generation during the testing days accurately, with an R^2 of 0.997 and MAE and RMSE values of 1.998 and 4.10, respectively, with considering all environmental parameters. When focusing solely on solar radiation and module temperature, the R^2 was 0.995, with MAE and RMSE of 2.046 and 4.594. The accuracy difference in this case was only 0.2% lower.

- The multiple linear regression (MLR) models failed to capture the system's nonlinearity, yielding significantly lower accuracy compared to ANN estimations. Nevertheless, both the Rational-Power-Law and Power-Law models achieved notably improved accuracy in estimating module power output in comparison to ANN predictions, with R^2 values of 0.9968 and 0.9962, and low MAEs of 1.156 and 1.242, respectively.

- For module temperature prediction, principal component analysis (PCA) indicated strong correlations among ambient air temperature, solar radiation, and operating temperature, with weaker correlations between operating temperature, wind speed, and relative humidity. Wind direction showed a particularly weak correlation.

- Evaluation of the predictions from all algorithms against experimental module temperature data revealed that ANNs possessed the best predictive proficiencies, attaining an R^2 of 0.986 and a low MAE of 0.982. The suggested model, along with kernel ridge regression (KRR) and gradient boosting algorithms, also demonstrated high accuracy in predicting module temperature.

- Generally, non-linear modeling outperformed linear modeling, providing superior accuracy due to greater flexibility and generalizability. The proposed model, built on these principles, proved to deliver better module temperature predictions compared to counterpart models from the literature.

- Upon developing and evaluating the proposed model, it was further examined for the estimation of the power generation of the photovoltaic module based on temperature predictions, utilizing an out-of-sample testing approach with entirely new datasets and yielding reasonable results.

- When comparing numerically estimated T_{back} from literature and experimental data, a strong agreement was observed, with greater accuracy and reduced error.

- Different parameters impacted T_{back} differently, where it appeared to scale in a linear way with ambient temperature T_a and solar radiation G, while a nonlinear decrease was noted with the increase in wind speed W_s.

- For average to high values of W_s, where forced convection mechanism is dominant, the influence of α, the angle of inclination, is insignificant, whereas if free convection dominated air flow, a fairly minor decrease in T_{back} is observed with the rise in α.

- The suggested regression model equation yielded highly accurate predictions, with a coefficient of determination (R^2) of 0.989, an adjusted and predicted R^2 values of 0.987, along with a MAE of 1.009, making it 10% more precise than the best tested model found in the literature.

- The suggested models are applicable for engineering tasks such as the estimation of power plant efficiency and calculations of power output in software dealing with photovoltaic systems. Nevertheless, additional tests and investigations are required for situations that are considerably different from those of the present study.

- Based on the principles of heat transfer and fluid dynamics, the suggested thermal model in the form of a simulation algorithm provided accurate predictions of T_{back}, as well as h_{conv} and h_{rad}. Additionally, calculating heat losses revealed that only 16% of solar radiation was converted to electricity, while the remainder was evacuated through radiation and convection at rates of 50% and 34%, respectively.

- Compared to measured data and models provided in literature, the T_{back} predicted via simulation exhibited an excellent alignment with measured data, establishing to be identified being among the most reliable approaches for modeling.

- In terms of statistical analysis, the simulation-based T_{back} produced an R^2 of 0.963, adjusted R^2 of 0.957, and a MAE of 1.883. In contrast, the King's model -as the best literature model- achieved an R^2 values of 0.973 and 0.966 for adjusted R^2, with a MAE of 1.663.

- Grounded on a thorough analysis, an explicit model that relates T_{cell} to T_a and G, similar to the Ross model, and using a determined coefficient k of 0.023, and another implicit model that incorporates the dynamical nature of the phenomena, demonstrating very practical performance.

Overall, the models for power output estimation established in this study, involving linear modeling, showed significantly improved performance and greater accuracy than those found in the existing literature. While these models demonstrate considerable accuracy and predictive capability, it was noted that non-linear machine learning algorithms exhibited superior abilities in uncovering underlying data structures and patterns. Therefore, a non-linear model was suggested, which closely approaches the performance of the ANN model, aligns well with measured data, and outperforms other machine learning algorithms, yielding very accurate results. Further analysis and testing in regions with significant climatic variability could be conducted, along with the consideration of more advanced machine learning algorithms.

Regarding module temperature modeling and calculations, detailed and comprehensive numerical simulations through CFD analysis were executed, leading to more precise estimations of module operating temperature. Each of the considered parameter exhibited unique effects on T_{back}, and based on these findings, a regression equation was established that offered an improved implementation and accurate prediction of the operating module temperature. Future studies may encompass additional aspects, such as varying ambient conditions, more modeling techniques, and other parameters including sun position (angle) and wind direction. Additionally, accurate temperature predictions have been achieved through the thermal modeling of photovoltaic modules, resulting in the proposal of new and accurate temperature models for engineering applications.

RECOMMENDATIONS AND PERSPECTIVE

The results reported in this work are limited to the scope of this study, and due to several limitations and obstacles observed during carrying out this work, such as the lack of measuring equipments, some areas for potential improvements and as future works can be drawn as follows:

- It is advised to conduct further investigations under conditions of significant climatic change, which may be considered in subsequent research.
- Future studies should explore more advanced machine learning techniques, such as deep learning models or ensemble methods, to potentially enhance predictive performance.
- Conducting studies in different geographical regions will allow validation of the models under varying environmental conditions, making them more globally applicable.
- Developing real-time monitoring systems that integrate these predictive models may optimize photovoltaic system efficiency in real-world applications.
- The solutions for temperature increase in photovoltaic modules can be addressed using some effective cooling techniques to improve their efficiency.
- An economical study is recommended as a future research direction to assess the financial viability of the proposed models, approaches and results.

REFERENCES

[1] C. C. A. C. D. National Oceanic and Atmospheric Administration, " Climate.gov. [Online]. Available: https://www.climate.gov/news-features/understanding-climate/climate-change-atmospheric-carbon-dioxide. Accessed: Oct. 4, 2024.

[2] I. E. Agency, "World Energy Outlook," 2023, www.iea.org.

[3] A.-R. E. U.S. Department of Commerce, " Trade.gov. [Online]. Available: https://www.trade.gov/country-commercial-guides/algeria-renewable-energy. Accessed: Oct. 4, 2024.

[4] R. E. a. E. E. D. P.-. Climate Policy Database, Algeria (2011)," Climate Policy Database.org. [Online]. Available: https://www.climatepolicydatabase.org/policies/renewable-energy-and-energy-efficiency-development-plan-2011-2030-algeria-2011. Accessed: Oct. 4, 2024.

[5] R. E. a. E. E. D. P.-. International Energy Agency, " IEA.org. [Online]. Available: https://www.iea.org/policies/6103-renewable-energy-and-energy-efficiency-development-plan-2015-2030. Accessed: Oct. 4, 2024.

[6] Y. Zahraoui, M. R. B. Khan, I. AlHamrouni, S. Mekhilef, and M. Ahmed, "Current status, scenario, and prospective of renewable energy in algeria: a review," *Energies,* vol. 14, p. 2354, 2021.

[7] A. E. O. U.S. Energy Information Administration, February 2021, www.eia.gov/aeo.

[8] M. Kanoğlu, Y. A. Çengel, and J. M. Cimbala, *Fundamentals and applications of renewable energy*: McGraw-Hill Education, 2020.

[9] S. A. Kalogirou, *Solar energy engineering: processes and systems*: Elsevier, 2023.

[10] T. B. Johansson, H. Kelly, A. K. Reddy, and R. H. Williams, "Renewable fuels and electricity for a growing world economy: defining and achieving the potential," *Energy Studies Review,* vol. 4, 1992.

[11] J. A. Duffie, W. A. Beckman, and N. Blair, *Solar engineering of thermal processes, photovoltaics and wind*: John Wiley & Sons, 2020.

[12] R. A. Messenger and A. Abtahi, *Photovoltaic systems engineering*: CRC press, 2018.

[13] Y. A. Çengel and A. J. Ghajar, *Heat and Mass Transfer: Fundamentals & Applications*: McGraw Hill Education, 2015.

[14] Y. A. Çengel, J. M. Cimbala, M. Kanoğlu, and R. H. Turner, *Fundamentals of Thermal-fluid Sciences*: McGraw-Hill Education, 2016.

[15] T. L. Bergman, *Fundamentals of heat and mass transfer*: John Wiley & Sons, 2011.

[16] D. Y. Goswami, *Principles of solar engineering*: CRC press, 2022.

[17] M. Hasanuzzaman, *Technologies for Solar Thermal Energy: Theory, Design And, Optimization*: Academic Press, 2022.

[18] L. Kumar, M. Hasanuzzaman, and N. Rahim, "Global advancement of solar thermal energy technologies for industrial process heat and its future prospects: A review," *Energy conversion and management,* vol. 195, pp. 885-908, 2019.

[19] G. Lorenzini, C. Biserni, and G. Flacco, *Solar thermal and biomass energy*: Wit Press, 2010.

[20] Y. Tian and C.-Y. Zhao, "A review of solar collectors and thermal energy storage in solar thermal applications," *Applied energy,* vol. 104, pp. 538-553, 2013.

[21] S. A. Kalogirou, S. Lloyd, J. Ward, and P. Eleftheriou, "Design and performance characteristics of a parabolic-trough solar-collector system," *Applied energy,* vol. 47, pp. 341-354, 1994.

[22] A. Mellit and S. Kalogirou, *Handbook of Artificial Intelligence Techniques in Photovoltaic Systems: Modeling, Control, Optimization, Forecasting and Fault Diagnosis*: Academic Press, 2022.

[23] G. N. Tiwari and S. Dubey, *Fundamentals of photovoltaic modules and their applications*: Royal Society of Chemistry, 2009.

[24] D. Govindasamy, F. Daniel, and A. Kumar, "Performance enhancement of photovoltaic system using composite phase change materials," *Energy,* vol. 288, p. 129871, 2024.

[25] A. Keddouda, R. Ihaddadene, A. Boukhari, A. Atia, M. Arıcı, N. Lebbihiat, *et al.*, "Solar photovoltaic power prediction using artificial neural network and multiple regression considering ambient and operating conditions," *Energy Conversion and Management,* vol. 288, p. 117186, 2023.

[26] X. Ma, M. Li, Y. Peng, L. Sun, and C. Chen, "Development of thermo–electrical loss model for photovoltaic module with inhomogeneous temperature," *Energy,* vol. 248, p. 123542, 2022.

[27] K. Hasan, S. B. Yousuf, M. S. H. K. Tushar, B. K. Das, P. Das, and M. S. Islam, "Effects of different environmental and operational factors on the PV performance: A comprehensive review," *Energy Science & Engineering,* vol. 10, pp. 656-675, 2022.

[28] R. Korab, M. Połomski, T. Naczyński, and T. Kandzia, "A dynamic thermal model for a photovoltaic module under varying atmospheric conditions," *Energy Conversion and Management,* vol. 280, p. 116773, 2023.

[29] E. Skoplaki and J. A. Palyvos, "On the temperature dependence of photovoltaic module electrical performance: A review of efficiency/power correlations," *Solar energy,* vol. 83, pp. 614-624, 2009.

[30] K. Vidyanandan, "An overview of factors affecting the performance of solar PV systems," *Energy Scan,* vol. 27, p. 216, 2017.

[31] Y. Abou Jieb and E. Hossain, "Photovoltaic Systems," 2022.

[32] A. K. Pandey, V. Tyagi, A. Jeyraj, L. Selvaraj, N. Rahim, and S. Tyagi, "Recent advances in solar photovoltaic systems for emerging trends and advanced applications," *Renewable and Sustainable Energy Reviews,* vol. 53, pp. 859-884, 2016.

[33] A. Luque and S. Hegedus, *Handbook of photovoltaic science and engineering*: John Wiley & Sons, 2011.

[34] A. Alcañiz, D. Grzebyk, H. Ziar, and O. Isabella, "Trends and gaps in photovoltaic power forecasting with machine learning," *Energy Reports,* vol. 9, pp. 447-471, 2023.

[35] L.-L. Li, S.-Y. Wen, M.-L. Tseng, and C.-S. Wang, "Renewable energy prediction: A novel short-term prediction model of photovoltaic output power," *Journal of Cleaner Production,* vol. 228, pp. 359-375, 2019.

[36] M. Trigo-González, F. Batlles, J. Alonso-Montesinos, P. Ferrada, J. Del Sagrado, M. Martínez-Durbán, *et al.*, "Hourly PV production estimation by means of an exportable multiple linear regression model," *Renewable Energy,* vol. 135, pp. 303-312, 2019.

[37] L. Liu, Y. Zhao, D. Chang, J. Xie, Z. Ma, Q. Sun, *et al.*, "Prediction of short-term PV power output and uncertainty analysis," *Applied energy,* vol. 228, pp. 700-711, 2018.

[38] W. Khan, S. Walker, and W. Zeiler, "Improved solar photovoltaic energy generation forecast using deep learning-based ensemble stacking approach," *Energy,* vol. 240, p. 122812, 2022.

[39] H. Mubarak, A. Hammoudeh, S. Ahmad, A. Abdellatif, S. Mekhilef, H. Mokhlis, *et al.*, "A hybrid machine learning method with explicit time encoding for improved Malaysian photovoltaic power prediction," *Journal of Cleaner Production,* p. 134979, 2022.

[40] C. Persson, P. Bacher, T. Shiga, and H. Madsen, "Multi-site solar power forecasting using gradient boosted regression trees," *Solar Energy,* vol. 150, pp. 423-436, 2017.

[41] J. Wang, P. Li, R. Ran, Y. Che, and Y. Zhou, "A short-term photovoltaic power prediction model based on the gradient boost decision tree," *Applied Sciences,* vol. 8, p. 689, 2018.

[42] J. Rosell and M. Ibanez, "Modelling power output in photovoltaic modules for outdoor operating conditions," *Energy conversion and management,* vol. 47, pp. 2424-2430, 2006.

[43] A. Mellit, S. Sağlam, and S. A. Kalogirou, "Artificial neural network-based model for estimating the produced power of a photovoltaic module," *Renewable Energy,* vol. 60, pp. 71-78, 2013.

[44] M. G. De Giorgi, P. M. Congedo, and M. Malvoni, "Photovoltaic power forecasting using statistical methods: impact of weather data," *IET Science, Measurement & Technology,* vol. 8, pp. 90-97, 2014.

[45] A. Dolara, F. Grimaccia, S. Leva, M. Mussetta, and E. Ogliari, "A physical hybrid artificial neural network for short term forecasting of PV plant power output," *Energies,* vol. 8, pp. 1138-1153, 2015.

[46] M. P. Almeida, O. Perpinan, and L. Narvarte, "PV power forecast using a nonparametric PV model," *Solar Energy,* vol. 115, pp. 354-368, 2015.

[47] I. Qasrawi and M. Awad, "Prediction of the power output of solar cells using neural networks: solar cells energy sector in Palestine," *International Journal of Computer Science and Security (IJCSS),* vol. 9, p. 280, 2015.

[48] G. Graditi, S. Ferlito, and G. Adinolfi, "Comparison of Photovoltaic plant power production prediction methods using a large measured dataset," *Renewable energy,* vol. 90, pp. 513-519, 2016.

[49] S. Pulipaka, F. Mani, and R. Kumar, "Modeling of soiled PV module with neural networks and regression using particle size composition," *Solar Energy,* vol. 123, pp. 116-126, 2016.

[50] S. Leva, A. Dolara, F. Grimaccia, M. Mussetta, and E. Ogliari, "Analysis and validation of 24 hours ahead neural network forecasting of photovoltaic output power," *Mathematics and computers in simulation,* vol. 131, pp. 88-100, 2017.

[51] L. Liu, D. Liu, Q. Sun, H. Li, and R. Wennersten, "Forecasting power output of photovoltaic system using a BP network method," *Energy Procedia,* vol. 142, pp. 780-786, 2017.

[52] S. Moslehi, T. A. Reddy, and S. Katipamula, "Evaluation of data-driven models for predicting solar photovoltaics power output," *Energy,* vol. 142, pp. 1057-1065, 2018.

[53] M. H. Alomari, J. Adeeb, and O. Younis, "Solar photovoltaic power forecasting in jordan using artificial neural networks," *International Journal of Electrical and Computer Engineering (IJECE),* vol. 8, pp. 497-497, 2018.

[54] M. K. Behera, I. Majumder, and N. Nayak, "Solar photovoltaic power forecasting using optimized modified extreme learning machine technique," *Engineering Science and Technology, an International Journal,* vol. 21, pp. 428-438, 2018.

[55] S. P. Durrani, S. Balluff, L. Wurzer, and S. Krauter, "Photovoltaic yield prediction using an irradiance forecast model based on multiple neural networks," *Journal of Modern Power Systems and Clean Energy,* vol. 6, pp. 255-267, 2018.

[56] I. Kayri and M. T. Gencoglu, "Predicting power production from a photovoltaic panel through artificial neural networks using atmospheric indicators," *Neural Computing and Applications,* vol. 31, pp. 3573-3586, 2019.

[57] D. A. R. de Jesús, P. Mandal, S. Chakraborty, and T. Senjyu, "Solar pv power prediction using a new approach based on hybrid deep neural network," in *2019 IEEE Power & Energy Society General Meeting (PESGM),* 2019, pp. 1-5.

[58] J. López Gómez, A. Ogando Martínez, F. Troncoso Pastoriza, L. Febrero Garrido, E. Granada Álvarez, and J. A. Orosa García, "Photovoltaic power prediction using artificial neural networks and numerical weather data," *Sustainability,* vol. 12, p. 10295, 2020.

[59] A. Erduman, "A smart short-term solar power output prediction by artificial neural network," *Electrical Engineering,* vol. 102, pp. 1441-1449, 2020.

[60] M. Wang, J. Peng, Y. Luo, Z. Shen, and H. Yang, "Comparison of different simplistic prediction models for forecasting PV power output: assessment with experimental measurements," *Energy,* vol. 224, p. 120162, 2021.

[61] M. Ayan and H. Toylan, "Estimating the power generating of a stand-alone solar photovoltaic panel using artificial neural networks and statistical methods," *Energy Sources, Part A: Recovery, Utilization, and Environmental Effects,* vol. 43, pp. 2496-2508, 2021.

[62] M. K. Park, J. M. Lee, W. H. Kang, J. M. Choi, and K. H. Lee, "Predictive model for PV power generation using RNN (LSTM)," *Journal of Mechanical Science and Technology,* vol. 35, pp. 795-803, 2021.

[63] A. Pamain, P. K. Rao, and F. N. Tilya, "Prediction of photovoltaic power output based on different non-linear autoregressive artificial neural network algorithms," *Global Energy Interconnection,* vol. 5, pp. 226-235, 2022.

[64] F. Rodríguez, A. Galarza, J. C. Vasquez, and J. M. Guerrero, "Using deep learning and meteorological parameters to forecast the photovoltaic generators intra-hour output power interval for smart grid control," *Energy,* vol. 239, p. 122116, 2022.

[65] S. Kallio and M. Siroux, "Photovoltaic power prediction for solar micro-grid optimal control," *Energy Reports,* vol. 9, pp. 594-601, 2023.

[66] L. Li, J. Cao, T. Hong, M. Lu, W. Zhao, and L. Fang, "Photovoltaic Power Prediction Based on Wavelet Analysis," in *International Conference On Signal And Information Processing, Networking And Computers*, 2022, pp. 216-222.

[67] S. Samara and E. Natsheh, "Modeling the output power of heterogeneous photovoltaic panels based on artificial neural networks using low cost microcontrollers," *Heliyon,* vol. 4, p. e00972, 2018.

[68] B. Zazoum, "Solar photovoltaic power prediction using different machine learning methods," *Energy Reports,* vol. 8, pp. 19-25, 2022.

[69] A. Olabi, M. A. Abdelkareem, C. Semeraro, M. Al Radi, H. Rezk, O. Muhaisen*, et al.*, "Artificial Neural Networks Applications in Partially Shaded PV Systems," *Thermal Science and Engineering Progress,* p. 101612, 2022.

[70] A. Mellit and A. M. Pavan, "Performance prediction of 20 kWp grid-connected photovoltaic plant at Trieste (Italy) using artificial neural network," *Energy Conversion and Management,* vol. 51, pp. 2431-2441, 2010.

[71] K. Narasimman, V. Gopalan, A. Bakthavatsalam, P. Elumalai, M. I. Shajahan, and J. J. Michael, "Modelling and real time performance evaluation of a 5 MW grid-connected solar photovoltaic plant using different artificial neural networks," *Energy Conversion and Management,* vol. 279, p. 116767, 2023.

[72] Y. Gong, Z. Wang, Z. Lai, and M. Jiang, "TVACPSO-assisted analysis of the effects of temperature and irradiance on the PV module performances," *Energy,* vol. 227, p. 120390, 2021.

[73] E. Skoplaki and J. A. Palyvos, "Operating temperature of photovoltaic modules: A survey of pertinent correlations," *Renewable energy,* vol. 34, pp. 23-29, 2009.

[74] S. Kaplanis and E. Kaplani, "A new dynamic model to predict transient and steady state PV temperatures taking into account the environmental conditions," *Energies,* vol. 12, p. 2, 2018.

[75] D. T. Lobera and S. Valkealahti, "Dynamic thermal model of solar PV systems under varying climatic conditions," *Solar energy,* vol. 93, pp. 183-194, 2013.

[76] G. Osma-Pinto and G. Ordóñez-Plata, "Dynamic thermal modelling for the prediction of the operating temperature of a PV panel with an integrated cooling system," *Renewable Energy,* vol. 152, pp. 1041-1054, 2020.

[77] N. Bailek, K. Bouchouicha, M. A. Hassan, A. Slimani, and B. Jamil, "Implicit regression-based correlations to predict the back temperature of PV modules in the arid region of south Algeria," *Renewable Energy,* vol. 156, pp. 57-67, 2020.

[78] X.-J. Dong, J.-N. Shen, G.-X. He, Z.-F. Ma, and Y.-J. He, "A general radial basis function neural network assisted hybrid modeling method for photovoltaic cell operating temperature prediction," *Energy,* vol. 234, p. 121212, 2021.

[79] A. Muzathik, "Photovoltaic modules operating temperature estimation using a simple correlation," *International Journal of Energy Engineering,* vol. 4, p. 151, 2014.

[80] D. P. N. Nguyen, K. Neyts, and J. Lauwaert, "Proposed Models to Improve Predicting the Operating Temperature of Different Photovoltaic Module Technologies under Various Climatic Conditions," *Applied Sciences,* vol. 11, p. 7064, 2021.

[81] A. Ziane, R. Dabou, A. Necaibia, N. Sahouane, M. Mostefaoui, A. Bouraiou, *et al.*, "Tree-based ensemble methods for predicting the module temperature of a grid-tied photovoltaic system in the desert," *International Journal of Green Energy,* vol. 18, pp. 1430-1440, 2021.

[82] S. P. Aly, S. Ahzi, N. Barth, and A. Abdallah, "Using energy balance method to study the thermal behavior of PV panels under time-varying field conditions," *Energy Conversion and Management,* vol. 175, pp. 246-262, 2018.

[83] M. Prilliman, J. S. Stein, D. Riley, and G. Tamizhmani, "Transient weighted moving-average model of photovoltaic module back-surface temperature," *IEEE Journal of Photovoltaics,* vol. 10, pp. 1053-1060, 2020.

[84] J. Zhou, Q. Yi, Y. Wang, and Z. Ye, "Temperature distribution of photovoltaic module based on finite element simulation," *Solar Energy,* vol. 111, pp. 97-103, 2015.

[85] M. Abdolzadeh and T. Zarei, "Optical and thermal modeling of a photovoltaic module and experimental evaluation of the modeling performance," *Environmental Progress & Sustainable Energy,* vol. 36, pp. 277-293, 2017.

[86] A. Gholami, M. Ameri, M. Zandi, and R. G. Ghoachani, "Electrical, thermal and optical modeling of photovoltaic systems: Step-by-step guide and comparative review study," *Sustainable Energy Technologies and Assessments,* vol. 49, p. 101711, 2022.

[87] W. Gu, X. Wang, and X. Bai, "Coupled optical-electrical-thermal loss modelling and energy distributions of a photovoltaic module," *Energy Conversion and Management,* vol. 276, p. 116476, 2023.

[88] A. Hassan, S. Abbas, S. Yousuf, F. Abbas, N. Amin, S. Ali*, et al.*, "An experimental and numerical study on the impact of various parameters in improving the heat transfer performance characteristics of a water based photovoltaic thermal system," *Renewable Energy,* vol. 202, pp. 499-512, 2023.

[89] R. Ross Jr, "Interface design considerations for terrestrial solar cell modules," in *12th Photovoltaic Specialists Conference*, 1976, pp. 801-806.

[90] T. Nordmann and L. Clavadetscher, "Understanding temperature effects on PV system performance," in *3rd World Conference onPhotovoltaic Energy Conversion, 2003. Proceedings of*, 2003, pp. 2243-2246.

[91] J. W. Stultz, "Thermal and other tests of photovoltaic modules performed in natural sunlight," *Journal of Energy,* vol. 3, pp. 363-372, 1979.

[92] J. D. Mondol, Y. Yohanis, M. Smyth, and B. Norton, "Long-term validated simulation of a building integrated photovoltaic system," *Solar energy,* vol. 78, pp. 163-176, 2005.

[93] J. D. Mondol, Y. G. Yohanis, and B. Norton, "The effect of low insolation conditions and inverter oversizing on the long-term performance of a grid-connected photovoltaic system," *Progress in Photovoltaics: Research and Applications,* vol. 15, pp. 353-368, 2007.

[94] J. D. Mondol, Y. G. Yohanis, and B. Norton, "Comparison of measured and predicted long term performance of grid a connected photovoltaic system," *Energy conversion and management,* vol. 48, pp. 1065-1080, 2007.

[95] T. Schott, "Operation temperatures of pv modules: a theoretical and experimental approach," in *EC Photovoltaic solar energy conference. 6*, 1985, pp. 392-396.

[96] W. Durisch, B. Bitnar, J.-C. Mayor, H. Kiess, K.-h. Lam, and J. Close, "Efficiency model for photovoltaic modules and demonstration of its application to energy yield estimation," *Solar energy materials and solar cells,* vol. 91, pp. 79-84, 2007.

[97] J.-M. SERVANT, "Calculation of the cell temperature for photovoltaic modules from climatic data," in *Intersol Eighty Five*, ed: Elsevier, 1986, pp. 1640-1643.

[98] F. Lasnier, *Photovoltaic engineering handbook*: CRC Press, 1990.

[99] D. L. King, "Photovoltaic module and array performance characterization methods for all system operating conditions," in *AIP conference proceedings*, 1997, pp. 347-368.

[100] D. L. King, J. A. Kratochvil, and W. E. Boyson, "Field experience with a new performance characterization procedure for photovoltaic arrays," Sandia National Lab.(SNL-NM), Albuquerque, NM (United States)1997.

[101] G. TamizhMani, L. Ji, Y. Tang, L. Petacci, and C. Osterwald, "Photovoltaic module thermal/wind performance: long-term monitoring and model development for energy

rating," in *NCPV and Solar Program Review Meeting Proceedings, 24-26 March 2003, Denver, Colorado (CD-ROM)*, 2003.

[102] D. L. King, J. A. Kratochvil, and W. E. Boyson, *Photovoltaic array performance model* vol. 8: Citeseer, 2004.

[103] S. Kurtz, K. Whitfield, D. Miller, J. Joyce, J. Wohlgemuth, M. Kempe, *et al.*, "Evaluation of high-temperature exposure of rack-mounted photovoltaic modules," in *2009 34th IEEE Photovoltaic Specialists Conference (PVSC)*, 2009, pp. 002399-002404.

[104] E. Skoplaki, A. Boudouvis, and J. Palyvos, "A simple correlation for the operating temperature of photovoltaic modules of arbitrary mounting," *Solar energy materials and solar cells,* vol. 92, pp. 1393-1402, 2008.

[105] M. Koehl, M. Heck, S. Wiesmeier, and J. Wirth, "Modeling of the nominal operating cell temperature based on outdoor weathering," *Solar Energy Materials and Solar Cells,* vol. 95, pp. 1638-1646, 2011.

[106] M. Almaktar, H. A. Rahman, M. Y. Hassan, and S. Rahman, "Climate-based empirical model for PV module temperature estimation in tropical environment," *Applied Solar Energy,* vol. 49, pp. 192-201, 2013.

[107] S. Kaplanis, E. Kaplani, and J. Kaldellis, "PV temperature and performance prediction in free-standing, BIPV and BAPV incorporating the effect of temperature and inclination on the heat transfer coefficients and the impact of wind, efficiency and ageing," *Renewable Energy,* vol. 181, pp. 235-249, 2022.

[108] İ. Ceylan, O. Erkaymaz, E. Gedik, and A. E. Gürel, "The prediction of photovoltaic module temperature with artificial neural networks," *Case Studies in Thermal Engineering,* vol. 3, pp. 11-20, 2014.

[109] C. COSKUN, N. Koçyiğit, and Z. OKTAY, "Estimation of pv module surface temperature using artificial neural networks," *Mugla Journal of Science and Technology,* vol. 2, pp. 15-18, 2016.

[110] A. Sohani and H. Sayyaadi, "Employing genetic programming to find the best correlation to predict temperature of solar photovoltaic panels," *Energy Conversion and Management,* vol. 224, p. 113291, 2020.

[111] X.-J. Dong, J.-N. Shen, Z.-F. Ma, and Y.-J. He, "Simultaneous operating temperature and output power prediction method for photovoltaic modules," *Energy,* vol. 260, p. 124909, 2022.

[112] A. H. Shiravi, M. Firoozzadeh, and M. Lotfi, "Experimental study on the effects of air blowing and irradiance intensity on the performance of photovoltaic modules, using central composite design," *Energy,* vol. 238, p. 121633, 2022.

[113] N. Dabaghzadeh and M. Eslami, "Temperature distribution in a photovoltaic module at various mounting and wind conditions: a complete CFD modeling," *Journal of Renewable and Sustainable Energy,* vol. 11, 2019.

[114] M. Jaszczur, J. Teneta, Q. Hassan, E. Majewska, and R. Hanus, "An experimental and numerical investigation of photovoltaic module temperature under varying environmental conditions," *Heat Transfer Engineering,* vol. 42, pp. 354-367, 2021.

[115] H. Lu and W. Zhao, "CFD prediction of dust pollution and impact on an isolated ground-mounted solar photovoltaic system," *Renewable Energy,* vol. 131, pp. 829-840, 2019.

[116] M. Herrando, G. Fantoni, A. Cubero, R. Simón-Allué, I. Guedea, and N. Fueyo, "Numerical analysis of the fluid flow and heat transfer of a hybrid PV-thermal collector and performance assessment," *Renewable Energy,* vol. 209, pp. 122-132, 2023.

[117] M. A. Yildirim and A. Cebula, "A numerical and experimental analysis of a novel highly-efficient water-based PV/T system," *Energy,* vol. 289, p. 129875, 2024.

[118] A. Abiola-Ogedengbe, H. Hangan, and K. Siddiqui, "Experimental investigation of wind effects on a standalone photovoltaic (PV) module," *Renewable Energy,* vol. 78, pp. 657-665, 2015.

[119] M. G. Chowdhury, D. Goossens, H. Goverde, and F. Catthoor, "Experimentally validated CFD simulations predicting wind effects on photovoltaic modules mounted on inclined surfaces," *Sustainable Energy Technologies and Assessments,* vol. 30, pp. 201-208, 2018.

[120] T. Hove, "A method for predicting long-term average performance of photovoltaic systems," *Renewable Energy,* vol. 21, pp. 207-229, 2000.

[121] M. Mattei, G. Notton, C. Cristofari, M. Muselli, and P. Poggi, "Calculation of the polycrystalline PV module temperature using a simple method of energy balance," *Renewable energy,* vol. 31, pp. 553-567, 2006.

[122] A. Tiwari and M. Sodha, "Performance evaluation of solar PV/T system: an experimental validation," *Solar energy,* vol. 80, pp. 751-759, 2006.

[123] A. Tiwari and M. Sodha, "Performance evaluation of hybrid PV/thermal water/air heating system: a parametric study," *Renewable energy,* vol. 31, pp. 2460-2474, 2006.

[124] L. Migliorini, L. Molinaroli, R. Simonetti, and G. Manzolini, "Development and experimental validation of a comprehensive thermoelectric dynamic model of photovoltaic modules," *Solar Energy,* vol. 144, pp. 489-501, 2017.

[125] M. Akhsassi, A. El Fathi, N. Erraissi, N. Aarich, A. Bennouna, M. Raoufi, *et al.*, "Experimental investigation and modeling of the thermal behavior of a solar PV module," *Solar Energy Materials and Solar Cells,* vol. 180, pp. 271-279, 2018.

[126] P. Bevilacqua, R. Bruno, A. Rollo, and V. Ferraro, "A novel thermal model for PV panels with back surface spray cooling," *Energy,* vol. 255, p. 124401, 2022.

[127] W. Gu, T. Ma, L. Shen, M. Li, Y. Zhang, and W. Zhang, "Coupled electrical-thermal modelling of photovoltaic modules under dynamic conditions," *Energy,* vol. 188, p. 116043, 2019.

[128] T. Ma, Z. Guo, L. Shen, X. Liu, Z. Chen, Y. Zhou, *et al.*, "Performance modelling of photovoltaic modules under actual operating conditions considering loss mechanism and energy distribution," *Applied Energy,* vol. 298, p. 117205, 2021.

[129] H. Goverde, D. Goossens, J. Govaerts, V. Dubey, F. Catthoor, K. Baert, *et al.*, "Spatial and temporal analysis of wind effects on PV module temperature and performance," *Sustainable Energy Technologies and Assessments,* vol. 11, pp. 36-41, 2015.

[130] E. Kaplani and S. Kaplanis, "Thermal modelling and experimental assessment of the dependence of PV module temperature on wind velocity and direction, module orientation and inclination," *Solar Energy,* vol. 107, pp. 443-460, 2014.

[131] C. Schwingshackl, M. Petitta, J. E. Wagner, G. Belluardo, D. Moser, M. Castelli, *et al.*, "Wind effect on PV module temperature: Analysis of different techniques for an accurate estimation," *Energy Procedia,* vol. 40, pp. 77-86, 2013.

[132] P. A. Mirzaei and R. Zhang, "Validation of a climatic CFD model to predict the surface temperature of building integrated photovoltaics," *Energy Procedia,* vol. 78, pp. 1865-1870, 2015.

[133] D. Roeleveld, G. Hailu, A. Fung, D. Naylor, T. Yang, and A. Athienitis, "Validation of computational fluid dynamics (CFD) model of a building integrated photovoltaic/thermal (BIPV/T) system," *Energy Procedia,* vol. 78, pp. 1901-1906, 2015.

[134] R. Zhang, P. A. Mirzaei, and J. Carmeliet, "Prediction of the surface temperature of building-integrated photovoltaics: Development of a high accuracy correlation using computational fluid dynamics," *Solar Energy,* vol. 147, pp. 151-163, 2017.

[135] T. Schott, "Operation temperatures of pv modules: a theoretical and experimental approach," in *EC Photovoltaic solar energy conference.*, 1985, pp. 392-396.

[136] M. W. Davis, A. H. Fanney, and B. P. Dougherty, "Prediction of building integrated photovoltaic cell temperatures," *J. Sol. Energy Eng.*, vol. 123, pp. 200-210, 2001.

[137] V. L. Brano, G. Ciulla, V. Franzitta, and A. Viola, "A novel implicit correlation for the operative temperature of a PV panel," *AASRI Procedia,* vol. 2, pp. 112-120, 2012.

[138] N. Lebbihiat, A. Atia, M. Arıcı, and N. Meneceur, "Geothermal energy use in Algeria: A review on the current status compared to the worldwide, utilization opportunities and countermeasures," *Journal of Cleaner Production,* vol. 302, p. 126950, 2021.

[139] S. Rosiek, J. Alonso-Montesinos, and F. Batlles, "Online 3-h forecasting of the power output from a BIPV system using satellite observations and ANN," *International Journal of Electrical Power & Energy Systems,* vol. 99, pp. 261-272, 2018.

[140] J. E. Gentle, W. K. Härdle, and Y. Mori, "Springer Handbooks of Computational Statistics," 2012.

[141] A. Pawlowski, J. L. Guzmán, F. Rodríguez, M. Berenguel, and J. Sánchez, "Application of time-series methods to disturbance estimation in predictive control problems," in *2010 IEEE International Symposium on Industrial Electronics*, 2010, pp. 409-414.

[142] W. Dai, S. Cremaschi, H. J. Subramani, and H. Gao, "Estimation of data uncertainty in the absence of replicate experiments," *Chemical Engineering Research and Design,* vol. 147, pp. 187-199, 2019.

[143] B. Butcher and B. J. Smith, "Feature Engineering and Selection: A Practical Approach for Predictive Models: by Max Kuhn and Kjell Johnson. Boca Raton, FL: Chapman & Hall/CRC Press, 2019, xv+ 297 pp., $79.95 (H), ISBN: 978-1-13-807922-9," ed: Taylor & Francis, 2020.

[144] H. Chen and X. Chang, "Photovoltaic power prediction of LSTM model based on Pearson feature selection," *Energy Reports,* vol. 7, pp. 1047-1054, 2021.

[145] A. Keddouda, R. Ihaddadene, A. Boukhari, A. Atia, M. Arıcı, N. Lebbihiat*, et al.*, "Photovoltaic module temperature prediction using various machine learning algorithms: Performance evaluation," *Applied Energy,* vol. 363, p. 123064, 2024.

[146] J. O. Rawlings, S. G. Pantula, and D. A. Dickey, *Applied regression analysis: a research tool*: Springer, 1998.

[147] R. R. Rhinehart, *Nonlinear regression modeling for engineering applications: modeling, model validation, and enabling design of experiments*: John Wiley & Sons, 2016.

[148] N. Matloff, *Statistical regression and classification: from linear models to machine learning*: CRC Press, 2017.

[149] A. E. Hoerl and R. W. Kennard, "Ridge regression: Biased estimation for nonorthogonal problems," *Technometrics,* vol. 12, pp. 55-67, 1970.

[150] B. Schölkopf, Z. Luo, and V. Vovk, *Empirical inference: Festschrift in honor of Vladimir N. Vapnik*: Springer Science & Business Media, 2013.

[151] F. Douak, F. Melgani, and N. Benoudjit, "Kernel ridge regression with active learning for wind speed prediction," *Applied energy,* vol. 103, pp. 328-340, 2013.

[152] N. Cristianini and J. Shawe-Taylor, *An introduction to support vector machines and other kernel-based learning methods*: Cambridge university press, 2000.

[153] R. Tibshirani, "Regression shrinkage and selection via the lasso," *Journal of the Royal Statistical Society Series B: Statistical Methodology,* vol. 58, pp. 267-288, 1996.

[154] S. L. Brunton and J. N. Kutz*, Data-driven science and engineering: Machine learning, dynamical systems, and control*: Cambridge University Press, 2022.

[155] H. Zou and T. Hastie, "Regularization and variable selection via the elastic net," *Journal of the Royal Statistical Society Series B: Statistical Methodology,* vol. 67, pp. 301-320, 2005.

[156] E. Pekel, "Estimation of soil moisture using decision tree regression," *Theoretical and Applied Climatology,* vol. 139, pp. 1111-1119, 2020.

[157] W. Y. Loh, "Classification and regression trees," *Wiley interdisciplinary reviews: data mining and knowledge discovery,* vol. 1, pp. 14-23, 2011.

[158] L. Breiman, "Random forests," *Machine learning,* vol. 45, pp. 5-32, 2001.

[159] A. Liaw and M. Wiener, "Classification and regression by randomForest," *R news,* vol. 2, pp. 18-22, 2002.

[160] J. H. Friedman, "Greedy function approximation: a gradient boosting machine," *Annals of statistics,* pp. 1189-1232, 2001.

[161] J. H. Friedman, "Stochastic gradient boosting," *Computational statistics & data analysis,* vol. 38, pp. 367-378, 2002.

[162] H. Drucker, C. J. Burges, L. Kaufman, A. Smola, and V. Vapnik, "Support vector regression machines," *Advances in neural information processing systems,* vol. 9, 1996.

[163] C. Cortes and V. Vapnik, "Support-vector networks," *Machine learning,* vol. 20, pp. 273-297, 1995.

[164] J. Hu, J. Hu, H. Lin, X. Li, C. Jiang, X. Qiu, *et al.,* "State-of-charge estimation for battery management system using optimized support vector machine for regression," *Journal of Power Sources,* vol. 269, pp. 682-693, 2014.

[165] R. De Leone, M. Pietrini, and A. Giovannelli, "Photovoltaic energy production forecast using support vector regression," *Neural Computing and Applications,* vol. 26, pp. 1955-1962, 2015.

[166] J. Platt, "Sequential minimal optimization: A fast algorithm for training support vector machines," 1998.

[167] K. Suzuki, *Artificial neural networks: methodological advances and biomedical applications*: BoD–Books on Demand, 2011.

[168] A. T. Mohammad, H. M. Hussen, and H. J. Akeiber, "Prediction of the output power of photovoltaic module using artificial neural networks model with optimizing the neurons number," *International Journal of Renewable Energy Development,* vol. 12, 2023.

[169] C. K. Williams and C. E. Rasmussen, *Gaussian processes for machine learning* vol. 2: MIT press Cambridge, MA, 2006.

[170] K. P. Murphy, *Probabilistic machine learning: an introduction*: MIT press, 2022.

[171] A. Keddouda, R. Ihaddadene, A. Boukhari, A. Atia, M. Arıcı, N. Lebbihiat, *et al.,* "Experimental and numerical modeling of photovoltaic modules temperature under varying ambient conditions," *Energy Conversion and Management,* vol. 312, p. 118563, 2024.

[172] M. Ouzzane, P. Eslami-Nejad, M. Badache, and Z. Aidoun, "New correlations for the prediction of the undisturbed ground temperature," *Geothermics,* vol. 53, pp. 379-384, 2015.

[173] ANSYS, *ANSYS Fluent Theory Guide,* ANSYS Inc ed., 2018.

[174] A. Keddouda, R. Ihaddadene, A. Boukhari, A. Atia, M. Arıcı, N. Lebbihiat, *et al.,* "Experimentally validated thermal modeling for temperature prediction of photovoltaic

modules under variable environmental conditions," *Renewable Energy,* vol. 231, p. 120922, 2024.

[175] Y. A. Çengel and J. M. Cimbala, "Fluid Mechanics: Fundamentals and Applications, Forth Edition," ed: New York: McGraw-Hill Education, 2018.

[176] E. Sparrow and K. Tien, "Forced convection heat transfer at an inclined and yawed square plate—application to solar collectors," 1977.

[177] E. M. Sparrow, J. Ramsey, and E. Mass, "Effect of finite width on heat transfer and fluid flow about an inclined rectangular plate," 1979.

[178] F. Test, R. Lessmann, and A. Johary, "Heat transfer during wind flow over rectangular bodies in the natural environment," *J. Heat Transfer* pp. 262–267, 1981.

[179] S. Kumar, V. Sharma, T. Kandpal, and S. Mullick, "Wind induced heat losses from outer cover of solar collectors," *Renewable Energy,* vol. 10, pp. 613-616, 1997.

[180] S. Jayamaha, N. Wijeysundera, and S. Chou, "Measurement of the heat transfer coefficient for walls," *Building and Environment,* vol. 31, pp. 399-407, 1996.

[181] E. Sartori, "Convection coefficient equations for forced air flow over flat surfaces," *Solar Energy,* vol. 80, pp. 1063-1071, 2006.

[182] J. Palyvos, "A survey of wind convection coefficient correlations for building envelope energy systems' modeling," *Applied thermal engineering,* vol. 28, pp. 801-808, 2008.

[183] W. H. McAdams, *Heat transmission,* Third ed. ed. Tokyo, Japan: McGraw-Hill, 1954.

[184] J. DW and P. WWS C, "Solar and wind induced external coefficients for solar collectors. Coop Mediterr Pour l'Energie Solaire," *Rev Int d'Heliotechnique,* vol. 2, p. 56, 1977.

[185] S. Sharples and P. Charlesworth, "Full-scale measurements of wind-induced convective heat transfer from a roof-mounted flat plate solar collector," *Solar Energy,* vol. 62, pp. 69-77, 1998.

[186] S. Kumar and S. Mullick, "Wind heat transfer coefficient in solar collectors in outdoor conditions," *Solar energy,* vol. 84, pp. 956-963, 2010.

[187] S. Shakerin, "Wind-related heat transfer coefficient for flat-plate solar collectors," 1987.

[188] Y. A. Çengel and A. J. Ghajar, *Heat and Mass Transfer: Fundamentals and Applications,* SIXTH EDITION ed.: McGraw-Hill Education 2020.

[189] S. W. Churchill and H. H. Chu, "Correlating equations for laminar and turbulent free convection from a vertical plate," *International journal of heat and mass transfer,* vol. 18, pp. 1323-1329, 1975.

[190] T. Fujii and H. Imura, "Natural-convection heat transfer from a plate with arbitrary inclination," *International journal of heat and mass transfer,* vol. 15, pp. 755-767, 1972.

[191] A. Bejan and A. D. Kraus, *Heat transfer handbook* vol. 1: John Wiley & Sons, 2003.

[192] Y. Cengel, J. Cimbala, and R. Turner, *Fundamentals of Thermal-Fluid Sciences*, FIFTH EDITION ed.: McGraw Hill, 2017.

[193] S. Armstrong and W. Hurley, "A thermal model for photovoltaic panels under varying atmospheric conditions," *Applied thermal engineering*, vol. 30, pp. 1488-1495, 2010.

[194] E. Kaplani and S. Kaplanis, "PV module temperature prediction at any environmental conditions and mounting configurations," in *Renewable Energy and Sustainable Buildings: Selected Papers from the World Renewable Energy Congress WREC 2018*, 2020, pp. 921-933.

[195] S. L. Brunton and J. N. Kutz, *Data-driven science and engineering: Machine learning, dynamical systems, and control*: Cambridge University Press, 2019.

[196] A. K. Vyas, S. Balamurugan, K. K. Hiran, and H. S. Dhiman, *Artificial Intelligence for Renewable Energy Systems*: John Wiley & Sons, 2022.

[197] S. Al-Dahidi, O. Ayadi, J. Adeeb, and M. Louzazni, "Assessment of artificial neural networks learning algorithms and training datasets for solar photovoltaic power production prediction," *Frontiers in energy research*, vol. 7, p. 130, 2019.

[198] R. Rawat, S. Kaushik, and R. Lamba, "A review on modeling, design methodology and size optimization of photovoltaic based water pumping, standalone and grid connected system," *Renewable and Sustainable Energy Reviews*, vol. 57, pp. 1506-1519, 2016.

[199] C. Hajjaj, A. A. Merrouni, A. Bouaichi, M. Benhmida, S. Sahnoun, A. Ghennioui, *et al.*, "Evaluation, comparison and experimental validation of different PV power prediction models under semi-arid climate," *Energy Conversion and Management*, vol. 173, pp. 476-488, 2018.

[200] A. C. Rakhimov, D. Visser, and E. Komen, "Uncertainty Quantification method for CFD applied to the turbulent mixing of two water layers," *Nuclear Engineering and Design*, vol. 333, pp. 1-15, 2018.

[201] L. Deville, M. Theristis, B. H. King, T. L. Chambers, and J. S. Stein, "Open-source photovoltaic model pipeline validation against well-characterized system data," *Progress in Photovoltaics: Research and Applications*, 2023.

[202] M. Dörenkämper, M. M. de Jong, J. Kroon, V. S. Nysted, J. Selj, and T. Kjeldstad, "Modeled and Measured Operating Temperatures of Floating PV Modules: A Comparison," *Energies*, vol. 16, p. 7153, 2023.

[203] A. Mermoud and B. Wittmer, "PVSYST user’s manual," *Switzerland, January*, 2014.

APPENDICES

Appendix A

A.1 Data acquisition system

A.1.1 Solar radiation logger

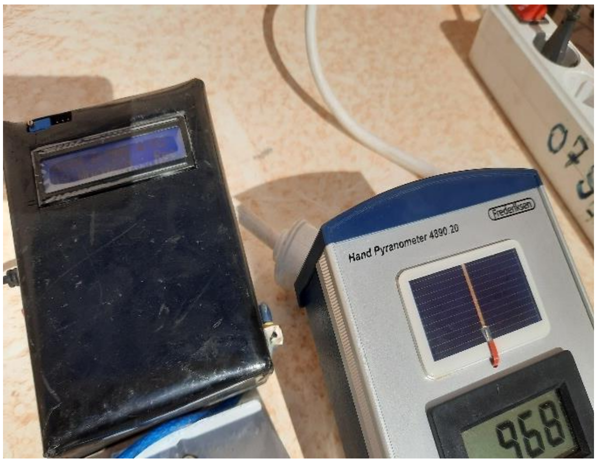

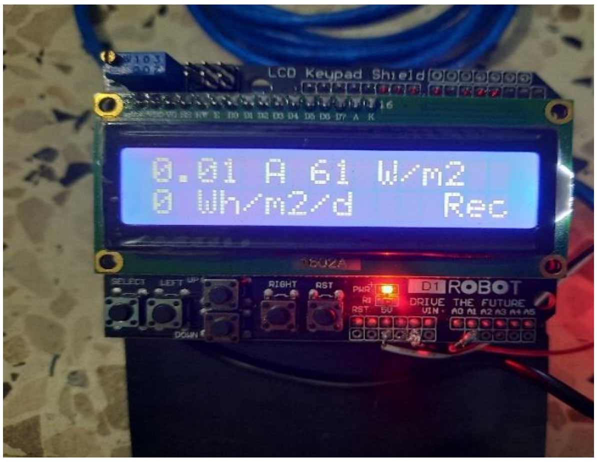

A.1.2 Temperature logger

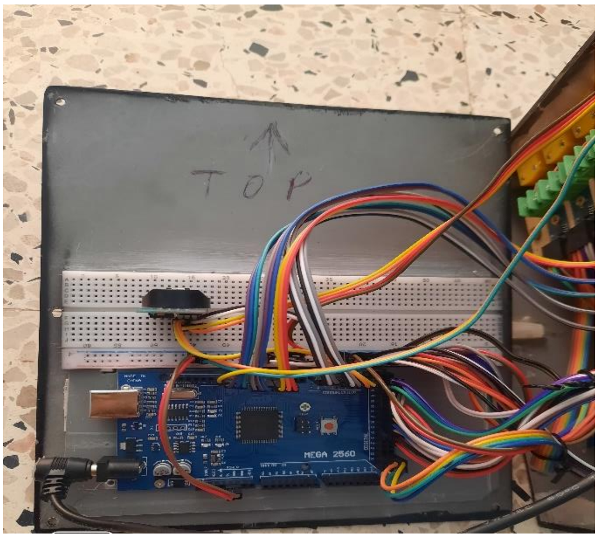

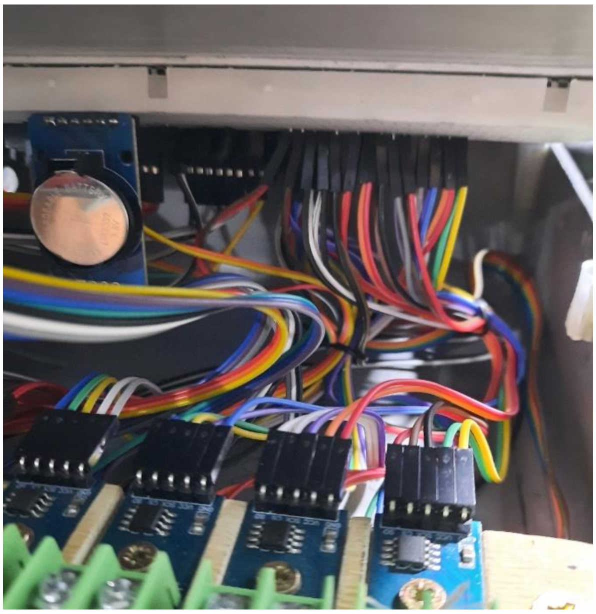

A.1.3 Wind speed and direction recorder

A.1.4 Photovoltaic power output recorder

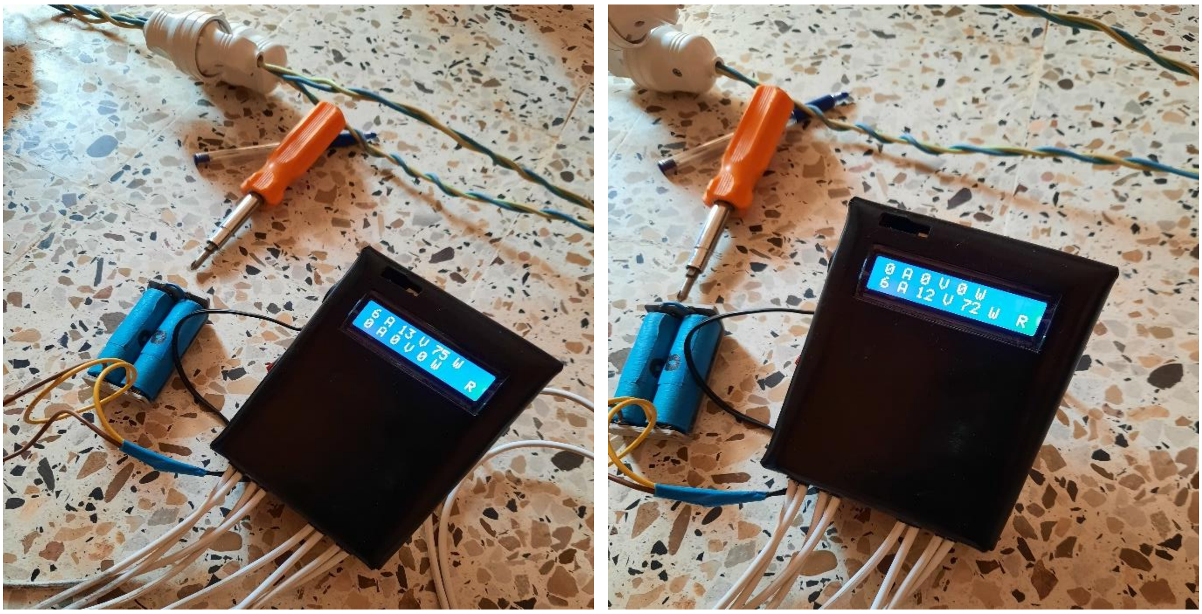

A.2 Location of experiments

Figure A.1: Experiments location

A.3 Mechanical characteristics of Photovoltaic modules

Table A.1: Mechanical characteristics of the photovoltaic module.

Characteristic	Value
Type of Cell	Polycrystalline 156×156
Cell array and number	4×9 (36 Pcs)
Dimensions	1480×669×35
Weight	12.0 Kg
Front glass	3.2mm Tempered Glass
Frame	Anodized Aluminium Alloy
Encapsulation	Glass/EVA/Cells/EVA/TPT
Relative humidity	0 to 100%
Resistance	-40°C to +85°C
Wind and snow load parameter	5400 Pa

Appendix B

B.1 Energy gap of some semiconductors

Table B.1: Energy Gap for Some Candidate Materials for PV Cells

Material	Band Gap (eV)
Si	1.11
SiC	2.6
$CdAs_2$	1
CdTe	1.44
CdSe	1.74
CdS	2.42
$CdSnO_4$	2.9
GaAs	1.4
GaP	2.24
Cu_2S	1.8
CuO	2
Cu_2Se	1.4
$CuInS_2$	1.5
$CuInSe_2$	1.01
$CuInTe_2$	0.9
InP	1.27
In_2Te_3	1.2
In_2O_3	2.8
Zn_3P_2	1.6
ZnTe	2.2
ZnSe	2.6
AlP	2.43
AlSb	1.63
As_2Se_3	1.6
Sb_2Se_3	1.2
Ge	0.67
Se	1.6

Appendix C

C.1 Scientific production and publications

C.1.1 Papers

A. Keddouda, R. Ihaddadene, A. Boukhari, A. Atia, M. Arıcı, N. Lebbihiat, et al., "Solar photovoltaic power prediction using artificial neural network and multiple regression considering ambient and operating conditions," Energy Conversion and Management, vol. 288, p. 117186, 2023.

A. Keddouda, R. Ihaddadene, A. Boukhari, A. Atia, M. Arıcı, N. Lebbihiat, et al., "Photovoltaic module temperature prediction using various machine learning algorithms: Performance evaluation," Applied Energy, vol. 363, p. 123064, 2024.

A. Keddouda, R. Ihaddadene, A. Boukhari, A. Atia, M. Arıcı, N. Lebbihiat, et al., "Experimental and numerical modeling of photovoltaic modules temperature under varying ambient conditions," Energy Conversion and Management, vol. 312, p. 118563, 2024.

A. Keddouda, R. Ihaddadene, A. Boukhari, A. Atia, M. Arıcı, N. Lebbihiat, et al., "Experimentally validated thermal modeling for temperature prediction of photovoltaic modules under variable environmental conditions," Renewable Energy, vol. 231, p. 120922, 2024.

C.1.2 International conferences

A. Keddouda, R. Ihaddadene, G. Belhi, N. Ihaddadene, H. Ahmed, T. Nedhirou, et al., "Experimental Evaluation of Explicit and Implicit Models in Prediction of PV Module Temperature," presented at the 7th Virtual International Conference on Science, Technology and Management in Energy, Belgrade, Serbia, 2021.

A. Keddouda, R. Ihaddadene, A. Boukhari, A. Atia, and N. Lebbihiat, "Modeling and prediction of photovoltaic power output using artificial neural network considering ambient conditions," 1st International Conference on Trends and Innovations in Smart Technologies (ICTIST) London, UK, October 7-8, 2022.

A. Keddouda, R. Ihaddadene, A. Boukhari, A. Atia, and N. Lebbihiat, "Solar photovoltaic power prediction using artificial neural networks," 1st International Conference on Optoelectronic, Materials & Renewable Energy ICOMRE’22, University of El Oued, December, 2022.

A. Keddouda, R. Ihaddadene, A. Boukhari, A. Atia, and N. Lebbihiat, "Data-Driven Models for Power Output Prediction of Photovoltaic Modules: Machine Learning Algorithms’ Evaluation and Comparison," 2nd International Conference on Materials, Energy and Environment (ICMEE) 23 – 24 October 2023, El Oued, Algeria.

A. Keddouda, R. Ihaddadene, A. Boukhari, A. Atia, and N. Lebbihiat, "CFD Based and Machine Learning Modeling and Prediction of Photovoltaic Modules’ Temperature and Power Output," International Pluridisciplinary PhD Meeting (IPPM’23) 2nd Edition, University of El Oued, December 11-13, 2023.

C.2 Simulation algorithm

The full code developed for the predictive simulation algorithm for the calculation of module temperature described in this thesis (III.3 Thermal modeling) is extensive to include but it is available upon request. Please contact the author at abdelhak.keddouda@gmail.com; abdelhak.keddouda@univ-msila.dz; for access.

Thème de Thèse : Etude de transfert de chaleur dans un panneau photovoltaïque (PV)
Auteurs : Abdelhak Keddouda, Département de génie mécanique, Université de M’Sila.
Spécialité : Energétique.

Résumé

L’énergie solaire est une source d’énergie renouvelable et propre prometteuse, et l’utilisation de modules photovoltaïques pour bénéficier de cette source pour produire de l’électricité est une pratique de plus en plus courante de nos jours. Cependant, le principal inconvénient de cette technologie est le rendement relativement faible, qui est affecté par plusieurs paramètres du système et de l’environnement. Dans cette étude, l’accent est mis sur le transfert de chaleur entre le module et son environnement, ainsi que sur la température du module (T_{pv}), entre autres paramètres efficaces, et son effet sur le processus de conversion solaire en électricité. Par conséquent, dans un premier temps, des expériences ont été menées pour mener une enquête sur la prédiction de la puissance de sortie des modules photovoltaïques, impliquant des réseaux de neurones artificiels (RNA) et une analyse de régression, visant à comprendre et à mettre en évidence l’effet et la relation de la température du module sur ses performances et sa puissance de sortie. Les résultats de cette enquête ont montré que le rayonnement solaire et la température du module sont des paramètres clés pour prédire la puissance de sortie photovoltaïque. De plus, le modèle RNA a montré les meilleures prédictions globales, tandis que la régression linéaire n’a pas pu fournir de bons résultats. Cependant, les modèles RPL (Rational-Power-Law) et PL (Power-Law) proposés ont pu capturer la non-linéarité du système, fournissant un R^2 de 0,998 et 0,996, et un MAE de 1,156 et 1,242, respectivement. Sur la base de ces résultats, une étude similaire a été réalisée pour étudier les paramètres affectant T_{pv}, où, en utilisant des données expérimentales et en mettant en œuvre douze algorithmes d’apprentissage automatique différents, les résultats de l’étude ont indiqué que la température ambiante (T_a), le rayonnement solaire (G), la vitesse du vent (W_s) sont des paramètres importants qui affectent T_{pv}. De plus, le modèle ANN et le modèle non linéaire proposé ont fourni des valeurs R2 de 0,986 et 0,981, avec un MAE de 0,982 et 1,476, et un MSE de 2,181 et 3,464, respectivement. De plus, le modèle proposé a démontré de meilleurs résultats par rapport aux modèles de la littérature. Français Au-delà de cela, et afin de modéliser le transfert de chaleur au sein du module photovoltaïque, des simulations numériques ont été proposées pour effectuer cette modélisation et calculer T_{pv}, où en utilisant des données expérimentales, et après avoir effectué une étude paramétrique, les résultats ont montré que la mise en relais des simulations de transfert de chaleur et d’écoulement de fluide, les résultats pour le calcul de T_{pv} étaient plus précis et exacts. Les résultats de l'étude ont également montré que G, T_a et W_s ont tendance à avoir l'impact majeur sur T_{back}, une augmentation de $100\ W/m^2$ de G peut produire une augmentation de 4 °C de T_{back} à des vitesses de vent faibles, et d'environ $2{,}4\ °C$ pour des W_s relativement plus élevées. T_a tend également à produire une augmentation linéaire de T_{back}, en attendant une augmentation de $5{,}8\ °C$, pour une augmentation de 6 $°C$ de T_a à $700\ W/m^2$ et 1 m/s de rayonnement solaire et de vitesse du vent, respectivement. De plus, un algorithme de simulation a été proposé et programmé pour modéliser et calculer T_{pv}, où les paramètres effectifs susmentionnés ont été considérés comme des entrées. Les résultats de cette étude ont révélé que l'algorithme de simulation proposé a fourni l'un des meilleurs résultats par rapport aux modèles de la littérature, atteignant un R^2 de $0{,}963$ et un MAE de $1{,}883$, ce qui est très proche du meilleur modèle global de King avec $R2 = 0{,}973$ et $MAE = 1{,}663$. De plus, deux nouveaux modèles de prédiction de T_{pv} ont été proposés. Après des tests sur de nouvelles données, le modèle explicite a fourni une première approximation raisonnable atteignant un $R2$ ajusté de $0{,}97$ et un MSE de $3{,}505$, et un modèle implicite précis, atteignant un MSE de seulement $1{,}268$.

Mots clés : Energie solaire ; Panneau photovoltaïque ; Transfert thermique ; Température du panneau PV ; Simulation numérique ; Modélisation mathématique

عنوان الأطروحة: دراسة انتقال الحرارة في لوح كهروضوئي

الكاتب: عبد الحق كدودة، قسم الهندسة الميكانيكية، جامعة المسيلة.

التخصص: طاقوية

ملخص

الطاقة الشمسية هي مصدر طاقة متجددة ونظيفة واعد، واستخدام الوحدات الكهروضوئية للاستفادة من هذا المصدر لتوليد الكهرباء هو ممارسة شائعة بشكل متزايد في الوقت الحاضر. ومع ذلك، فإن العيب الرئيسي لهذه التكنولوجيا هو الكفاءة المنخفضة نسبيًا، والتي تتأثر بالعديد من معلمات النظام والمحيط. في هذه الدراسة، ينصب التركيز على انتقال الحرارة بين الوحدة ومحيطها، وكذلك درجة حرارة الوحدة (T_{pv})، من بين معلمات فعالة أخرى، وتأثيرها على عملية تحويل الطاقة الشمسية إلى كهربائية، لذلك، أجريت أولاً تجارب لإجراء تحقيق للتنبؤ بمخرجات الطاقة للوحدات الكهروضوئية، والتي شملت الشبكات العصبية الاصطناعية (ANNs) وتحليل الانحدار، بهدف فهم وتسليط الضوء على تأثير وعلاقة درجة حرارة بأداء الوحدة ومخرجاتها من الطاقة. أظهرت نتائج هذا التحقيق أن الإشعاع الشمسي ودرجة حرارة الوحدة هي معلمات رئيسية للتنبؤ بمخرجات الطاقة الكهروضوئية. علاوة على ذلك، أظهر نموذج ANN أفضل التوقعات الإجمالية، في حين لم يتمكن الانحدار الخطي من تقديم نتائج جيدة. ومع ذلك، كان نموذج قانون القوة المنطقية (RPL) ونموذج قانون القوة (PL) المقترحين قادرين على التقاط اللاخطية في النظام، مما يوفر R^2 0.998 و 0.996، و MAE 1.156 و 1.242، على التوالي. بناءً على هذه النتائج، تم إجراء دراسة مماثلة للتحقيق في المعلمات التي تؤثر على T_{pv}، حيث أشارت نتائج الدراسة، باستخدام البيانات التجريبية وتنفيذ اثني عشر خوارزمية مختلفة للتعلم الآلي، إلى أن درجة الحرارة المحيطة (T_a)، والإشعاع الشمسي (G)، وسرعة الرياح (W_s) هي معلمات مهمة تؤثر على T_{pv}. بالإضافة إلى ذلك، قدم نموذج ANN والنموذج غير الخطي المقترح قيم R^2 0.986 و 0.981، مع MAE 0.982 و 1.476، و MSE 2.181 و 3.464، على التوالي. علاوة على ذلك، أظهر النموذج المقترح نتائج أفضل عند مقارنته بنماذج الأدبيات. بالإضافة إلى ذلك، ومن أجل نمذجة انتقال الحرارة داخل الوحدة الكهروضوئية، تم اقتراح محاكاة رقمية لأداء هذه النمذجة وحساب T_{pv}، حيث باستخدام البيانات التجريبية، وبعد إجراء دراسة بارامترية، أظهرت النتائج أن نقل محاكاة انتقال الحرارة وتدفق السوائل، كانت نتائج حساب T_{pv} أكثر دقة. أظهرت نتائج الدراسة أيضًا أن G و T_a و W_s تميل إلى التأثير بشكل كبير على T_{back}، حيث يمكن أن تؤدي زيادة

قدرها 100 وات/م^2 في G إلى زيادة قدرها 4 درجات مئوية في T_{back} عند سرعات الرياح المنخفضة، وحوالي 2.4 درجة مئوية لـ W_s أعلى نسبيًا. تميل T_a أيضًا إلى إحداث زيادة خطية في T_{back}، متوقعة ارتفاعًا قدره 5.8 درجة مئوية، لزيادة قدرها 6 درجات مئوية في T_a عند 700 وات/م^2 و 1 متر/ثانية من الإشعاع الشمسي وسرعة الرياح، على التوالي. علاوة على ذلك، تم اقتراح خوارزمية محاكاة وبرمجتها لنمذجة وحساب T_{pv}، حيث تم اعتبار المعلمات الفعالة المذكورة أعلاه كمدخلات. كشفت نتائج هذا البحث أن خوارزمية المحاكاة المقترحة قدمت واحدة من أفضل النتائج مقارنة بنماذج الأدبيات، حيث حققت R^2 من 0.963 و MAE من 1.883، وهو قريب جدًا من أفضل نموذج إجمالي بواسطة King عند $R^2 = 0.973$ و $MAE = 1.663$. بالإضافة إلى ذلك، تم اقتراح نموذجين جديدين للتنبؤ بـ T_{pv}. بعد الاختبار على بيانات جديدة، قدم النموذج الصريح تقريبًا أوليًا معقولًا حقق R^2 معدلًا من 0.97 و MSE من 3.505، ونموذجًا ضمنيًا دقيقًا، محققًا MSE من 1.268 فقط.

كلمات مفتاحية : طاقة شمسية؛ لوح كهروضوئي؛ انتقال الحرارة؛ درجة حرارة لوح كهروضوئي؛ محاكاة رقمية؛ النمذجة الرياضية

Thesis Title: Study of heat transfer in a photovoltaic (PV) module

Authors: Abdelhak Keddouda, Department of mechanical engineering, University of M’Sila

Specialty: Energetics**.**

Abstract

Solar energy is a promising renewable and clean energy source, and the use of photovoltaic modules to benefit from that source to generate electricity is more and more common practice nowadays. However, the main drawback of this technology is the relatively low efficiency, which is affected by several system and ambient parameters. In this study, the focus is on the heat transfer between the module and its surrounding, as well as module temperature (T_{pv}), among other effective parameters, and its effect on the solar to electrical conversion process, therefore, firstly, experiments were conducted to carry on an investigation for the prediction of photovoltaic modules power output was performed, involving Artificial Neural Networks (ANNs) and regression analysis, aiming to understand and highlight the effect and relation of module temperature on its performance and power output. The results of this investigation showed that solar radiation and module temperature are key parameters to predict the photovoltaic power output. Furthermore, the ANN model showed the best overall predictions, while linear regression was unable to provide good results. However, the proposed Rational-Power-Law (RPL) and Power-Law (PL) models were able to capture the nonlinearity in the system, providing an R^2 of 0.998 and 0.996, and a MAE of 1.156, and 1.242, respectively. Based on those findings, similar study was performed to investigate the parameters affecting T_{pv}, where, using experimental data, and implementing twelve different machine learning algorithms, the study results indicated that ambient temperature (T_a), solar radiation (G), wind speed (W_s) are important parameters that affect T_{pv}. Additionally, the ANN model and the proposed non-linear model provided an R^2 values of 0.986 and 0.981, with a MAE of 0.982 and 1.476, and MSE of 2.181 and 3.464, respectively. Moreover, the proposed model demonstrated better results when compared with literature models. Beyond that, and in order to model the heat transfer within the photovoltaic module, numerical simulations were proposed to perform that modeling and calculate T_{pv}, where using experimental data, and after performing a parametric study, results showed that relaying of heat transfer and fluid flow simulations, results for calculating T_{pv} were more accurate and precise. The study results also showed that G, T_a and W_s tend to have the major impact on T_{back}, an increase of 100 W/m^2 in G can produce an increase of 4 $°C$ in T_{back} at low wind speeds, and about 2.4 $°C$ for relatively higher W_s. T_a also tends to yield linear increase in T_{back}, expecting $5.8\ °C$ rise, for $6\ °C$ increase in T_a at $700\ W/m^2$ and $1\ m/s$ of solar radiation and wind speed, respectively. Moreover, a simulation algorithm was proposed and programmed to model and calculate T_{pv}, were the aforementioned effective parameters was considered as inputs. The findings of this investigation revealed that the proposed simulation algorithm provided one of the best results in comparison to literature models, achieving an R^2 of 0.963 and a MAE of 1.883, which is very close to the best overall model by King at $R^2 = 0.973$ and $MAE = 1.663$. Additionally, two new models for T_{pv} prediction were proposed. After testing on new data, the explicit model provided a reasonable first approximation attaining an adjusted R^2 of 0.97 and a MSE of 3.505, and an accurate implicit model, achieving a MSE of only 1.268.

Keywords: Solar energy; Photovoltaic module; Heat transfer; PV module temperature; Numerical simulation; Mathematical modeling.